

Ali Afzalifar

MODELLING NUCLEATING FLOWS OF STEAM

Thesis for the degree of Doctor of Science (Technology) to be presented with due permission for public examination and criticism in the lecture room 2303 at Lappeenranta University of Technology, Lappeenranta, Finland on the 6th of September, 2017, at noon.

Acta Universitatis
Lappeenrantaensis 762

- Supervisors Associate Professor Teemu Turunen-Saaresti
LUT School of Energy Systems
Lappeenranta University of Technology
Finland
- Associate Professor Aki Grönman
LUT School of Energy Systems
Lappeenranta University of Technology
Finland
- Reviewers Professor Günter H. Schnerr
Department of Mechanical Engineering
The Technical University of Munich
Germany
- Doctor Shigeki Senoo
Research Manager
Turbo Machinery Research Department
Mitsubishi Hitachi Power Systems
Japan
- Opponent Doctor Brian Haller
Aerodynamics, Performance, Heat Transfer – Technical Lead
GE Power
United Kingdom

ISBN 978-952-335-121-9
ISBN 978-952-335-122-6 (PDF)
ISSN-L 1456-4491
ISSN 1456-4491

Lappeenrannan teknillinen yliopisto
Yliopistopaino 2017

Abstract

Ali Afzalifar

Modelling nucleating flows of steam

Lappeenranta 2017

102 pages

Acta Universitatis Lappeenrantaensis 762

Diss. Lappeenranta University of Technology

ISBN 978-952-335-121-9, ISBN 978-952-335-122-6 (PDF), ISSN-L 1456-4491, ISSN 1456-4491

The nucleation-induced condensation of steam in the course of expansion in turbines gives rise to the loss of efficiency and blading erosion. Numerical modelling is a precious asset to predict and understand the condensation effects on the steam turbine performance with the aim of developing more-informed turbine design methods. This thesis concerns the two main constituents of numerical models for nucleating flows of steam; the phase change model and the dispersed multiphase flow model.

With respect to the phase change model, the classical nucleation theory is examined in light of the recent nucleation rate measurements for water. In particular, the supersaturation dependence of classical nucleation theory is critically evaluated. It is shown that the underproduction of the liquid mean droplet size can be explained in connection with not only the droplet growth equation but also the nucleation rate equation.

With respect to the second aspect, several models which are typically the most common choices for modelling wet-steam flows are implemented and compared with one another. Among these models, the moment-based methods are particularly attractive as they can take account of the polydispersity of wet-steam flows while conveniently lending themselves to an Eulerian reference frame. However, it is discussed that the moment sets can become corrupted applying high-order temporal and spatial discretisation schemes. It is shown that moment corruption completely blocks the application of the quadrature method of moments. Moreover, it is demonstrated that although the moment corruption does not block the conventional method of moments, it can result in droplet size distributions with negative or unreasonable variance and, therefore, increases the uncertainty over the results.

Keywords: nucleation, wet-steam flow, method of moments, steam turbine

Acknowledgements

Thank you,

Teemu Turunen-Saaresti,

for being my first supervisor, trusting me to find my own path in research, putting up with my impatience and unusual work style, and all the support and motivation during this project. I do not remember any discouraging comment from you.

Thank you,

Aki Grönman,

for being my second supervisor and all your guidance, support and help.

Thank you,

Alireza Ameli and Tomi Naukkarinen,

for being my friends, best colleagues and supporting me.

Thank you,

all my friends specially Ali and Saeed,

for being with me all the way.

Ali Afzalifar

January 2017

Lappeenranta, Finland

To my beloved family: my mother, brother and sister

Contents

Abstract

Acknowledgements

Contents

List of publications	11
Nomenclature	13
1 Introduction	17
1.1 Background and motivation.....	17
1.2 Thesis objectives and outline.....	18
1.3 Thesis objectives and outline.....	19
2 Phase change model	21
2.1 Classical nucleation theory.....	21
2.2 Supersaturation dependence of classical nucleation theory.....	22
2.3 Droplet growth equations.....	25
2.4 Characteristic problem of modelling LP wet-steam flows.....	27
2.5 Link between mean droplet size underprediction and excessive supersaturation dependence of CNT.....	31
2.6 Illustrative examples.....	32
2.6.1 Nozzle B.....	34
2.6.2 Experiment 203.....	38
3 Dispersed multiphase flow models	43
3.1 Transport equations.....	43
3.1.1 Numerical discretisation schemes.....	44
3.1.2 Thermodynamics properties.....	45
3.2 Moment-based models.....	46
3.2.1 Conventional method of moments.....	47
3.2.2 Quadrature method of moments.....	48
3.2.3 Moment-based models in a Lagrangian reference frame.....	50
3.3 Discrete-spectrum Eulerian-Lagrangian model.....	50
3.4 Monodispersed model.....	52
4 Comparison of dispersed multiphase flow models	53
4.1 Introduction of test cases.....	53
4.2 Grid dependency study.....	55
4.3 Nozzle A.....	56
4.4 Experiment 252.....	61

4.5	Stability and computational cost of studied DMFMs.....	64
5	Moment corruption and nonrealisability problem	67
5.1	Properties of moment space and realisability condition.....	67
5.2	Moment corruption.....	68
5.3	Solution techniques for nonrealisability problem	71
5.3.1	First solution type; realisable high-order schemes	72
5.3.2	Second solution type; moment corrections	72
5.4	Comparison of solutions to nonrealisability	73
5.4.1	Realizable quasi-high-order scheme.....	73
5.4.2	Moment corrections.....	75
6	Nonrealisability problem with CMOM	79
6.1	Subcritical condensation with a single nucleation process.....	79
6.2	Subcritical condensation with two nucleation processes.....	82
6.3	Unsteady supercritical condensation	84
7	Conclusions and recommendations	87
7.1	Origin of droplet size underprediction in modelling of low pressure nucleating flows of steam	87
7.2	Comparison of moment-based methods for representing droplet size distributions in supersonic nucleating flows of steam.....	87
7.3	Nonrealisability problem with quadrature method of moments in wet-steam flows and solution techniques	88
7.4	Nonrealisability problem with conventional method of moments in wet-steam flows	88
	References	89
	Appendix: details of nozzle test cases	99
	Publications	

List of publications

This thesis is based on the following articles which are referred to as Publications hereafter in this thesis. The rights have been granted by publishers to include the Publications in the dissertation.

- I. Afzalifar, A., Turunen-Saaresti, T., and Grönman, A. (2016). Origin of droplet size underprediction in modelling of low pressure nucleating flows of steam. *International Journal of Multiphase Flow*, 86, pp. 86-98.
- II. Afzalifar, A., Turunen-Saaresti, T., and Grönman, A. (2016). Comparison of moment-based methods for representing droplet size distributions in supersonic nucleating flows of steam. In: *Proceedings of the 16th International Symposium on Transport Phenomena and Dynamics of Rotating Machinery ISROMAC*, Honolulu, Hawaii, April 10-15.
 - This Publication has been selected to be published in the special issue, entitled "Flows in Rotating Machineries: some Recent Advances", of *Journal of Fluids Engineering*.
- III. Afzalifar, A., Turunen-Saaresti, T., and Grönman, A. (2017). Nonrealizability problem with quadrature method of moments in wet-steam flows and solution techniques. *Journal of Engineering for Gas Turbines and Power*, 139, pp. 012602.
- IV. Afzalifar, A., Turunen-Saaresti, T., and Grönman, A. (2016). Nonrealisability problem with the conventional method of moments in wet-steam flows. In: *Wet Steam Conference*, Prague, September 12-14.
 - This Publication has been selected to be published in the special issue, entitled "Wet Steam 2016", of *Proceedings of the Institution of Mechanical Engineers, Part A: Journal of Power and Energy*.

I am the principal author and investigator of all Publications. Teemu Turunen-Saaresti and Aki Grönman, as the technical advisors, actively contributed to all Publications, providing interpretations of results, valuable suggestions and guidance.

Nomenclature

In the present work, variables and constants are *italicised*, vectors are denoted using **bold regular style**, and abbreviations are denoted using regular style.

Latin alphabet

A	area	m^2
A_1	surface area of one molecule	m^2
a	parameter defined in Equation 3.17	m/sec
b	parameter defined in Equation 3.17	$1/\text{sec}$
\mathbf{C}	convective flux vector	–
C	parameter defined in Equation 2.6	–
C_{1-4}	calibration constants for nucleation rates in chapter 2	–
c_p	specific heat capacity at constant pressure	$\text{J}/(\text{kgK})$
E	total internal energy	$\text{J}/(\text{kgK})$
d	diameter	m
d_{2j}	parameter defined in Equation 5.1	–
f	parameter defined in Equation 2.17	–
f	number density function	$1/\text{m}$
F	flux of number density function	$1/\text{sec}$
G	Gibbs free energy	J
H	total enthalpy	$\text{J}/(\text{kgK})$
h	specific enthalpy	$\text{J}/(\text{kgK})$
J	nucleation rate	$1/(\text{kgsec})$
K	number of droplet bins	–
k	parameter in MUSCL, defined in Equations 3.12 and 3.13	–
K_B	Boltzmann's constant	J/K
Kn	Knudsen number	–
l	mean free path	m
l	parameter defined in Equation 5.2	–
M	Mach number advection Mach number denoted	–
M_a	advection Mach number	–
m	molecular mass	kg
m	parameter defined in Equation 5.2	–
N	number of droplets per unit of mass	$1/\text{kg}$
N_g	number of cells in a computational domain	–
N_i	number of droplets in the i^{th} droplet bin	$1/\text{kg}$
n	number of quadrature points	–
p	pressure	bar
p_0	inlet stagnation pressure	bar
Pr	Prandtl number	–
q_c	condensation coefficient	–
q_e	evaporation coefficient	–

R	evaporation coefficient	J/(kgK)
r	radius	m
S	supersaturation ratio	–
s	throat height	m
T	temperature	K
t	time	sec
U	numerical velocity	m/sec
u	velocity	m/sec
V	volume in the particle phase space	m ⁴
v	parameter defined in Equation 5.14	–
v_1	volume of one molecule	m ³
w	weight	1/kg
X	x-coordinate (width)	m
Y	y-coordinate (depth)	m
Y	wetness fraction	–
y_i	wetness fraction of the i^{th} droplet bin	–
Z	z-coordinate (height)	m
z	parameter defined in Equation 5.13	–

Greek alphabet

α	parameter defined in Equation 2.13	–
α	isobaric expansion coefficient	1/K
γ	specific heats ratio	–
ζ	$= \Delta t / (A_l \Delta X_l)$	sec/m ³
θ	parameter defined in Equation 2.16	–
λ	thermal conductivity	W/(mK)
μ	moment	–
ρ	density	kg/m ³
σ	surface tension	J/m ²
σ	standard deviation	m
ψ	parameter defined in Equation 2.13	–

Superscripts

.	derivative with respect to time
*	related to the critical cluster/droplet

Subscripts

g	number of molecules in a cluster
l	computational cell index
i	radius, weight and droplet bin index
j	moment index
L	left state of a computational cell

l	liquid properties
m	liquid-vapour mixture properties
R	right state of a computational cell
s	saturation properties
v	vapour mixture properties
20	surface-area-averaged value
32	Sauter mean value
σ	surface work

Abbreviations

AUSM	advection upstream splitting method
CFD	computational fluid dynamics
CFL	Courant–Friedrichs–Lewy
CPU	central processing unit
CMOM	conventional method of moments
Cou	Courtney’s correction factor to CNT
CNT	classical nucleation theory
DMFM	dispersed multiphase flow model
EOS	equation of state
exp	critical size based on experiment
E-L	discrete-spectrum Eulerian-Lagrangian and Eulerian-Lagrangian
E-E	Eulerian-Eulerian
G-T	critical size based on Gibbs-Thomson
Kan	Kantrowitz’s correction factor to CNT
LHS	left-hand side
LP	low pressure
MOM	method of moments
Mono	monodispersed model
MUSCL	monotonic upstream centred scheme for conservation laws
NDF	number density function
PPS	particle phase space
QMOM	quadrature method of moments
QS	quasi-second-order scheme
RHS	right-hand side
Se	semi-empirical
WM	Wright’s moment correction

1 Introduction

1.1 Background and motivation

Phase transition, whether in the form of condensation, evaporation or sublimation, is a ubiquitous phenomenon in nature and engineering applications, and thus, a problem of intrinsic interest to scientists and engineers. However, due to the extraordinary complexity of this phenomenon, even for water as the most extensively studied substance in the history of science, the physical details of phase transition are not adequately understood yet. Among different forms of phase transition, condensation has received much attention due to its wide-ranging application in science and engineering. Applications related to the condensation of vapours can be found in fields as diverse as fluid dynamics (Schnerr, et al., 1995), energy conversion (Yan, et al., 1999) and metallurgy (Porter, et al., 2009). The major contributions to understanding and modelling the condensation of vapour flows can be traced back to three main research lines as follows.

In the early 20th century shortly after the introduction of steam turbines into the power industry, it was realised that there is a negative correlation between the steam wetness fraction and the turbine efficiency (Bauman, 1921). Further, it was noted that the blading erosion becomes severe when the wetness fraction increases in steam turbines (Stodola, 1922). In the 1960s, the advent of nuclear steam turbines, suffering from pronounced problems related to excessive wetness, rapidly increased motivation for researching the condensation problem in these machines (Gyarmathy, 1962; Kirillov & Yablonik, 1968; Moore & Sculpher, 1969). Recently, the incentives to increase the efficiency and competitiveness of renewable power plants, such as plants with geothermal and biofuel steam turbines which are hindered by excessive moisture formation, have revived the interest in studying and modelling condensing flows of steam, the so-called ‘wet-steam’ flows. Another source of motivation in this topic has always been atmospheric science concerning the condensation, growth/evaporation and transport of aerosols in the atmosphere (Mason, 1960; Kulmala, et al., 2013). Moreover, in the 1950s, the Space Race and missile competition during the cold war sparked the interest in research in condensing flows of air and nitrogen flows in cryogenic wind tunnels (Hall & Kramer, 1979), and aerosol formation from metal vapours (Fuks & Sutugin, 1970).

From the engineering standpoint, the crucial importance of steam turbines in the global power production, despite its rises and falls, has constantly fuelled the interest in research on steam condensing flows. As a result, so far a large body of knowledge about wet-steam flows has been acquired. Massive improvements in the computational power and inventions of advanced numerical techniques have led to the development of sophisticated computational models for predicting the condensation and its effects on the flow behaviour. The new models are able to incorporate the analytical forms of phase transition theories into detailed computational fluid dynamics (CFD) calculations of steam flow (Gerber, 2002; Gerber, 2008; Dykas & Wróblewski, 2011; Chandler, et al., 2014).

However, most steam turbine manufacturers still hesitate to integrate new wet-steam models into their design routines. The general tendency among the manufacturers is to rely on fully/semi-empirical methods to take account of condensation effects. The lack of confidence in new computational models stems from a poor theoretical understanding of the phase transition phenomenon and also the highly interdisciplinary nature of the condensation problem in steam turbines. The condensation in steam turbines is not merely about the phase transition; instead, it is a fascinating and complex question which arises at the intersection of thermodynamics, fluid dynamics and transfer of mass and energy, all drifting between the macroscopic and microscopic worlds. In fact, after more than a century of research on wet-steam flows, the modelling predictions cannot deliver the required engineering accuracy even for simple experimental test cases (Bakhtar, et al., 2005; Gerber & Mousavi, 2006).

1.2 Thesis objectives and outline

To reduce the complexity of the problem to a tractable level, this thesis examines the main constituting components of a typical wet-steam model in isolation. Thus, it is possible to trace the imprecision in modelling back to each individual component. In general, the backbone of all CFD calculations for predicting steam condensing flows is formed by two components:

- The phase change model integrating the theories of nucleation and droplet growth. The former provides an analytical expression to quantify the formation or nucleation rate of the very first nuclei of the new phase in the old phase, i.e. liquid droplets inside the vapour. The latter defines the growth rate of the liquid nuclei/droplets once they are formed by means of nucleation.
 - Publication I concerns this component.
- The dispersed multiphase flow model (DMFM) which integrates the phase change model into the flow equations to be solved numerically. This model governs the mass, heat and momentum transfer between the two phases, namely the liquid droplets being the dispersed phase and the vapour being the continuous phase.
 - Publications II, III and IV concern this component.

Chapter 2 is dedicated to Publication I starting with a brief introduction to classical nucleation theory (CNT) in section 2.1, followed by a critical discussion on CNT supersaturation dependence and droplet growth equations in sections 2.2 and 2.3, respectively. Sections 2.4 and 2.5 explain a typical problem in the modelling of low pressure (LP) wet-steam flows and its connection to the dependence of CNT on supersaturation. Chapter 2 ends with examinations of two well-known LP nozzle test cases in section 2.6, showing that rectifying the dependence of the nucleation rate on supersaturation can improve the mean droplet size prediction in modelling LP wet-steam flows.

Chapter 3 first, in section 3.1, gives a description of the numerical solution to the transport equations of wet steam as a liquid-vapour mixture. The chapter continues with an introduction of the studied DMFMs, beginning in section 3.2 with the method of moments (MOM) and its two main branches: the quadrature and conventional method of moments (QMOM and CMOM). The other two DMFMs – namely the discrete-spectrum Eulerian-Lagrangian (E-L) model and the monodispersed model (Mono) – are presented in sections 3.3 and 3.4, respectively. In short, the chapter covers the complete details on the numerical aspect of models applied in all Publications.

Chapter 4 corresponds to Publication II, presenting comprehensive comparisons between the DMFMs introduced in Chapter 3.

Chapter 5 explains the concepts of the realisability condition in section 5.1 and moment corruption in Section 5.2. Thereafter, the solution techniques for the nonrealisability problem are described in section 5.3 and compared in section 5.4. The chapter encompasses the theoretical parts of Publications III and IV on the nonrealisability problem and also the results and discussions presented in Publication III about the techniques to solve the nonrealisability problem in the context of the QMOM.

Chapter 6 presents the examination of Publication IV on the nonrealisability problem in the context of the CMOM. Three types of test cases with distinct characteristics are investigated in sections 6.1-6.3 to see the effects of the nonrealisability problem on the CMOM performance.

Chapter 7 presents the conclusions of this thesis based on the findings of Publications I, II, III and IV or equivalently chapters 2, 4, 5 and 6.

Several nozzle experiments are used in this thesis and the Publications. All details about these nozzles geometries and boundary conditions are presented in the appendix of this thesis.

1.3 Thesis contributions

In Publication I, the underprediction of the mean liquid droplet size in modelling wet-steam flows was explained for the first time in connection with the excessive dependence of CNT on supersaturation. It was shown that by moderating the dependence of CNT on supersaturation, the prediction of the mean droplet size can be improved. To the knowledge of author, none of the previous studies had noticed this connection.

In Publication II, four different DMFMs, i.e. the CMOM, QMOM, E-L model and Mono, were compared with the main focus on the accuracy of DMFMs in representing the droplet size distribution. Previous comparative studies had only considered some of the above-mentioned DMFMs, not all of them. In addition, contrary to the previous works,

the CMOM and QMOM are cast in an Eulerian frame of reference as it is the convenient implementation of these methods in an Eulerian framework, making them interesting for modelling complex wet-steam flows in turbines.

In Publication III, the nonrealisability problem with QMOM was pointed out and presented to the wet-steam research community. The nonrealisability problem had not been noted in any of the previous works pertaining to wet-steam research. However, it should be stressed that this problem and its remedies were addressed by a few researchers in other fields, such as aerosol and combustion modelling prior to the current author's Publications.

In Publication IV, the effect of the nonrealisability problem on the CMOM was examined. As it seems that the CMOM is not burdened by nonrealisability, no study had previously investigated this problem with it. However, through several test cases it was shown that nonrealisable moment sets are generated also in the CMOM, and they can lead to droplet size distributions with unreasonable values for variance and also skewness.

2 Phase change model

This chapter covers Publication I and also presents equations of the nucleation rate and droplet growth rate which form the phase change model used also in all other Publications.

2.1 Classical nucleation theory

Understanding nucleation of a new phase inside an old phase, followed by the new phase growth, is of tremendous importance in science and engineering. Nucleation theory provides the main recourse for explaining natural and engineered phase change processes such as crystallisation (Vekilov, 2010), aerosol formation (Laaksonen, et al., 1995), the formation of astrophysical particles (Gail & Sedlmayr, 1988) and even the quark-hadron transition in the early universe just after the Big Bang (Fuller, et al., 1988). Among different lines of study in nucleation theory, e.g. ab initio (Temelso, et al., 2011) and classical (Yasuoka & Matsumoto, 1998) molecular dynamics simulations and the density functional approach (Laaksonen & Oxtoby, 1995), classical nucleation theory (CNT), although suffering from severe shortcomings, is still the most popular approach. The popularity of CNT mainly stems from its simplicity and lack of any other quantitative theory with better accuracy applicable to practical cases.

The foundations of CNT have been built on the major studies by Thomson (1872), Helmholtz (1886) and Gibbs (1878) from the late 19th century. These studies concerned the thermodynamic aspect of nucleation, defining the free energy change of vapour in the course of droplet formation. Later in the 20th century, the works of Farkas (1927), Becker and Döring (1935), Volmer (1939), Zeldovich (1942) and Frenkel (1955) focusing on the kinetic aspect of CNT and its mathematical formulation led to the current form of CNT representable as

$$J_{CNT} = K \exp\left(-\frac{(\Delta G^*)_{CNT}}{k_B T_v}\right) \quad (2.1)$$

where J_{CNT} is the nucleation rate per unit of volume, $(\Delta G^*)_{CNT}$ is the change in Gibbs free energy in the course of a critical cluster formation, k_B is Boltzmann's constant, T_v is the vapour temperature, and K is the so called "pre-exponential factor." According to the standard form of CNT, K is

$$K = \left(\frac{2\sigma}{\pi m}\right)^{1/2} \left(\frac{p}{k_B T_v}\right)^2 v_1 \quad (2.2)$$

in which σ is the planar surface tension, m is the molecular mass, p is pressure and v_1 is the new phase (liquid) molecular volume, which can be computed by knowing the liquid bulk density, denoted by ρ_l , and regarding the molecule as a sphere.

The free energy change for nucleation of a g -mer, i.e. a cluster made of g molecules, in a supersaturated vapour is due to, first, the volume work exerted on the system to increase the pressure of vapour to its saturation pressure p_s , and second, the surface work done by the system to build up a phase boundary, denoted by $\Delta G_{g,\sigma}$. The combination of these two is

$$\Delta G_g = -gk_B T_v \ln(S) + k_B T_v \ln(S) + \Delta G_{g,\sigma} \quad (2.3)$$

where S is the supersaturation, i.e. $S = p/p_s$. The second term on the right-hand side (RHS) of the equation above was introduced by Courtney's correction to CNT (Courtney, 1961) to take account of the partial pressure of clusters. This term reduces J_{CNT} by the factor of $1/S$. The first two terms on the RHS of Equation 2.3 are dependent on S and given based only on thermodynamics. On the other hand, the third term is a function of temperature alone which inherits several inelegant assumptions made in CNT including the capillary approximation, the spherical shape for clusters having only a couple of molecules and the 'surface of tension'. It is commonly believed that the deviations between nucleation experiments and CNT chiefly come from these assumptions (Lothe & Pound, 1962; Dillmann & Meier, 1991; Reiss, et al., 1997). Nevertheless, the very same assumptions permit calculation of $\Delta G_{g,\sigma}$ simply through multiplication of a g -mer surface area, denoted by A_g , and the surface tension. Thus, in the case of the homogenous nucleation, $\Delta G_{g,\sigma}$ is

$$(\Delta G_{g,\sigma})_{CNT} = A_g \sigma = A_1 g^{\frac{2}{3}} \sigma \quad (2.4)$$

in which A_1 is a monomer surface area of given as $A_1 = (\pi(6m/\rho_l)^2)^{1/3}$.

2.2 Supersaturation dependence of classical nucleation theory

Recently, Girshick (2014) pointed out that CNT shows incorrect dependence on supersaturation when it is compared to experimental measurements of stationary nucleation rates. Girshick attributed this incorrect dependence on supersaturation to the imprecision of CNT in the calculation of $\Delta G_{g,\sigma}$. Girshick's argument contradicts the broad agreement on the correctness of the supersaturation dependence of CNT asserted in many studies such as those by Oxtoby (1992), Wölk & Strey (2001) and Manka, et al. (2010). Moreover, this argument is remarkable as it connects the supersaturation dependence of CNT to the work required for the phase boundary formation, i.e. $(\Delta G_{g,\sigma})_{CNT}$, which is a function of only temperature. Applying the first nucleation theorem, proposed by Kashchiev (1982), Girshick argued that the poor supersaturation dependence of CNT is corroborated by nucleation rate measurements for several substances, like water, argon, nitrogen and the 1-alcohols. Girshick's argument has already been approved by other researchers as being well-founded (Hansen, 2014; Mullick, et al., 2015).

The first nucleation theorem furnishes a model-independent approach to compute the number of molecules in the new phase critical cluster from the isothermal nucleation rate as

$$\left(\frac{\partial \ln(J)}{\partial \ln(S)}\right)_T = g^* + 1. \quad (2.5)$$

If g^* is computed by the equation above from the nucleation rate experiment; it is known as the experimental molecular content of the critical cluster and denoted by g_{exp}^* . In other words, for each isothermal nucleation measurement, g_{exp}^* is obtained by linear least square fits to $\ln(J)$ vs. $\ln(S)$. Considering Equation 2.5, the first nucleation theorem suggests that any defect in the theoretical computation of g^* directly stems from the erroneous slope of J vs. S , or equivalently the incorrect supersaturation dependence of J in theory. The relation of g^* to the slope of J vs. S can be further clarified by integrating both sides of Equation 2.5, which reads

$$J = C(T_v)S^{g^*+1} \quad (2.6)$$

in which $C(T_v)$ is a function of temperature alone to account for the integral boundary conditions. According to CNT, see Equation 2.1, $C(T_v)$ equates to $K_s + \exp(-\Delta G_\sigma/k_B T_v)$ where K_s is the pre-exponential factor calculated at saturation pressure.

According to the Gibbs free-energy minimisation, the theoretical molecular content of the critical cluster based on CNT is given by differentiating Equation 1.3 with respect to g to find the extremum of the change in the Gibbs free energy as

$$\frac{\partial}{\partial g} (\Delta G_{g=g^*})_{CNT} = 0 \rightarrow k_B T_v \ln(S) = \frac{2}{3} A_1 (g^*)^{-\frac{1}{3}} \sigma. \quad (2.7)$$

Due to the necessity of a phase boundary formation, the found extremum is actually a maximum for the change in the Gibbs free energy. It is stressed that the term $(2/3)A_1(g^*)^{-1/3}\sigma$ in the equation above depends on CNT assumptions to calculate $(\Delta G_{g,\sigma})_{CNT}$. On the hand other, $k_B T_v \ln(S)$ is computed with recourse only to thermodynamics. Equation 2.7 is rearranged to give the final expression of the critical cluster size, i.e. the Gibbs-Thomson equation, as

$$g_{GT}^* = \left(\frac{2A_1\sigma}{3k_B T_v \ln(S)} \right)^3. \quad (2.8)$$

As explained for Equation 2.7, g_{GT}^* is directly dependent on how $(\Delta G_{g,\sigma})_{CNT}$ is calculated. Moreover, by relating the radius of a cluster to its molecular content as $4\pi r^2 = A_1 g^{\frac{2}{3}}$, the critical radius r^* is computed as

$$r^* = \frac{2m\sigma}{\rho_l k_B T_v \ln(S)}. \quad (2.9)$$

Considering Equations 2.6 and 2.8, the discrepancies between g_{GT}^* and g_{exp}^* , and similarly the incorrect dependence of CNT on supersaturation must be attributed to the imprecise calculation of $(\Delta G_{g,\sigma})_{CNT}$, although this term by itself is a function dependent on temperature alone.

Figure 2.1 compares g_{exp}^* from nine experimental works by Wölk & Strey (2001), Manka, et al. (2010), Brus, et al. (2008), Brus, et al. (2009), Miller, et al. (1983), Luijten, et al. (1997), Holten, et al (2005), Kim, et al. (2004) and Mikheev, et al. (2002), denoted as Refs. 1-9, respectively, with g_{GT}^* for the same temperature and supersaturation. It can be seen that only few points lie on the “perfect agreement” line, and for all of the other measurement points, CNT overpredicts g^* . In addition, the deviation between g_{GT}^* and g_{exp}^* continuously increases as the critical size becomes larger. Therefore, based on Equation 2.5 or 2.6, it is concluded that for water, the slope of J vs. S is increasingly overpredicted by CNT as the critical size becomes larger for higher temperatures and lower supersaturations (see Figure 2.2).

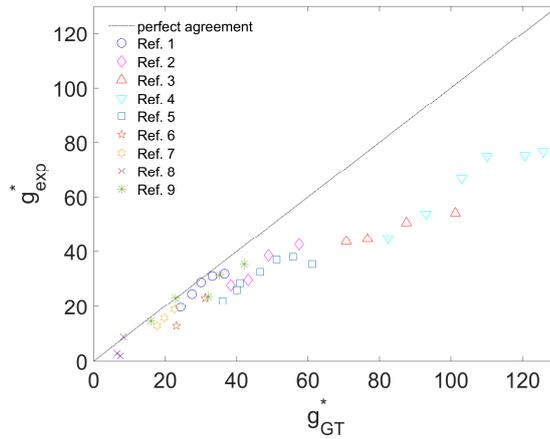


Figure 2.1: Comparison of g_{GT}^* and g_{exp}^* for water, recalculated from data given by Manka, et al. (2010), by inclusion of 1 according to the RHS of Equation 2.5 which was ignored by Manka, et al. (2010).

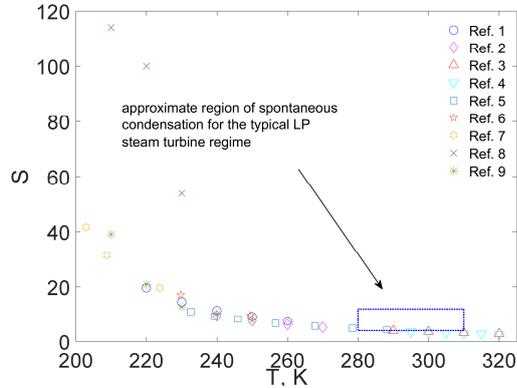


Figure 2.2: Supersaturations and temperatures of nucleation rate experiments for water and the typical regime of spontaneous nucleation in LP steam turbines.

Unfortunately, as illustrated in Figure 2.2, the operating region in LP steam turbines is not covered by the nucleation experiments. Only near the lower supersaturation limit of the shown region, a few points of Ref. 3 (Brus, et al., 2008) and Ref. 4 (Brus, et al., 2009) overlap with this region. Therefore, all that can be said based on Figures 2.1 and 2.2 is that for all the experimental studies that cover either the supersaturation or temperature intervals of typical LP wet-steam regimes, CNT constantly predicts larger critical sizes relative to g_{exp}^* . It is emphasised that the slope of J vs. S given by CNT becomes excessively steeper for higher temperatures corresponding to the typical temperature range in LP wet-steam turbines.

2.3 Droplet growth equations

After nucleation, the growth of liquid droplets is determined by mass and heat (energy) transfer between the droplets and vapour. Due to the high specific heat of the evaporation of water and especially in the absence of an inert gas, it is believed that the droplet growth rate is limited by the rate at which the droplet can transfer the latent heat back to the vapour. The characteristics of the transfer processes are defined by the Knudsen number, the ratio of the mean free path to the droplet diameter $Kn = \bar{l}_v/2r$. For a Kn lower than 0.01, continuum mechanics hold, and for a Kn larger than 4.5, the free-molecular regime applies. The intermediate Knudsen numbers, i.e. between 0.01 and 4.5, correspond to the transition regime. Most of droplets in steam turbines, especially in LP turbines, grow in the transition regime (Gyarmathy, 1976).

In the free-molecular regime, the kinetic theory is applied to predict the heat and mass transfer, while in the continuum regime, the transfer process is governed by diffusion. However, in the transition regime there are serious doubts over defining the droplet growth as the interactions of molecules near the droplet surface are highly complicated and difficult to characterise (Young, 1982). Applying a correction term as a function

of Kn , Gyarmathy (1976) developed a general heat transfer coefficient for a broad range of Knudsen numbers from the continuum regime down to the free molecular regime. This generalisation considerably increases the uncertainty about the heat transfer rate and consequently the droplet growth rate. The Gyarmathy droplet growth equation is written as

$$\dot{r} = \frac{dr}{dt} = \frac{\lambda_v(T_l - T_v)}{\rho_l h_{lv}(r + 1.59\bar{l}_v)} \quad (2.10)$$

where λ_v is the vapour thermal conductivity, h_{lv} is the specific enthalpy of evaporation, and T_l is the droplet temperature. Since T_l is not known, a second relation, given from the mass transfer, has to be coupled with Equation 2.10 to compute the growth rate iteratively. To sidestep the iterative calculations of T_l and \dot{r} , Gyarmathy (1976) proposed an algebraic relation to estimate T_l as

$$T_l = T_s - \Delta T \frac{r^*}{r} \quad (2.11)$$

where $\Delta T = T_s - T_v$ is the supercooling degree, T_s is the saturation temperature and r is the droplet radius. Using the equation above for T_l , the iteration procedure is circumvented and the calculation speed is significantly enhanced, albeit at the expense of adding another source of uncertainty to the calculation. Gyarmathy's droplet growth equation is the most common choice for modelling wet-steam flows, chiefly because of its simplicity and the absence of any alternative which can provide more accurate results.

Subsequently, Young (1982) slightly modified Gyarmathy's equation and also introduced a semi-empirical correction factor to it to match both the pressure and droplet size measurements in LP nozzle experiments. The modified droplet growth rate by Young reads

$$\dot{r} = \frac{\lambda_v(1 - \frac{r^*}{r})\Delta T}{\rho_l h_{lv} r \left(1 + (1 - \psi)3.78 \frac{Kn}{Pr_v}\right)} \quad (2.12)$$

where Pr_v is the vapour Prandtl number and $(1 - \psi)$ is the above-mentioned semi-empirical correction in which ψ is

$$\psi = \frac{RT_s}{h_{lv}} \left[\alpha - 0.5 - \left(\frac{\gamma + 1}{2\gamma}\right) \left(\frac{c_p T_s}{h_{lv}}\right) \left(\frac{2 - q_c}{2q_c}\right) \right] \quad (2.13)$$

where R is the specific gas constant, γ is the vapour isentropic exponent, c_p is the isobaric specific heat capacity of the vapour, α is a tuning parameter to provide agreement with the experiments and q_c is the condensation coefficient with the typical value of unity. Furthermore, ψ is derived based on the assumption that during non-equilibrium

condensation, the evaporation coefficient q_e is less than the condensation coefficient. That is to say, the probability of absorbing vapour molecules impinging on the liquid droplet surface is greater than the probability of liquid molecules escaping to the vapour from the surface of the droplet. This assumption, although retains the physical justifiability for the proposed correction factor, is yet to be proved and it is merely applied to increase the droplet growth rate and bring predictions in line with LP nozzle experiments (Bakhtar, et al., 2005). Figure 2.3 shows the effects of different values for α on the droplet growth rate by comparing the growth rates normalised with respect to $\alpha = 0$. As shown in Figure 2.3, approaching the continuum regime, all the growth rates converge, indicating that Equation 2.12 becomes insensitive to α . In contrast, the growth rates deviate significantly from one another in the transition and free-molecular regimes. Therefore, for LP wet-steam flows in the vicinity of the nucleation zone where droplets are extremely small and Kn is very large, higher values of α significantly enhance the droplet growth rates.

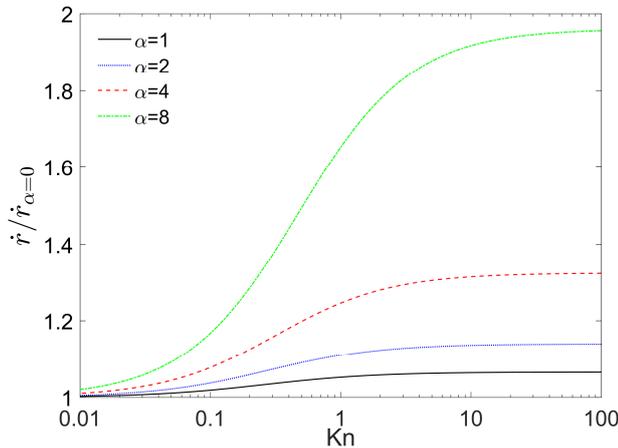


Figure 2.3: Effects of α on the droplet growth rate for $q_c = 1$, $Pr_v \approx 1$, $\gamma = 1.3$ and $\bar{l}_v = 0.1$ micron.

2.4 Characteristic problem of modelling LP wet-steam flows

The typical problem in modelling LP wet-steam flows is that only by enhancing the droplet growth is it possible to match the measured pressures and avoid underpredicting the mean droplet size. The underprediction of the mean droplet size is also common issue in modelling wet-steam flows in LP turbines (Chandler, et al., 2014). In wet-steam turbines, the liquid droplet size strongly affects the flow behaviour, the possibility and extent of further nucleation processes, turbine performance and balding erosion (White, et al., 1996; Bakhtar, et al., 2006). Thus, precise prediction of the size distribution of liquid droplets in wet-steam turbines is equally important as the accurate information on the pressure distribution including the location and significance of the condensation shock.

To further discuss this problem, Nozzle B of the study by Moore et al. (1973), being a very well-known LP nozzle test case, is selected for examination. In the Nozzle B experiment, steam was supplied to the inlet at the stagnation pressure of 0.25 bar and superheating degree of 20 K. All the details on Nozzle B geometry of is provided in the appendix. The multiphase model applied to resolve the liquid evolution is the discrete-spectrum Eulerian-Lagrangian (E-L) model whose complete description along with other details on the numerical flow calculations are given in chapter 3. The droplet growth rate is calculated by Equation 2.12 for all cases with different values of α which is indicated for each case. Nucleation rates are computed by the standard CNT and its corrected versions by Kantrowitz's factor (Kantrowitz, 1951) and also Courtney's and Kantrowitz's factors together, which are indicated as J_{Kan} and $J_{Kan-Cou}$, respectively. These equations read as

$$J_{Kan} = \frac{1}{(1 + \theta)} J_{CNT} \quad (2.14)$$

$$J_{Kan-Cou} = \frac{1}{5} J_{Kan} \quad (2.15)$$

where θ is dependent merely on temperature as

$$\theta = 2 \frac{\gamma - 1}{\gamma + 1} \frac{h_w}{RT_v} \left(\frac{h_w}{RT_v} - \frac{1}{2} \right) \quad (2.16)$$

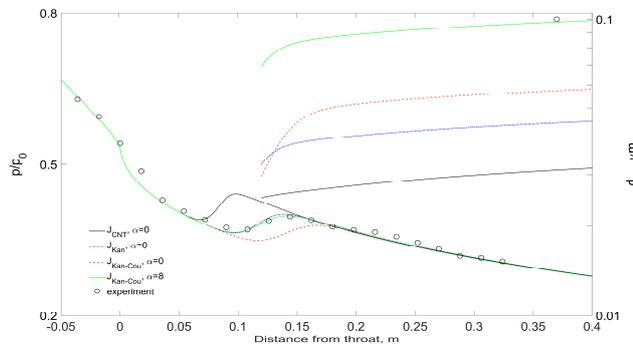


Figure 2.4: Comparison of modelling results for Nozzle B

Figure 2.4 compares the modelling results and experimental measurements for Nozzle B. Note that the pressure distributions are normalized with respect to p_0 being the inlet stagnation pressure. It is clear that the Sauter mean diameters d_{32} from all of the models are smaller than the experimental one except for the model with the augmented droplet growth rate, i.e. $\alpha = 8$. The position of condensation shock is correctly predicted only by J_{Kan} , $\alpha = 0$ and $J_{Kan-Cou}$, $\alpha = 8$. On the other hand, J_{CNT} , $\alpha = 0$ and $J_{Kan-Cou}$, $\alpha = 0$ displace the condensation shock backward and forward, respectively. These backward or forward shifts in the prediction of the location of the condensation shock and also the

misprediction of its magnitude are caused by, first, the excess or lack of interfacial area density being controlled by the nucleation rate, and second, by deficiencies in calculating the droplet growth rate. The only model that matches both the experimental pressure and droplet size is $J_{Kan-Cou}, \alpha = 8$. The success of $J_{Kan-Cou}, \alpha = 8$ is due to two mechanisms. First, reducing the nucleation rate and, therefore, the droplet number density, using Kantrowitz's and Courtney's corrections. Then, compensating the reduction of nucleation rates by enhancing the droplet growth rate, i.e. changing α from 0 to 8.

To further explain how $J_{Kan-Cou}, \alpha = 8$ can correctly predict both pressure and droplet size, it is constructive to start from Young's statement on the link between the wrong prediction of the mean droplet size to the inaccurate calculation of the nucleation rate (Young, 1982). According to Young, if a model accurately matches the measured pressure but fails to correctly predict the mean size of liquid droplets just downstream of the condensation shock, the failure must be attributed to the imprecision in the prediction of the nucleation rate. Therefore, disregarding the fact that in nozzle experiments the droplet size is typically reported for far downstream of the condensation shock, this question is brought up: If the imprecision in the nucleation rate is the origin of inaccuracy in the mean droplet prediction, why would the droplet growth rate need to be enhanced to match the experiment?

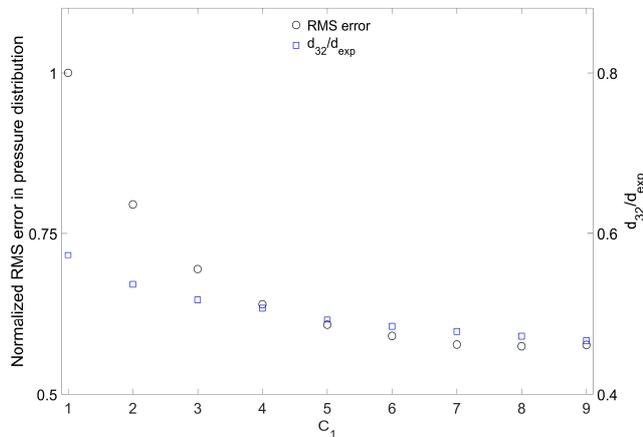


Figure 2.5: RMS error between the predicted and experimental pressures and change in normalised mean diameter for Nozzle B by varying C_1 in $C_1 J_{Kan-Cou}$

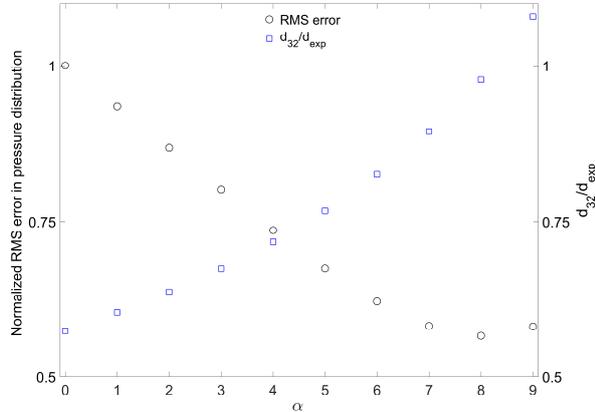


Figure 2.6: RMS error between the predicted and experimental pressure distributions and change in normalised mean diameter for Nozzle B by varying α for $J_{Kan-Cou}$

The answer to the question above is explained with recourse to the inverse correlation between the mean droplet size and the rate of nucleation. This inverse correlation is explained by considering the normalised root-mean-square (RMS) errors of the predicted pressures relative to the measurements when the nucleation rate is changed and the droplet growth rate is kept unchanged as shown in Figure 2.5, and vice versa as shown in Figure 2.6. In the first case, the multiplication of $J_{Kan-Cou}$ by a constant factor, C_1 , reduces the RMS error, but simultaneously leads to increased underprediction of the mean diameter. In other words, increasing the nucleation rate, or equivalently the droplet number density, improves the pressure prediction at the expense of underprediction of the mean diameter, reflected in a decreasing trend of d_{32}/d_{exp} . This inverse correlation impedes consistent agreements with both measured pressure and droplet size in LP wet-steam nozzles by applying a simple reduction/increase factor to CNT (Young, 1982; White & Young, 1993).

In contrast, augmenting the droplet growth by increasing α to $\alpha = 8$ improves predictions for both pressure distribution and the mean droplet size, as shown in Figure 2.6. For $J_{Kan-Cou}$, $\alpha = 8$, the droplet growth rate is increased enough to trigger the condensation shock with a smaller droplet number (or interfacial area) density in comparison to $J_{Kan-Cou}$, $\alpha = 0$. By the same token, as the flow expands, the enhanced droplet growth rate reduces supersaturation at higher rates which, in turn, counterbalances the enhancement of the droplet growth rate. Eventually, the model will be able to furnish the pressure and droplet size distributions in line with the experiment. Therefore, it can be argued that the augmentation introduced by Young to the droplet growth rate can be viewed also, to some extent, as a surrogate for a modification to CNT.

2.5 Link between mean droplet size underprediction and excessive supersaturation dependence of CNT

As discussed before, water nucleation rate measurements especially for the typical temperatures in LP steam turbines show much lesser dependence on supersaturation in comparison with CNT. The consequence of this discrepancy between CNT and the experiment can be comprehended by picturing the relative locations of two curves formed by nucleation rates for an isotherm given by CNT and the experiment, namely two curves with different slopes. At a given supersaturation interval, irrespective of where these curves intersect, the curve with the steeper slope, i.e. that of CNT, overestimates the gap between the nucleation rates of the upper and lower bounds of the supersaturation interval. In other words, the excessive dependence of CNT on supersaturation leads to a bias against nucleation rates in comparatively low supersaturations, and therefore, retards the onset of nucleation. Furthermore, it is noted that for an isotherm, the critical droplet size becomes smaller as supersaturation increases (see Equations 2.8 and 2.9). Therefore, CNT underpredicts the nucleation rate and consequently the fraction of large droplets (formed in comparatively low supersaturation). However, at the same time, CNT overpredicts the nucleation rate and consequently the fraction of small droplets (formed in comparatively high supersaturations). Therefore, it is argued that, in an isothermal nucleation process, the excessive dependence of CNT on supersaturation results in underprediction of the mean droplet size.

However, in contrast to the isothermal nucleation, in practical processes nucleation and droplet growth happen under nonuniform conditions, i.e. nonuniform temperature and supersaturation distributions. Unquestionably, condensation in the steam turbines and nozzles also occurs under nonuniform conditions. Nevertheless, the distinctive attribute of spontaneous nucleation in single-component vapour flows is that although the cooling and expansion rates can differ on a case-to-case basis, the change in temperature is generally much slower compared to the change of supersaturation. In fact, supersaturation responds exponentially to any change in temperature simply because the saturation pressure is an exponential function of temperature. This behaviour of S vs. T over the Nozzle B centreline is depicted in Figure 2.7 for the two models which correctly match the experimental pressure distribution. The direction of flow suggests that during the rapid expansion of steam, as temperature decreases, supersaturation exponentially increases to its highest value, i.e. the Wilson point. Thereafter, by acquiring sufficient supersaturation, the self-quenching characteristic of this flow type brings the vapour state back to the equilibrium. The equilibrium is re-established by the latent heat release which raises the temperature and leads to the exponential decrease in supersaturation.

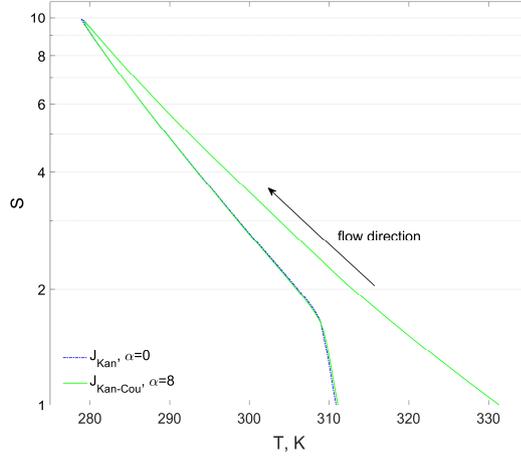


Figure 2.7: S vs. T by models, i.e. J_{Kan} , $\alpha = 0$ and $J_{Kan-Cou}$, $\alpha = 8$, which provide good agreements with the pressure measurements.

Moreover, interestingly from Figure 2.7 it can be argued that regardless of the applied equations for nucleation and droplet growth rates in a model, if the pressure distribution is accurately predicted, the equation of the nucleation rate will be supplied with the correct sets of temperature and supersaturation. Therefore, thinking of the nucleation rate equation as a function of S and T , if a model predicts the correct distribution for pressure (and by the same token correct values for S and T as the arguments of the nucleation function) but an incorrect mean droplet size just downstream of the condensation shock, it can be concluded that the deficiencies come from the function used to calculate the nucleation rate.

2.6 Illustrative examples

To investigate if a nucleation rate equation with lesser dependence on supersaturation is able to improve the droplet size prediction without violating the agreement with the measured pressure, Nozzle B and the experiment number 203 of the study by Moses and Stein (1978) are chosen as test cases. To proceed with the investigation, a new expression for $\Delta G_{g,\sigma}$ different from that of CNT is needed. Thus, a semi-empirical approach using the experimental nucleation rates reported by Brus, et al. (2008) is applied to derive an expression for ΔG^* , which includes $\Delta G_{g,\sigma}$. To the knowledge of the current author, as discussed for Figures 2.1 and 2.2, the work by Brus, et al. (2008) is the only available experimental study on water nucleation rates which includes the temperatures of interest in LP wet-steam flows. The values of g_{exp}^* from the experiment are used to derive an equation for the critical cluster molecular content in the form of a function of temperature and supersaturation.

Thereafter, this equation for g^* is employed to estimate the free energy barrier to the formation of the critical cluster. According to Equation 2.8, it is deduced that g^* can be expressed as

$$g^* = \frac{2f(T_v)}{(\ln(S))^3} \quad (2.17)$$

in which $2f(T_v)$ is a function that substitutes all of the variables dependent on temperature alone, i.e.

$$2f(T_v) = \left(\frac{2A_1\sigma}{3k_B T_v}\right)^3. \quad (2.18)$$

In addition, by substituting $\Delta G_{g,\sigma}$ from Equation 2.4 in Equation 2.3, the change in the Gibbs free energy to form the critical cluster is directly linked to g^* as

$$\frac{\Delta G^*}{k_B T_v} = \frac{\ln(S)}{2} g^* + \ln(S). \quad (2.19)$$

Equations 2.17 and 2.19 are used to substitute ΔG^* in Equation 2.1, and by incorporating Kantrowitz's correction factor, a semi-empirical relation for the nucleation rate, indicated by J_{se} , is given as

$$J_{se} = \frac{1}{s} \frac{K}{(1+\theta)} \exp\left(-\frac{f(T_v)}{(\ln(S))^2}\right). \quad (2.20)$$

According to Equation 2.17, $f(T_v)$ for each isotherm nucleation measurement is computed as $f(T_v) = (1/2)g_{exp}^* \ln(S)^3$. Table 2.1 compares the theoretical (based on CNT) and experimental values of g^* and $f(T_v)$ at 290 K and 300 K.

Table 2.1: g^* and $f(T_v)$ from CNT and experiment.

	Isotherm, K	$\ln(S)$	g^*	$f(T_v)$
exp	290	1.375	43.740	56.873
CNT			70.678	91.899
exp	300	1.270	44.611	45.679
CNT			76.680	78.516

For temperatures between 290 K and 300 K, $f(T_v)$, to be used in J_{se} , is estimated by the linear interpolation

$$f(T_v) = -1.119T_v + 381.480. \quad (2.21)$$

For temperatures above 300 K, i.e. between 300 K and 310 K and between 310 K and 320 K, similar relations for $f(T_v)$ are obtained from the experimental values. For temperatures below 290 K, because no measurement is reported in the experiment, Equation 2.21 is extrapolated to estimate $f(T_v)$. As it can be seen in Table 2.1, the experimental values of $f(T_v)$ are considerably smaller than the theoretical ones from CNT. Considering the exponential term in Equation 2.20, the smaller experimental $f(T_v)$ also suggests the dependence of CNT on supersaturation is excessively strong.

Leaving aside the inevitable inaccuracy introduced by the linear approximation, the semi-empirical is theoretically justified as it follows CNT in essence and $2f(T_v)$ only replaces temperature-dependent variables in ΔG^* . It is interesting to note that the experimental $f(T_v)$ leads to a smaller ΔG^* indicating that CNT overestimates ΔG^* . Nevertheless, the debate about the underestimation or overestimation of ΔG^* by CNT is still open. For example, the empirical correction to CNT proposed by Wölk, et al. (2002) suggests that the actual free energy barrier is smaller for temperatures above 238 K compared to CNT. Likewise, the work by Ten Wolde, et al. (1998) states that underestimation of ΔG^* by CNT results in the overprediction of nucleation rates. To add to the confusion, there are other works, such as those by Schmelzer, et al. (2006) and Chen, et al. (2001), expressing the opposite view that CNT overestimates ΔG^* . It is emphasised that it is not claimed that the simple approach employed here can provide an accurate estimation for ΔG^* . Instead, the only purpose of the semi-empirical approach is to provide a tool to assess the influence of the supersaturation dependence of the nucleation rate on the droplet size prediction in real test cases.

2.6.1 Nozzle B

Two more models are chosen for comparison with J_{Se} to highlight the impact of reducing the supersaturation dependence on the prediction of the mean droplet size. These two models are the corrected versions of CNT which, as shown in Figure 2.4, accurately predict the pressure distribution in Nozzle B, i.e. J_{Kan} , $\alpha = 0$ and $J_{Kan-Cou}$, $\alpha = 8$. It is of vital importance to ascertain that all models give pressure distributions as close to each other as possible to make a meaningful comparison regarding the mean droplet size prediction. For the same reason, J_{Se} must also be calibrated to give a pressure distribution as close as possible to the experiment. Thus, while keeping $\alpha = 0$ in the droplet growth equation, a constant multiplier for J_{Se} is sought, which minimizes the RMS errors between the predicted and measured pressures. To be specific, the measured pressure in the nozzle experiment is employed merely as a condition to force all models to conform to the same pressure pattern. The normalized RMS errors by applying different multipliers C_2 to J_{Se} are shown in Table 2.2. The lowest error is obtained reducing J_{Se} by a factor of 0.003. Figure 2.8 depicts nucleation rates by J_{Kan} and $(0.003)J_{Se}$, for 290 K and 300 K. The $(0.003)J_{Se}$ curves exhibit a much gentler slope and higher rates for low

supersaturations compared to those of J_{Kan} as a result of a lower ΔG^* and lesser dependence on S .

Table 2.2: Normalised RMS errors in the predicted pressure distributions by $C_2 J_{Se}$, $\alpha = 0$

C_2	0.002	0.0025	0.003	0.0035	0.004
RMS	0.9673	0.9670	0.9565	0.9735	1.0000

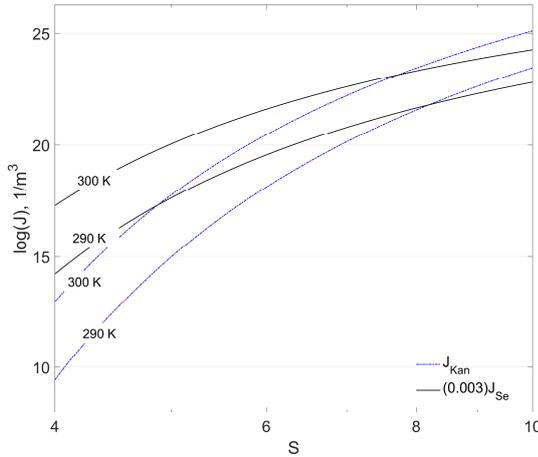


Figure 2.8: Nucleation rates at 290 K and 300 K by $(0.003)J_{Se}$ and J_{Kan} .

Regardless of errors in the experimental measurements, numerous uncertainties over CNT and also droplet growth warrant using different correction or tuning factors to provide agreement with the measurements. Thus, utilising tuning factors to adjust the CNT has been found necessary in many studies. Most of these factors were either directly applied to the surface tension, such as in the work of Kermani and Gerber (2003), or were related to the imprecision caused by the planar surface tension, such as in the study by Simpson and White (2005). Nonetheless, it is noteworthy that the immediate outcome of any modification to the surface tension is an alteration in the critical cluster size (see Equation 2.8 or 2.17), which will be also reflected as a change in CNT dependence on supersaturation (see Equation 2.6 or 2.20). The current author does not attribute any physical significance to the obtained calibration factor for J_{Se} , as it is not necessary considering the aim of calibrating J_{Se} . As explained earlier, the only aim of the calibration process is to obtain conditions (similar pressure distributions) for all models to draw a fair comparison between the predicted mean droplet sizes.

Figure 2.9 compares the results of J_{Kan} , $\alpha = 0$ and $(0.003)J_{Se}$, $\alpha = 0$ along with $J_{Kan-cou}$, $\alpha = 8$. The mean droplet size using $(0.003)J_{Se}$ is considerably increased, by around 30%, compared to J_{Kan} , $\alpha = 0$. This improvement in the mean droplet size prediction is solely caused by a reduction of the supersaturation dependence in $(0.003)J_{Se}$

as the droplet growth rate is kept at its lowest, $\alpha = 0$, to zero for both J_{Kan} and $(0.003)J_{Se}$. As shown in Figure 2.3, decreasing α significantly reduces the droplet growth rate. Thus, it is concluded that lowering the dependence on S in $(0.003)J_{Se}$ can compensate, to some extent, for the decrease of the droplet growth rate when $\alpha = 0$.

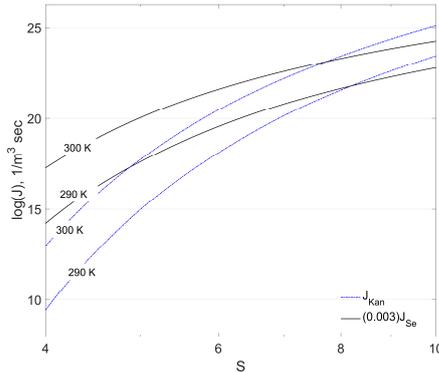


Figure 2.9: Comparison of pressure and droplet mean diameter J_{Kan} , $J_{Kan-Cou}$ and $(0.003)J_{Se}$ for Nozzle B.

To explain how the semi-empirical nucleation rate equation can increase the mean droplet size, it is helpful to consider Figure 2.10, which shows the mass-based nucleation rates and droplet number density, indicated by N , over the Nozzle B centreline. The benefit of treating the number density per unit of mass as opposed to per unit of volume comes from the fact that mass is a conserved quantity, and by using mass-based variables in rapid expansions, the impact of density gradients is separated from the concentration of droplets (White & Young, 2008). As illustrated in Figure 2.10, the lesser dependence on S in $(0.003)J_{Se}$ widens the zone of nucleation and enlarges the droplet number densities upstream of the Wilson point. On the other hand, using J_{Kan} , $\alpha = 0$, the nucleation zone contracts with a higher peak, which means Simpson & White the nucleation of smaller critical droplets but at higher rates in comparison with $(0.003)J_{Se}$. For $J_{Kan-Cou}$, $\alpha = 8$, the augmentation of the droplet growth rate compensates for the decrease of the nucleation rate and enables the equilibrium re-establishment with much lower nucleation rates, and thus, a larger mean droplet size compared to the other models. This compensating effect of the augmented growth rate is also clearly detectable in the form of reduced droplet number density. For $(0.003)J_{Se}$, nucleation initiates faster compared to the two other models, and it also ends faster compared to J_{Kan} , $\alpha = 0$, which employs an identical value for α .

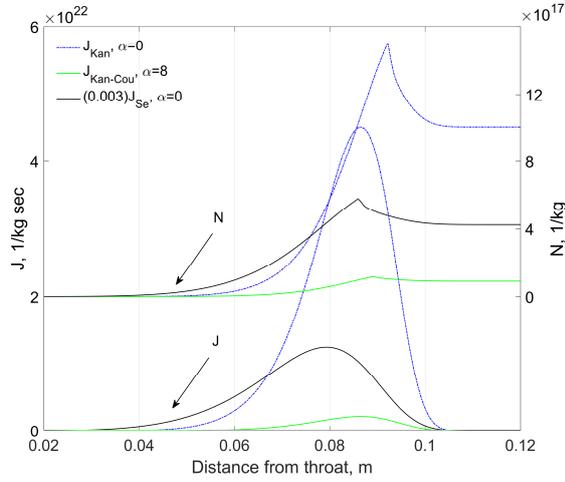


Figure 2.10: Nucleation rates and droplet number densities by J_{Kan} , $J_{Kan-Cou}$ and $(0.003)J_{Se}$ over Nozzle B centreline.

Figure 2.11 shows distributions of the wetness proportion over the droplet size spectrum at different locations in Nozzle B. For the model benefiting from the enhanced droplet growth rate, the liquid phase always consists of droplets which, on average, are larger compared to the other two models. Between J_{Kan} , $\alpha = 0$ and $(0.003)J_{Se}$, $\alpha = 0$, the semi-empirical model always gives larger droplets with greater proportions of wetness fractions compared to J_{Kan} , although in both models $\alpha = 0$. The increase in the nucleation rates applying $(0.003)J_{Se}$, which happens for lower supersaturations upstream of the Wilson point, reduces the value of supersaturation attained at the Wilson point (see Figure 2.12). Thus, the total droplet number density and nucleation peak are prevented from rising abnormally contrary to J_{Kan} , $\alpha = 0$. In other words, the role of an enhanced growth rate, through increasing α , is partially compensated by raising nucleation rates in favour of larger critical droplets in $(0.003)J_{Se}$. It should be noted that the size spectra of liquid droplets are resolved down to the local critical sizes assuming that droplets smaller than the local critical radius evaporate. The effect of this assumption can be seen as the vertical lines (cut-offs) in Figure 2.11 (c) and (d).

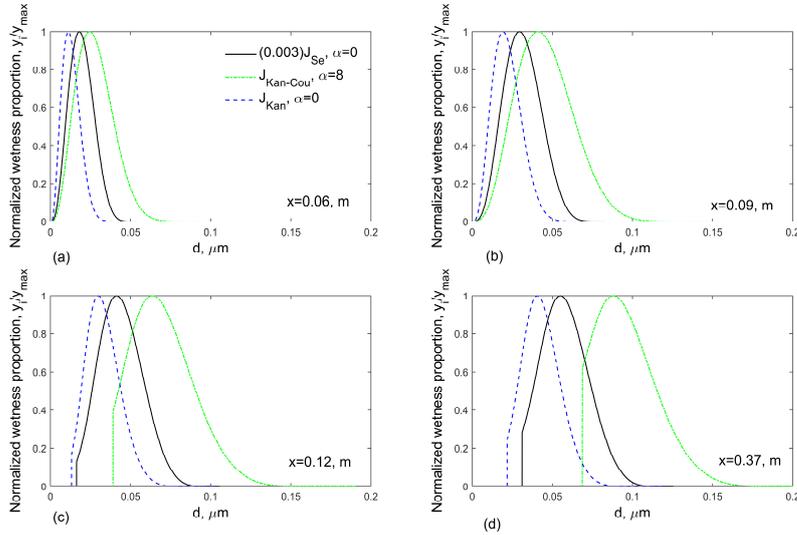


Figure 2.11: Distributions of normalised liquid proportion over droplet size spectra by J_{Kan} , $J_{Kan-Cou}$ and $(0.003)J_{Se}$ at different streamwise locations downstream of Nozzle B throat.

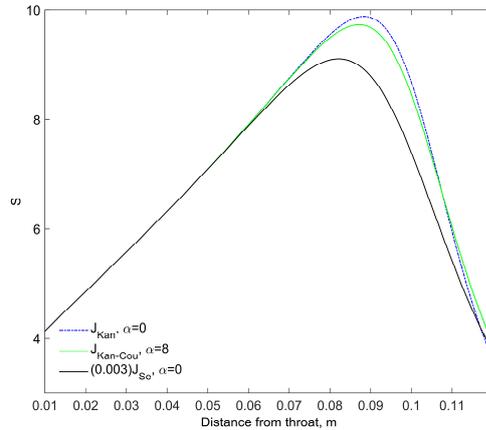


Figure 2.12: Comparison of supersaturation distributions J_{Kan} , $J_{Kan-Cou}$ and $(0.003)J_{Se}$ over Nozzle B centreline

2.6.2 Experiment 203

Moses and Stein performed several experiments by applying different stagnation pressures and temperatures to a single nozzle inlet. See the appendix for the information about the geometry of Moses and Stein nozzle. One of their LP experiments for which both droplet size and pressure measurements are available is the experiment number 203 (Exp. 203), with a stagnation pressure and a temperature of 0.358 bar and 368.3 K, respectively. Contrary to Nozzle B, in the case of Exp. 203 $J_{Kan}, \alpha =$

0 and $J_{Kan-Cou}$, $\alpha = 8$ cannot give a reasonably accurate agreement with the pressure measurement. Therefore, to provide the conditions for a fair comparison, the models are calibrated to predict pressure distributions as close as possible to each other. The calibration factors and normalised RMS errors are given in Table 2.3. For $\alpha = 0$, $C_3 J_{Kan}$ and $C_4 J_{Se}$ lead the lowest errors by setting C_3 and C_4 to 50 and 0.32, respectively. Moreover, augmenting the droplet growth rate results in the lowest RMS error at $\alpha = 13$ for $J_{Kan-Cou}$.

Figure 2.3: Normalised RMS errors in predicted pressure distributions

$C_3 J_{Kan}, \alpha = 0$					
C_3	42	46	50	54	58
RMS error	1.0000	0.9625	0.9455	0.9477	0.9602
$C_4 J_{Se}, \alpha = 0$					
C_4	0.24	0.28	0.32	0.36	0.40
RMS error	1.0000	0.8245	0.7295	0.7395	0.7745
$J_{Kan-Cou}$					
α	10	11	12	13	14
RMS error	1.0000	0.7778	0.5263	0.2955	0.3838

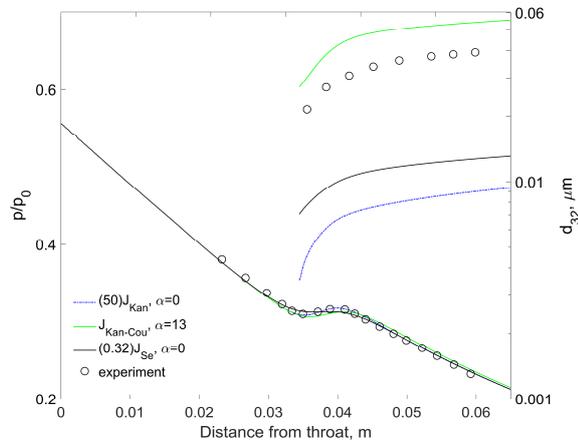


Figure 2.13: Comparison of the models with the lowest RMS errors for Exp. 203

Figure 2.13 compares the results with the lowest RMS errors from each model. As shown in Figure 2.13, all of the models fail to accurately predict the mean droplet size distribution. Expectedly, the model with an enhanced droplet growth rate gives the largest droplet diameters – even larger than the measurements. The important matter is that between $(50)J_{Kan}$, $\alpha = 0$ and $(0.32)J_{Se}$, $\alpha = 0$, the semi-empirical model can predict mean droplet sizes on average around 43% larger than the other model owing to the faster start and end of nucleation. The earlier onset of nucleation becomes obvious by

comparing nucleation rates and droplet number densities between the models with $\alpha = 0$ in Figure 2.14. The interesting point is that this stronger initiation of nucleation not only does not reduce the mean droplet size but also results in an increase in the mean droplet size by quenching the nucleation faster and consequently decreasing the droplet number density.

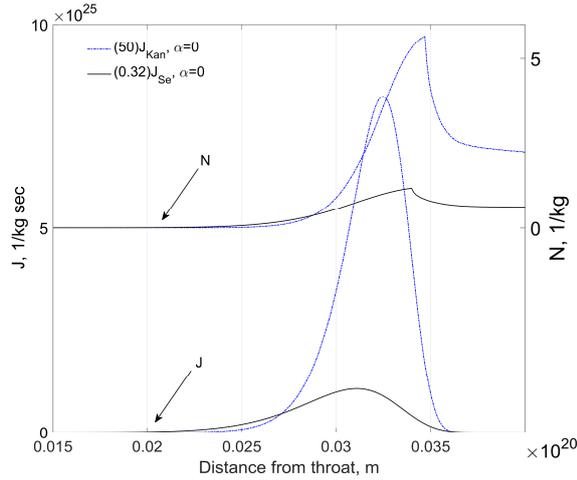


Figure 2.14: Comparison of nucleation rates and droplet number densities by $(50)J_{Kan}$, $\alpha = 0$ and $(0.32)J_{Se}$, $\alpha = 0$ for Exp. 203.

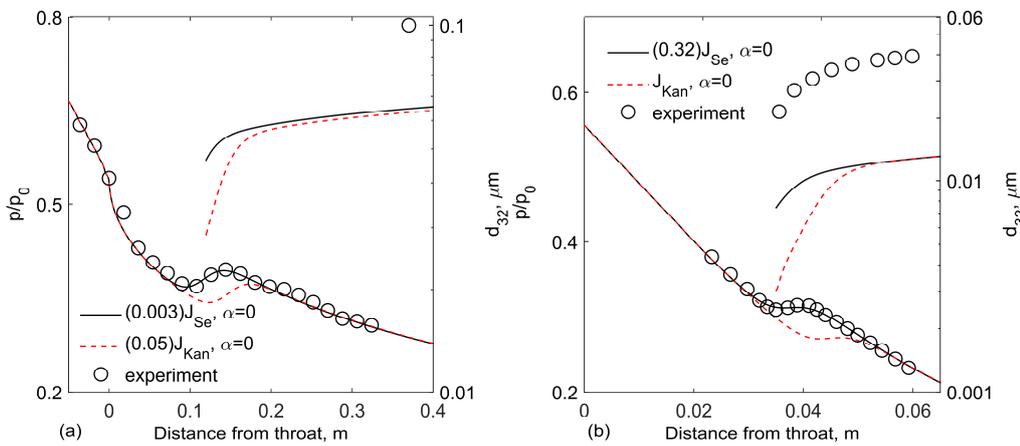


Figure 2.15: Comparison of semi-empirical equation and J_{Kan} calibrated to predict equal mean droplet sizes by applying simple reduction factors, (a) Nozzle B, (b) Exp. 203.

To sum up, for both Nozzle B and Exp. 203, the milder dependence of J_{Se} on supersaturation leads to a larger mean droplet size by increasing nucleation rates in a comparatively low S and decreasing nucleation rates in a comparatively high S . In

addition, increasing nucleation rates of comparatively large droplets before the Wilson point lowers the attainable supersaturation at the Wilson point, and hence indirectly diminishes nucleation rates of comparatively small droplets which are nucleated in the vicinity of the Wilson point. Although, at first look, the growth of the mean droplet sizes through the semi-empirical equation might appear not particularly considerable, it should be reiterated that it is impossible to increase the mean droplet size by merely reducing the nucleation rate without violating the agreement with the measured pressure. As illustrated in Figure 2.15, simple reduction factors to the nucleation rate can increase the mean droplet size to similar values as predicted by the semi-empirical equation in both test cases but at the expense of failure in predicting the correct pressure distribution. Nevertheless, irrespective of the equation applied for nucleation rate, it is clear that the droplet growth rate still needs to be augmented to quench the nucleation more quickly and perfectly predict the mean diameter. This issue has been pointed out also in several other works. For example Sinha, et al. (2009) and Pathak, et al. (2013) observed that increasing the droplet growth rate by invoking the isothermal assumption could quench nucleation faster and predict mean droplet diameters larger and closer to the measurements. However, the latter work reported significant temperature deviations between the liquid droplets and the vapour. Furthermore, as discussed earlier, Young (1982) also proposed enhancing the droplet growth rate as a solution to the underprediction of the mean droplet size in LP wet-steam flows. However, to the knowledge of the author, thus far no reliable evidence has been found to support the augmentation of the droplet growth rate on the grounds addressed by Young. In view of the current work, the most important point is that it is also possible to quench nucleation faster compared to CNT by rectifying the supersaturation dependence of the nucleation rate equation. This was formerly considered impossible, owing to the inverse correlation between the nucleation rate and the mean droplet size.

3 Dispersed multiphase flow models

This chapter encompasses (in section 3.1) details on the numerical solution to the transport equations and (in sections 3.2-4) descriptions of DMFMs which are used in all Publications.

Experimental measurements in wet-steam turbines have shown very broad and skewed size distributions for the liquid droplets (Walters, 1987; Walters, 1988). Particularly, in large LP steam turbines, droplets which are nucleated in turbine initial stages have sufficient time to grow in the following stages to sizes larger than one micron with substantial inertial relaxation times resulting in wide and complex droplet size spectra and also the divergence in liquid and vapour path lines (Gerber & Mousavi, 2007). Moreover, heat and momentum transfer processes between the liquid droplets and steam are strongly dependent on the droplet size. Therefore, to accurately model the flow behaviour of the liquid-gas mixture and the loss mechanism due to non-equilibrium transfer processes, it is of crucial importance to take the polydispersity of the liquid droplets into account. Accordingly, the main focus here is on how the presented DMFMs can handle polydispersity.

3.1 Transport equations

For validating a DMFM based on the experiment, it is advantageous to choose test cases with a minimised number of uncertainty sources to focus only on the essential constituents of the model. In this respect, supersonic wet-steam nozzle experiments are viewed as very popular validation test cases. The reason of this popularity is that the flow behaviour in these nozzles is not complex and allows transport equations to be cast in simple frameworks, such as the Euler equation set. Hence, the deficiencies in results can be conveniently traced back to the main components of the employed DMFM.

By disregarding the slip velocity between the liquid droplets and vapour and also the liquid partial pressure, the transport equation set of the vapour-liquid mixture transforms to that of a single phase fluid. Neglecting the relative acceleration between the droplets and vapour is a proper assumption considering the fact that droplets formed by homogenous nucleation are extremely small (smaller than one micro meter) with a marginal inertial relaxation time. Therefore, for viscous-free flows, the transport equations in a one-dimensional domain along the Cartesian coordinate X read as

$$\frac{\partial}{\partial t} \begin{bmatrix} \rho_m A \\ \rho_m u A \\ \rho_m E_m A \end{bmatrix} + \frac{\partial}{\partial X} \begin{bmatrix} \rho_m u A \\ (\rho_m u^2 + p_v) A \\ \rho_m u H_m A \end{bmatrix} = \begin{bmatrix} 0 \\ p \frac{dA}{dX} \\ 0 \end{bmatrix} \quad (3.1)$$

where A is the cross-sectional area, m is a subscript to denote the mixture properties, u is the velocity, E is the total internal energy and H is the total enthalpy. For a given wetness

fraction Y , by ignoring the extremely small volume fraction of liquid, the mixture properties are calculated from vapour and liquid properties as below

$$\rho_m = \frac{\rho_v}{1 - Y} \quad (3.2)$$

$$E_m = YE_l + (1 - Y)E_v \quad (3.3)$$

$$H_m = YH_l + (1 - Y)H_v. \quad (3.4)$$

3.1.1 Numerical discretisation schemes

The Advection Upstream Splitting Method (AUSM) flux splitter scheme, introduced by Liou and Steffen (1993) is employed to solve the discretised form of Equation 3.1 in the context of the finite volume method. The AUSM is based on the decomposition of the convective flux vector \mathbf{C} into a pressure part and a convective part. These two parts are computed by separating the variables at the computational cell faces based on the left and right states of each cell face. As specified by Van Leer (1997), the pressure part is calculated as the sum of a positive pressure and a negative pressure associated with the cell face left and right states, respectively. These negative and positive pressures are functions of Mach numbers and pressures for the right and left states of the cell face as shown below

$$p_L^+ = \begin{cases} p_L & \text{if } M_L \geq 1 \\ \frac{p_L}{4}(M_L + 1)^2(2 - M_L) & \text{if } |M_L| < 1 \\ 0 & \text{if } M_L < -1 \end{cases} \quad (3.5)$$

$$p_R^- = \begin{cases} 0 & \text{if } M_R \geq 1 \\ \frac{p_R}{4}(M_R - 1)^2(2 + M_R) & \text{if } |M_R| < 1 \\ p_R & \text{if } M_R < -1 \end{cases} \quad (3.6)$$

where the subscripts L and R indicate the left and right states and M is the Mach number. The convective part in the AUSM is computed using the primitive variables (ρ , u , E and H) of either the left state or the right state of the cell face, depending on the sign of the so-called advection Mach number denoted by M_a . As with the pressure part, the advection Mach number is also given by the summation of a positive and a negative Mach number, i.e. $M_a = M_L^+ + M_R^-$, which are formulated as

$$M_L^+ = \begin{cases} M_L & \text{if } M_L \geq 1 \\ \frac{1}{4}(M_L + 1)^2 & \text{if } |M_L| < 1 \\ 0 & \text{if } M_L < -1 \end{cases} \quad (3.7)$$

$$M_R^- = \begin{cases} 0 & \text{if } M_R \geq 1 \\ \frac{-1}{4}(M_R - 1)^2 & \text{if } |M_R| < 1 \\ M_R & \text{if } M_R < -1 \end{cases} \quad (3.8)$$

The positivity or negativity of M_a determines whether fluid particles flow from west to east or vice versa. The sign of M_a is ascertained introducing two numerical velocities for the left and right states of the cell face as follows

$$U_{L,I+1/2}^+ = [M_a + |M_a|]c_L \quad (3.9)$$

$$U_{R,I+1/2}^- = [M_a - |M_a|]c_R \quad (3.10)$$

where c is the frozen speed of sound in the mixture. Finally, the convective flux vector at the east face of the I^{th} computational cell $\mathbf{C}_{I+1/2}$ is written as

$$\mathbf{C}_{I+1/2} = \frac{1}{2} \left(U_L^+ \begin{bmatrix} \rho_m c \\ \rho_m c u \\ \rho_m c H_m \end{bmatrix}_L + U_R^- \begin{bmatrix} \rho_m c \\ \rho_m c u \\ \rho_m c H_m \end{bmatrix}_R \right) + \begin{bmatrix} 0 \\ p_L^+ + p_R^- \\ 0 \end{bmatrix}. \quad (3.11)$$

The convective flux vector at the west face, i.e. $\mathbf{C}_{I-1/2}$, is also given in the same way. The primitive variables for the left and right states are computed using interpolated conservative variables from the cell centres by employing the Monotonic Upstream-Centred Scheme for Conservation Laws (MUSCL) proposed by Van Leer (1979). For instance, for the cell face $I + 1/2$, the values of density for the left and right states are given as,

$$\rho_L = \rho_I + \frac{1}{4} [(1+k)(\rho_{I+1} - \rho_I) + (1-k)(\rho_I - \rho_{I-1})] \quad (3.12)$$

$$\rho_R = \rho_{I+1} - \frac{1}{4} [(1-k)(\rho_{I+2} - \rho_{I+1}) + (1+k)(\rho_{I+1} - \rho_I)] \quad (3.13)$$

in which k determines the order of accuracy in spatial discretisation, $k = 0$ leads to a second-order upwind-biased discretisation, $k = 1/3$ provides a third-order upwind-biased discretisation and $k = 0$ results in a fully one-sided second-order upwind-biased discretisation. For the second order and third order, MUSCL is stabilised by the flux limiter functions derived by Roe (1986) and Koren (1993), respectively.

3.1.2 Thermodynamics properties

For practical temperature and pressure ranges in wet-steam turbines, the behaviour of steam considerably deviates from the ideal gas assumption necessitating the use of a real gas equation of state (EOS). Formerly, the tendency was towards applying simpler real gas EOSs, such as those proposed by Young (1992), to retain the computational costs

manageable. However, due to the introduction of a tabulated method of storing and interpolating the thermodynamics properties by Hill et al. (2000) and also the advancement in computational power, more complicated EOSs, such as formulations given by Vukalovich (1958), Young (1988) and IAPWS (2007), can be used in wet-steam flow modelling. It was demonstrated by Bakhtar and Piran (1979) that virial coefficients in Vukalovich's EOS are well-behaved under extrapolation into the metastable, discarding the need for modifications. Therefore, in this thesis and its Publications, Vukalovich's EOS is applied to calculate water vapour properties. To minimise the thermodynamic inconsistency between the liquid and vapour properties, the Clausius-Clapeyron relation along with the empirical relation for saturation pressure as a function of temperature, given by Keenan et al. (1978), is used to calculate the saturation enthalpy of water liquid. Moreover, the equations, given by Young (1982), are employed to compute the density and planar surface tensions of liquid water, respectively.

3.2 Moment-based models

To describe the moment-based models, it is necessary to first explain the concept of a particle phase space (PPS) on which all variations of the MOM are based. A PPS provides the framework for describing the distribution and dynamics of a particulate/dispersed phase. To track the particle distribution over the spatial coordinates and also properties of the particle itself, a PPS comprises two coordinate types: external and internal. The external coordinates correspond to the spatial coordinates, i.e. X , Y and Z . The internal coordinates are introduced to take account of variations in particle distribution with respect to particle characteristics such as size, velocity and shape. Assuming that all particles are spherical and travel at the same velocity with the continuous phase, the number of internal coordinates reduces to one which is the radius coordinate. Therefore, the PPS comprises a four-dimensional space expanding over the coordinates X , Y , Z and r . In addition, the particle number density function (NDF), denoted by f , is utilised to describe the presence of particles in the PPS in terms of an intensive quantity. In other words, the number of particles per unit mass of mixture with radii spanning from r to $r + dr$ is given by $\int f dr$. By the same token, the total number of droplets per unit of mass is also given by $\int \rho_m dV$, where dV is an elemental volume of the PPS, i.e. $dV = dX dY dZ dr$.

Using the concepts above, the conservation of mass for the liquid phase (particulate phase) can be easily codified in terms of the population balance equation of the liquid droplets. In the absence of droplet breakage and coalescence, the population balance equation takes a familiar form of a transport equation for f in the PPS:

$$\frac{\partial}{\partial t}(\rho_m f) + \nabla \cdot (\rho_m f u) + \frac{\partial}{\partial r}(\rho_m f u_r) = \rho_m J \quad (3.14)$$

in which u_r is the velocity over the internal dimension r in the PPS. In fact, u_r is the droplet growth rate and equal to \dot{r} .

The main drawback to solving Equation 3.14 in its current form is that f is not known a priori. However, in the majority of practical problems, working with the complete information of NDF, if available, is not necessary. In most practical problems, information on a few first moments of the droplet size distribution suffice to track the interfacial transfer processes between the vapour and liquid droplets. The moments of a distribution, denoted by μ , are related to f as follows:

$$\mu_j = \int r^j f dr \quad (3.15)$$

in which j indicates the moment index. To eliminate f , Equation 3.15 is incorporated into Equation 3.14. Thus, the liquid phase conservation can be represented in terms of a set of moment-transport equations with the following form:

$$\frac{\partial}{\partial t} (\rho_m \mu_j) + \nabla \cdot (\rho_m \mu_j u) = \rho_m J r^{*j} + j \rho_m \int r^{j-1} u_r f dr \quad (3.16)$$

(see (Randolph & Larson, 1988) or (White & Hounslow, 2000) for mathematical derivation). Typically, only the transport equations of the four first moments need to be solved. These four moments encompass all of the essential physical characteristics of the dispersed phase:

1. The zeroth moment, $\mu_0 = \int f dr$, is equal to the mass-based droplet number density.
2. The first moment, $\mu_1 = \int r f dr$, amounts to the sum of the radii of all droplets per unit of mass.
3. The second moment, $\mu_2 = \int r^2 f dr$, is proportional to the total surface area of droplets per unit of mass.
4. The fourth moment, $\mu_3 = \int r^3 f dr$, is proportional to the total volume occupied by the droplets per unit of mass.

However, as it can be seen in Equation 3.16, f still appears inside the integral on the RHS of the equation. The CMOM and QMOM apply different approaches to eliminate f entirely from the moment-transport equations which are described subsequently in the rest of this chapter.

3.2.1 Conventional method of moments

As shown by Hulburt and Katz (1964), to close the moment-transport equations without any recourse to the NDF, in the CMOM, an idealised form has to be employed for the droplet growth rate. This idealised form of u_r can be represented as

$$u_r = a + br \quad (3.17)$$

where a and b are only functions of vapour properties and independent of r . Based on the features of the droplet growth process, various forms for a and b can be considered. A detailed comparison between several functions for a and b is provided by White (2003). The most common selection in wet-steam modelling, as in studies by Hill (1966), Simpson & White (2005) and Halama & Fort (2012), is to set $b = 0$, and computing the droplet growth rate $u_r = a$ for the surface-area-averaged radius $r_{20} = (\mu_2/\mu_0)^{1/2}$. This means that the size distribution of droplets is ignored in modelling their growth, and all droplets (f) grow (travel) with the same rate (velocity) $u_r = a$ (in the PPS). As a consequence, the moment-transport equations are solved without recourse to f by only using moments themselves in a recursive manner as follows:

$$\frac{\partial}{\partial t} (\rho_m \mu_j) + \nabla \cdot (\rho_m \mu_j u) = \rho_m J r^{*j} + j \rho_m \mu_{j-1} a \quad (3.18)$$

in which a is calculated by Equation 2.12 for $r = r_{20}$. In all Publications, for the CMOM, the moment-transport equations in the above form are solved. It should be noted to retain consistency with Publication II, in chapter 4 the terms CMOM and MOM are used interchangeably.

3.2.2 Quadrature method of moments

The QMOM, introduced by McGraw (1997), offers a distinctive advantage over the CMOM in terms of respecting the droplet size distribution in modelling the droplet growth. The main idea of the QMOM comes from reconstructing the continuous NDF by the weighted sum of Dirac delta functions using n -point Gaussian quadrature in a discretised fashion, i.e.

$$f \approx \sum_{i=1}^n w_i \delta(r - r_i) \quad (3.19)$$

where i is the quadrature index and n determines the accuracy or the number of quadrature points and also the dimension of the moment set, i.e. $2n$, for which the weights and radii are calculated. In the QMOM, moments are represented in terms of summations over n products of weights, w_i , and radii, r_i , as below

$$\mu_j = \sum_{i=1}^n r_i^j w_i. \quad (3.20)$$

By introducing moments from Equation 3.20 into Equation 3.16, the closure to the moment-transport equations is given as

$$\frac{\partial}{\partial t} (\rho_m \mu_j) + \nabla \cdot (\rho_m \mu_j u) = \rho_m J r^{*j} + \rho_m j \sum_{i=1}^n r_i^{j-1} \dot{r}_i w_i. \quad (3.21)$$

Figure 3.1 schematically shows the discrete reconstruction of size distribution through a four-point Gaussian quadrature in comparison to the continuous size distribution. It can be seen that, in contrast to CMOM, for QMOM each element of the discretised size distribution has its own unique velocity (droplet growth rate) along the r coordinate in the PPS.

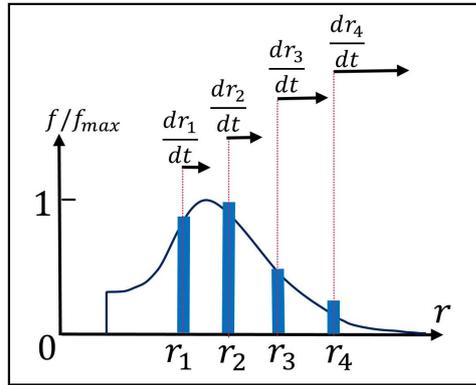


Figure 3.1: Discrete size distribution using Gaussian quadrature

For a given moment set, the direct way to calculate weights and radii is to find the roots of a non-linear system, formed by $2n$ known moments and $2n$ unknowns consisting of n sets of radius and weight as follows:

$$\begin{bmatrix} 1 & 1 & \dots & 1 \\ r_1 & r_2 & \dots & r_n \\ \vdots & \vdots & \dots & \vdots \\ r_1^{2n-1} & r_2^{2n-1} & \dots & r_n^{2n-1} \end{bmatrix}_{2n \times n} \times \begin{bmatrix} w_1 \\ w_2 \\ \vdots \\ w_n \end{bmatrix}_{n \times 1} = \begin{bmatrix} \mu_0 \\ \mu_1 \\ \vdots \\ \mu_{2n-1} \end{bmatrix}_{2n \times 1}. \quad (3.22)$$

An iterative method is required to solve the system above, and because the problem is naturally ill-conditioned, it is highly sensitive to the initial solutions. As shown by Press, et al. (1992), this issue can be sidestepped by first calculating the recursion coefficients of orthogonal polynomials with respect to f . Then, the radii and weights are found by solving the eigenvalue problem of the so-called Jacobi matrix – a symmetric ($n \times n$) tridiagonal whose elements are the recursion coefficients of the orthogonal polynomials.

The procedure for calculating recursion coefficients of the orthogonal polynomials, to form the Jacobi matrix, is called the moment-inversion algorithm. The QMOM robustness and efficiency strongly relies on the performance of the moment-inversion algorithm. Two commonly used algorithms are Wheeler and the product-difference, given by Gordon (1968) and Wheeler (1974), respectively. In Publications II and III, Wheeler's

algorithm is applied to the QMOM due to its strong stability compared to the other algorithms, such as the product-difference. A detailed discussion on the product-difference and Wheeler's algorithms can be found in the study by Marchisio and Fox (2013). The QMOM accuracy can be elevated by increasing the number of quadrature points since a larger n entails more sets of radii and weights to reconstruct the NDF. As the number of moment-transport equations which have to be solved is double the number of quadrature points, the computational cost significantly rises as n increases. Therefore, a balance between the required accuracy and computational cost should be sought. It is suggested by Marchisio et al. (2003) that a Gaussian quadrature with three points can provide the desirable balance. In Publications II and III, the QMOM results are obtained by the three-point quadrature, which means that the droplet size distribution is resolved using three sets of radii and weights.

3.2.3 Moment-based models in a Lagrangian reference frame

The form of moment transport presented by Equation 3.18 for the MOM (and also 3.21 for the QMOM) suggests an Eulerian framework as a natural candidate to work with. However, by applying the continuity law to the moment-transport equations, they can be recast in the following form to track the moments in a Lagrangian frame of reference:

$$\frac{D}{Dt}(\mu_j) = Jr^{*j} + j\rho_m\mu_{j-1}a \quad (3.23)$$

where D denotes the material derivative. In Publication IV, a Lagrangian module is employed to numerically integrate the evolution of moments along the streamline. This module is identical to the one presented in the following section except for the droplet growth rate, which in the CMOM is calculated for r_{20} .

3.3 Discrete-spectrum Eulerian-Lagrangian model

The E-L model used in Publication II is quite similar to the one presented by Young (1992). This model consists of a Lagrangian tracking module which is entirely decoupled from the flow solver which works in an Eulerian framework. This module only receives the pressure distribution from the flow solver to track the evolution of the wetness along the streamline. The module represents the continuous droplet size distribution by means of a finite number of droplet bins. The generation of fresh liquid droplets through nucleation along the streamline is monitored, and when the nucleation rate exceeds an arbitrary limit, a new group of droplets is added to the calculation.

Since the number of droplet groups can be theoretically limitless, as mentioned earlier, a finite number of bins are used to group droplets falling in the same size range. Therefore, the total wetness fraction is given by the sum of contributions by all of the bins as

$$Y = \sum_{i=1}^K y_i = \sum_{i=1}^K \frac{4}{3} \pi \rho_L N_i r_i^3 \quad (3.24)$$

where K is the number of bins and y_i and N_i are the wetness fraction and number of droplets in the i^{th} bin. The changes of y_i through the nucleation and growth processes are accounted for as

$$\frac{Dy_i}{Dt} = \frac{4}{3} J \pi r_i^3 + 4 \pi r_i^2 \frac{dr_i}{dt} \quad (3.25)$$

in which the first term on the left-hand side (LHS) is the material derivative of y_i , and the first term on the RHS swings into action in case the critical radius is in the size range of the i^{th} bin. The radius of droplets in each bin can be represented by an average size typically mass- or surface-averaged radius. However, for a sufficiently large number of bins, the choice of averaging does not influence the results. In Young's work (Young, 1992), the droplet growth equation was directly integrated, resulting in an implicit analytical equation for the new radius after the growth process. Then, this implicit equation was solved iteratively using the Newton-Raphson method. However, as this equation contains a logarithmic term, it is very sensitive to the initial guess and prone to yield imaginary numbers. Therefore, in Publications II and IV, the droplet growth integration is performed numerically using a third-order Runge–Kutta scheme.

As with Young's work, the growth integration is performed in two steps, a predictor and a corrector step. In the predictor step, the vapour properties are assumed to remain equal to that of the beginning of the integration increment. For the corrector step, the vapour properties are calculated for the mean of the beginning, and updated values at the end of the increment. To estimate the temperature at the end of the increment to be used in the corrector step, a relation between the changes of the mixture specific enthalpy h_m and the pressure is needed. This relation is derived by considering the flow particle as an isolated thermodynamic system

$$\frac{Dh_m}{Dt} = \frac{1}{\rho_m} \frac{Dp}{dt} \quad (3.26)$$

The mixture enthalpy is connected to the enthalpies of liquid and vapour through Equation 3.4. Furthermore, the change in vapour enthalpy is related to the variations in vapour temperature and pressure and it is defined by the following thermodynamic relation:

$$dh_v = c_{p,v} dT_v + \left(\frac{1 - \alpha_v}{\rho_v} \right) dp \quad (3.27)$$

where $c_{p,v}$ is the vapour isobaric specific heat capacity and α_v is the vapour isobaric expansion coefficient. Eventually, by using Equations 3.4, 3.26 and 3.27, the temperature change after each integration time step is estimated as

$$\Delta T_v = \frac{\sum_{i=1}^K (y_i (h_v - h_i)) + \left(\frac{\alpha_v T_v - Y}{\rho_v}\right) \Delta p}{c_{p,v}}. \quad (3.27)$$

To reduce the computational costs, the number of droplet bins can be decreased, or even the entire spectrum can collapse into a single representative size by an averaging method (see e.g. Gerber (2002) and Fakhari (2006)). However, in Publication II, the entire droplet spectrum is restored by introducing one bin at every single integration step in the Lagrangian tracking module. Thus, all of the information on the size distribution of droplets is retained in the calculation, and the results of the E-L model provide reliable benchmark calculations.

3.4 Monodispersed model

The monodispersed model (referred to hereafter as Mono) is the least expensive model in terms of computational expenses compared to the previously presented ones because only two transport equations are required to track the liquid phase evaluation. By the same token, the Mono is the most common model for wet-steam flows applied in numerous works, such as those by Mccallum & Hunt (1999), Gerber and Kermani (2004) and Dykas & Wróblewski (2012), to name a few. In most studies applying the Mono, and also in Publication II, the total liquid droplet number and liquid volume are the ones to be conserved in the calculations. In other words, the Mono can be viewed as a type of the CMOM consisting of only two moments which are connected to each other by an average droplet size, i.e. the volume-averaged radius $r_{30} = (\mu_3/\mu_0)^{1/3}$.

4 Comparison of dispersed multiphase flow models

This chapter concerns comparison of the DMFMs as presented in Publication II. The results of the quadrature method of moments, E-L model and monodispersed model are denoted by QMOM, E-L model and Mono, respectively. Moreover, to be consistent with Publication II, the results of the conventional method of moments are indicated by MOM, that is to say MOM and CMOM are used interchangeably in this chapter.

Before discussing the results, it is remarked that although limited experimental measurements for pressure and mean droplet size are available from the studied test cases, the evaluation of the MOM, QMOM and Mono are based on the E-L model calculations. The reasons for relying on the E-L model calculations instead of measurements for evaluating other DMFMs are:

1. The E-L model is the most accurate model among the applied DMFMs, as it preserves the complete information on the droplet size distribution and it is immune to discretisation errors in the Eulerian framework.
2. There are considerable doubts over the experimental data and also their interpretation methods (which are from several decades ago), in particular for the droplet size measurements.
3. No experimental data are available for other important parameters such as the droplet number and wetness fraction distributions to cross-check the modelling results.
4. The combination of deficiencies in nucleation and droplet growth theories along with inaccuracies of a DMFM may influence the results in favour of or against matching the experiment. Therefore, comparing the DMFMs only based on the experiment can result in misleading conclusions.

4.1 Introduction of test cases

Two test cases are selected for evaluating the DMFMs: Nozzle A of the study by Moore et al. (1973) and the nozzle experiment numbered as 252 (Exp. 252) from the work by Moses and Stein (1978). In Nozzle A, the supplied steam at the inlet was 17 K superheated at a stagnation pressure of 0.25 bar. In the experiment 252, the superheating degree and stagnation pressure were 25.26 K and 0.4005 bar, respectively. For the Moses and Stein nozzle, the effective area is used in calculation, owing to the considerable boundary layer thickness compared to the nozzle height and depth. Figure 4.1 compares the geometries and distribution of supersaturation in these nozzles. It can be seen that different nozzle geometries and inlet boundary conditions resulted in a distinct supersaturation distribution in these two nozzles. For more information on these nozzle experiments see the appendix.

The shape of the converging part of Nozzle A was not given by Moore. However, the shape of the diverging part was provided in the form of a straight line indicating that the geometry curvature was discontinuous at the throat of Nozzle A (and also all other nozzles) in the work by Moore et al. (1973). Thus, in Publication II, the converging part of Nozzle A is approximated by a straight line, as suggested by Kermani & Gerber (2003). In contrast, the Moses and Stein nozzle curvature in both transonic and supersonic sections was a continuous part of a circular arc. The continuous curvature of the Moses and Stein nozzle results in a very smooth and much wider distribution of supersaturation and consequently nucleation zone over the nozzle centreline compared to Nozzle A (see bottom of Figure 4.1).

For the same reason, the hypothetical expansion rates (calculated for the isentropic expansion of a dry flow) of these two nozzles are very dissimilar. In Nozzle A, the expansion rate quickly reaches a peak of around 3500 sec^{-1} in the nucleation zone and then decreases rapidly to a very low rate under 2000 sec^{-1} . Owing to the low expansion rate and superheating degree at the Nozzle A inlet, the nucleation process starts very near to the throat and is restricted to a small proportion of the nozzle. On the other hand, in the Moses and Stein nozzle, the expansion rate in general is quite higher and gradually growing from 10000 sec^{-1} to 13000 sec^{-1} over the nucleation zone. Due to a larger expansion rate and higher superheating degree at the nozzle inlet in Exp. 252, the nucleation zone is moved more downstream of the throat and extends over a larger proportion of the nozzle. Therefore, in Exp. 252 in comparison with Nozzle A, nucleation takes place more gradually over a larger part of the domain until it is enhanced by larger supersaturation levels to quench itself and return to equilibrium.

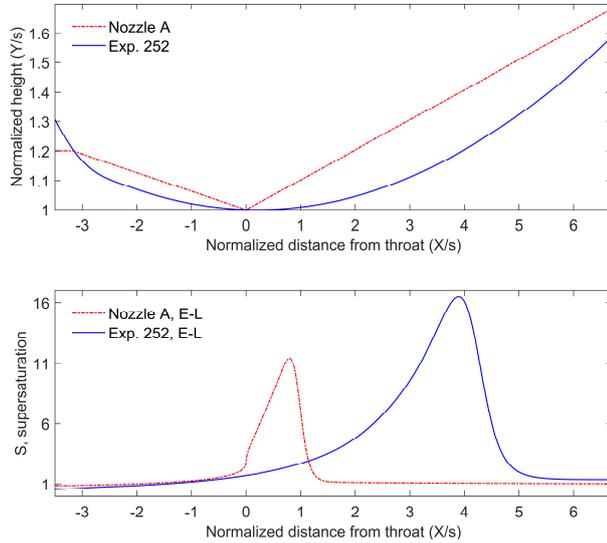


Figure 4.1: Normalised nozzle heights (top) and supersaturation distributions in the presence of phase transition (bottom) obtained by the E-L model; Y and s denote nozzle and throat heights, respectively.

4.2 Grid dependency study

To avoid the nonrealisability problem (this problem is discussed in detail in chapter 5) all transport equations for the MOM, QMOM and Mono are discretised using the first-order upwind scheme, and integration in time is performed by the single-stage explicit scheme. In contrast, as the Lagrangian tracking module is completely decoupled from the Eulerian flow calculations, for the E-L, the third-order MUSCL and Runge-Kutta schemes are applied for the spatial and temporal integration, respectively. The limitation to apply high-order schemes and also the strong grid-dependent nature of the fully Eulerian DMFMs necessitate using very fine grids to obtain grid-independent results. As shown in section 5.5.1 (and Publication III), weights and radii are much more sensitive to the grid resolution than the other variables. Therefore, the grid dependency study is based on the predictions of radii and weights by the QMOM. Figures 4.2 and 4.3 illustrate the distributions of radii and weights in Nozzle A using grids with 1000, 2000 and 3000 elements. It can be seen that for grids with more than 2000 elements, the predictions are not sensitive to the grid size.

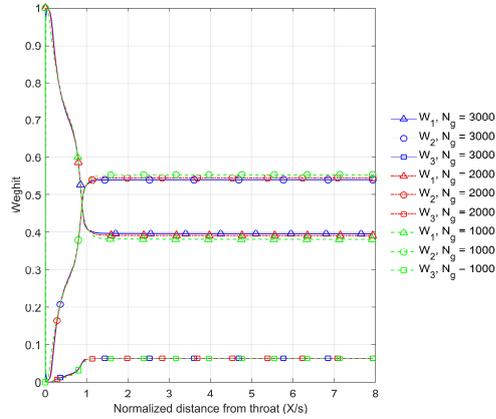


Figure 4.2: Comparison of weights for grid sizes of 1000, 2000 and 3000 in Nozzle A, N_g indicates the grid size.

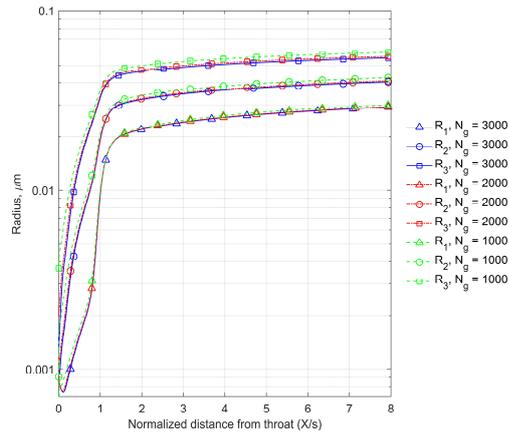


Figure 4.3: Comparison of radii for grid sizes of 1000, 2000 and 3000 in Nozzle A, N_g indicates the grid size.

4.3 Nozzle A

Figures 4.4 and 4.5 show that all polydisperse DMFMs, i.e. the MOM, QMOM and E-L model predict quite similar distributions for the pressure and mean diameter in Nozzle A. On the other hand, the pressure and mean diameter distributions by the Mono are rather different. Given the simplicity of the flow and condensation process, it is concluded that the Mono does not precisely locate the Wilson point and cannot correctly predict the highest nucleation rate in the domain. The slight discrepancies in predictions by the Mono, compared to the polydisperse DMFMs, can become considerable in practical problems with several nucleation processes. It is noted that for flows with $M > 1$, the

Wilson point is identified equivalently as the location of the lowest pressure or highest supersaturation.

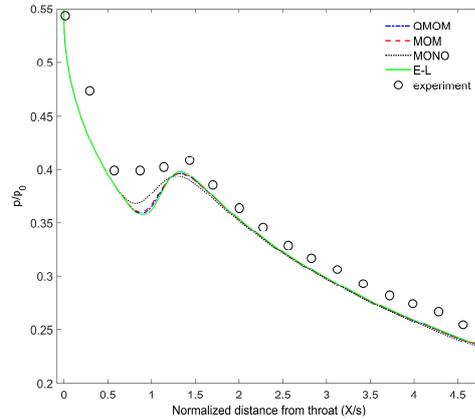


Figure 4.4: Comparison of pressure distributions in Nozzle A.

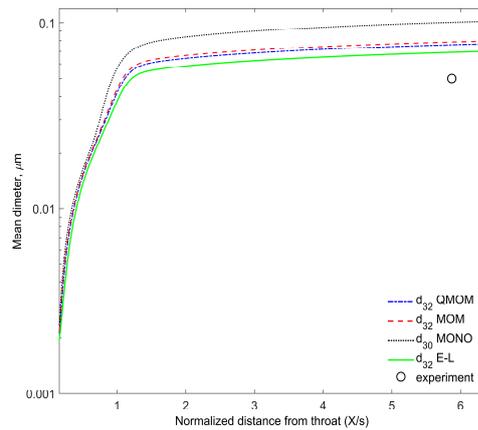


Figure 4.5: Comparison of droplet mean diameter distributions in Nozzle A.

The normalised distribution of moments with respect to the moments given by the E-L model over the nucleation zone are shown in Figure 4.6. It can be seen that the QMOM predicts moments in closer agreement with those of the E-L model, in particular for moments with orders above two. The better accuracy of the QMOM stems from its capability to model the droplet growth using three radii and weights compared to the MOM, which only uses a single averaged radius, i.e. r_{20} . Recalling chapter 3, it should be remarked that μ_4 and μ_5 are not needed in the MOM calculations and do not influence the MOM results at all. Nevertheless, to allow a more informative examination of the

MOM on the droplet size distribution, it is decided to retain and update these in calculations.

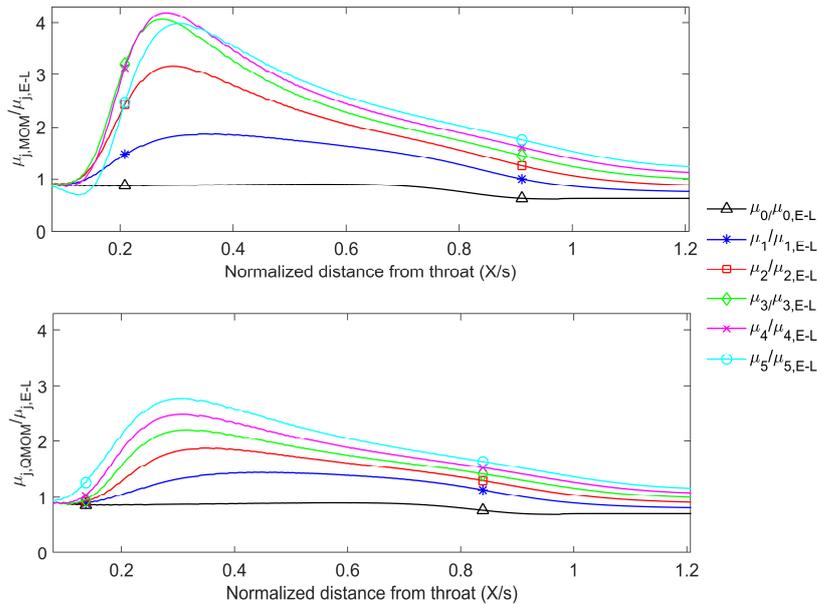


Figure 4.6: Normalised moments, with respect to the E-L model, of MOM (top) and QMOM (bottom) over the nucleation zone in Nozzle A.

In addition, having μ_4 and μ_5 available for the MOM, by applying the Gaussian quadrature one can calculate three radii and weights also for the MOM. Thus, the underlying size distribution can be approximated in a discrete fashion by three radii and weights, as shown in Figure 4.7. As with the moments, the discrepancy between the radii and weights from the MOM and QMOM is also significant in the nucleation zone, as shown in Figure 4.7. Nonetheless, after the quench of nucleation, i.e. $X/s \approx 1.2$, the results of the two models become quite similar. It is stressed that μ_4 and μ_5 do not affect the MOM results and the radii and weights were computed just once in the post-processing stage at the end of calculation of the MOM.

The discrete size distributions obtained by the MOM and QMOM are compared with the full-size spectra resolved by the E-L model at three locations: inside, just after and far downstream of the nucleation zone in Figure 4.8. As with the previous comparisons, here again the predictions by the QMOM are clearly superior to those of the MOM in the nucleation zone ($X/s = 0.3$) and closer to the predictions by the E-L model. Downstream of the nucleation zone, the QMOM and MOM results are relatively alike. At $X/s = 1.5$ and $X/s = 7.0$ where size spectra become broader, the discrete distributions represented

by only three radii fail to establish a perceptible means for comparison. However, it should be emphasised that the above-mentioned failure must not be interpreted as wrong predictions for moments since the relative moments are close to one downstream of $X/s = 1.2$, as shown in Figure 4.6. This failure only indicates that to mimic the full shape of the size distribution clearly, more quadrature points are needed in the QMOM. In general, it is possible to conclude that the QMOM provides slightly closer resemblances to the E-L model also after the nucleation zone in Figure 4.8.

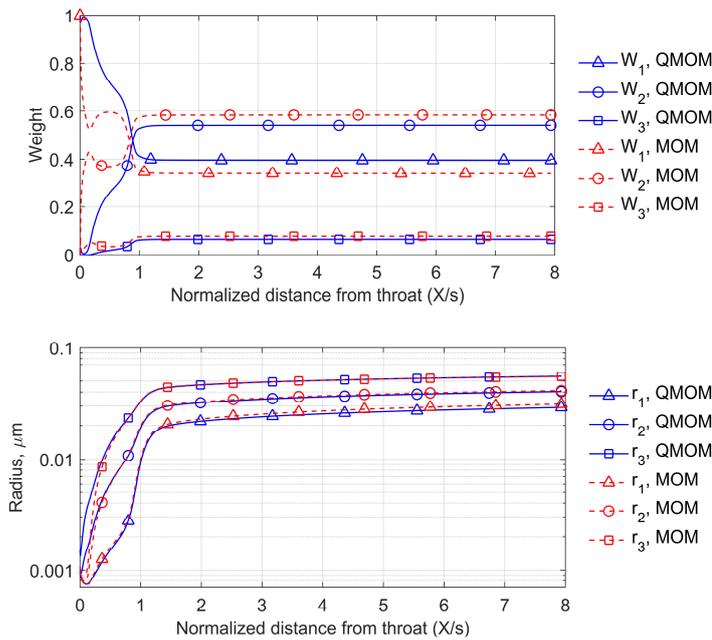


Figure 4.7: Comparisons of weights (top) and radii (bottom) between QMOM and MOM in Nozzle A.

It is interesting to note that downstream the nucleation zone where the size distribution is fully developed, in the absence of a secondary nucleation or evaporation, the size distribution will maintain the same pattern and only drift along the r dimension because of the droplet growth in the PPS, as can be seen in Figures 4.7 and 4.8. After the quench of nucleation when the equilibrium state is re-established, the growth rate becomes almost insensitive to the droplet size, as can be seen also in Figure 4.9. Therefore, the gaps between the radii and weights given by the MOM and QMOM are kept unaffected. In other words, the droplet growth rate computed by Equation 2.12 for slight supersaturation levels can be practically defined by a function only dependent on the vapour properties. Putting aside if this attribute of Equation 2.12 for very low supersaturations is realistic or not, it is argued that in such conditions, the QMOM converts to the MOM. Thus, the important point is that the confinement of the nucleation zone (the region with high

supersaturation) to a small portion of Nozzle A and consequently dominance of the post-nucleation droplet growth in a larger portion of the nozzle leads to relatively same radii and weights given by the QMOM and MOM, even though for the MOM no radii and weights were computed in the course of calculation, and the droplet growth rate was calculated only for r_{20} .

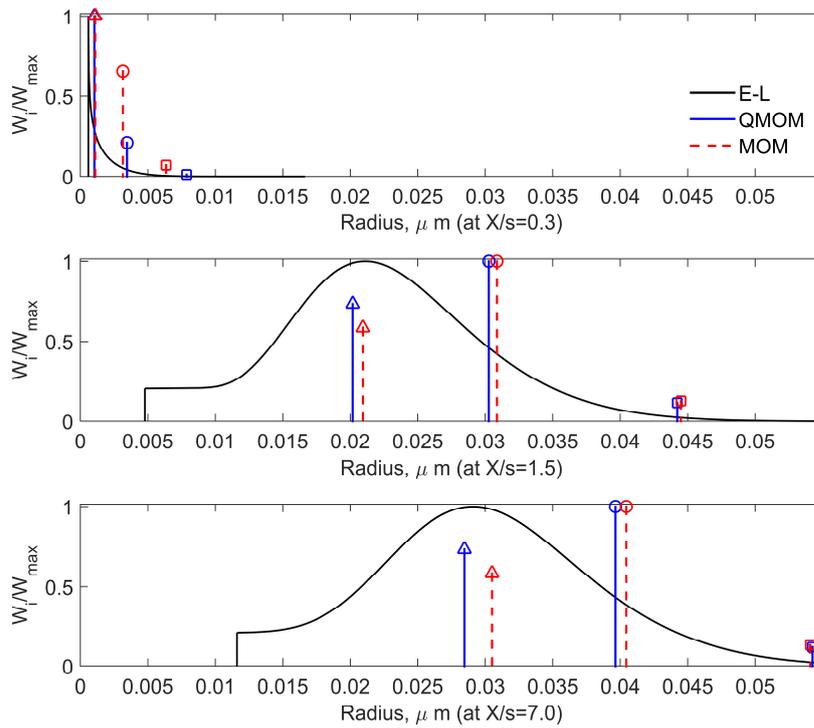


Figure 4.8: Size distributions by QMOM and MOM and E-L model at $X/s = 0.3$ (top), $X/s = 1.5$ (centre) and $X/s = 7.0$ (bottom)

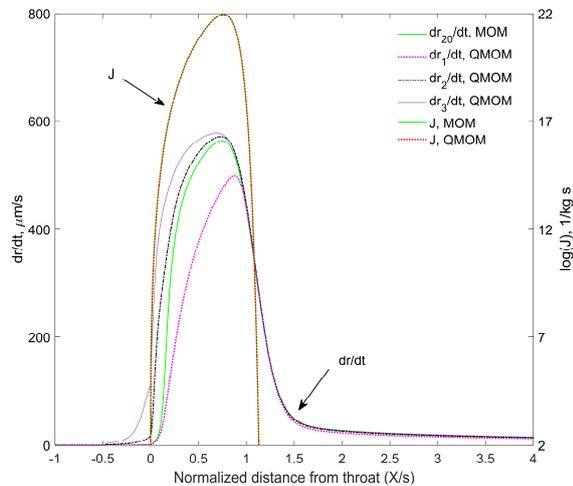


Figure 4.9: Distributions of nucleation rates and growth rates of droplet sizes for QMOM and MOM calculations in Nozzle A.

4.4 Experiment 252

As explained earlier, in Exp. 252 the overall nucleation and non-equilibrium state are more significant and prevail over a larger part of the domain (compare Figure 4.10 with 4.9). As can be seen in Figure 4.10, the deviations between the growth rates are larger and extended to a much greater part of the domain in comparison with Nozzle A. By the same token, as shown in Figure 4.11, the moments predicted by the MOM and QMOM deviate from those of the E-L model to a greater extent and over a wider part of the domain corresponding to the nucleation zone. Nevertheless, compared to the MOM, the QMOM clearly provides better agreement with the E-L model. Similarly, Figure 4.12 also shows more apparent differences between the weights calculated for the QMOM and MOM. Contrary to Nozzle A, even in the post-nucleation part of the domain the weights given by the MOM and QMOM are clearly dissimilar. The wiggles in the weights of both the MOM and QMOM, from the throat to $X/s \approx 1$, are caused by instabilities related to the moment-inversion problem. The moment-inversion problem for nearly monodispersed cases is susceptible to become ill-conditioned if the radii (the quadrature points) are in close proximity to one another, see the radii distributions, from the throat to $X/s \approx 1$, in Figure 4.12 (bottom).

In general, as with Nozzle A, in Exp. 252 also all of the polydisperse models give similar pressure and mean diameter distributions (see Figures 4.13 and 4.14). Nevertheless, it can be concluded that dissimilarities between the moment-based models and the E-L model and also between the MOM and the QMOM themselves, especially considering the pressure distributions, are more apparent in comparison with Nozzle A. It is also

noticeable that the deviation between the Mono and the polydisperse models is more significant compared to Nozzle A.

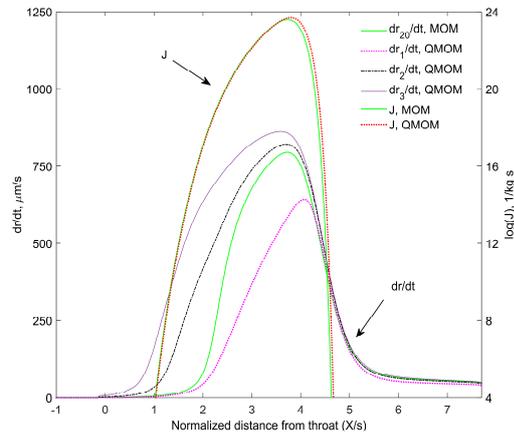


Figure 4.10: Nucleation rate and growth rate distributions for droplet sizes present in QMOM and MOM calculations in experiment 252.

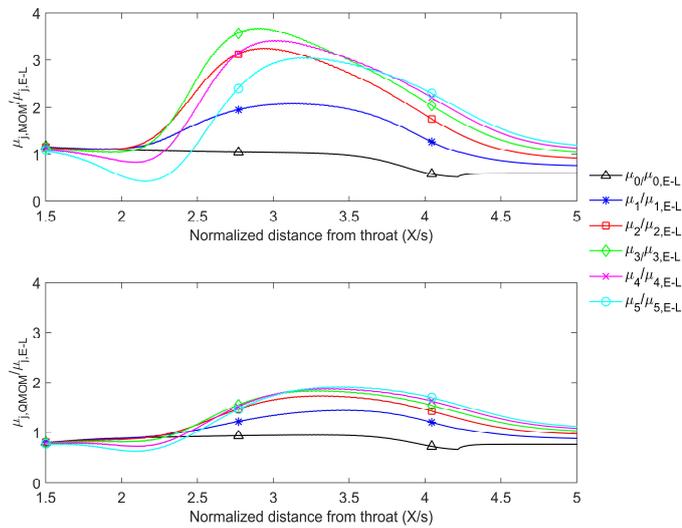


Figure 4.11: Distributions of normalised moments, with respect to the E-L model, of MOM (top) and QMOM (bottom) over the nucleation zone in experiment 252.

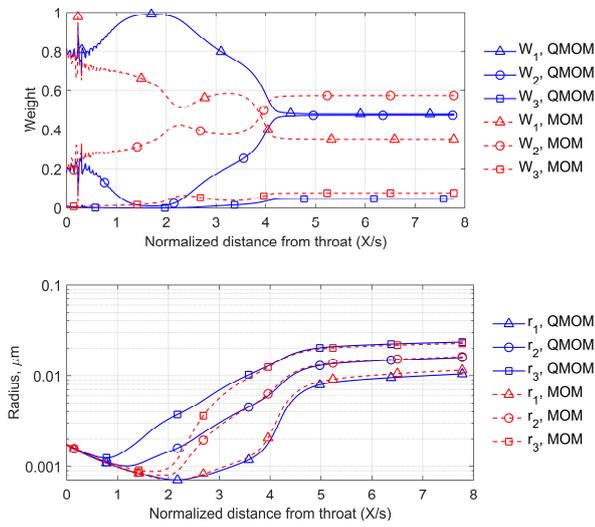


Figure 4.12: Distributions of weights (top) and radii (bottom) from QMOM and MOM in experiment 252.

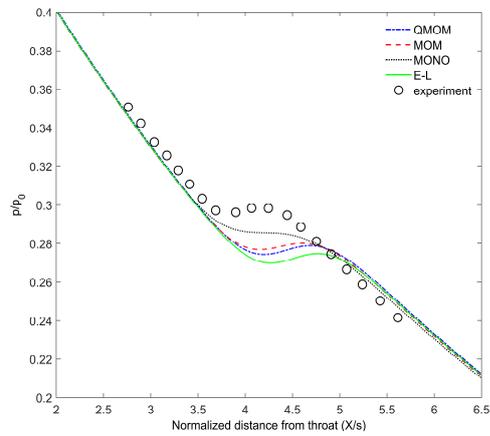


Figure 4.13: Comparison of pressure distributions in experiment 252.

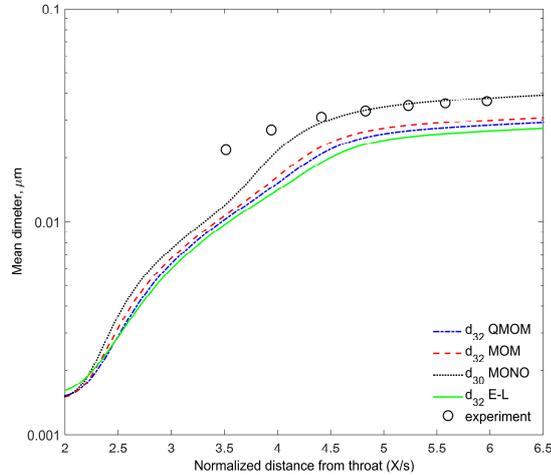


Figure 4.14: Comparison of droplet mean diameter distributions in experiment 252.

4.5 Stability and computational cost of studied DMFMs

Among the studied models, the E-L differs considerably in terms of its structures and objectives from the other ones, which are intrinsically similar. The Lagrangian module which tracks the liquid phase is completely decoupled from the motion solution. Therefore, by employing a third-order explicit Runge–Kutta scheme, the temporal integration in the E-L model can be stabilised and also accelerated using more than one Courant–Friedrichs–Lewy (CFL) number. Comparatively speaking, the results of the E-L model are not sensitive to the grid size. In addition, as the E-L model is not burdened by the nonrealisability problem, it is fully compatible with high-order spatial schemes, reducing its dependency on the grid resolution even further. However, for complex two- and three-dimensional flows, the E-L model quickly becomes inefficient and intractable. The author is not aware of any work reported in the literature that applies the E-L model for simulating unsteady flows in multistage full-scale turbines. Due to the above-mentioned distinct features of the E-L model, a meaningful comparison about its stability and computational costs with other DMFMs make is difficult to draw.

On the other hand, the structures of the MOM, QMOM and Mono are quite similar. Thus, a fair comparison between these models can be made about the central processing unit (CPU) time and stability. The CPU times of the MOM and QMOM are normalised with respect to that of the Mono and presented in Table 4.1. Based on Table 4.1 and the fact that the pressure and mean droplet size distributions calculated by the MOM are very close to those of the QMOM and also the E-L model, it can be argued that the MOM is the most efficient model. Nevertheless, as discussed before, the MOM may lose its accuracy for flows undergoing several nucleation processes. According to Table 4.1, the

QMOM consumes the largest amount of CPU time for which the moment-inversion algorithm alone is responsible for a significant proportion of consumed CPU time.

Table 4.1: CPU time for 100 time steps of QMOM and MOM normalised with respect to Mono

Grid size	MOM	QMOM	Share of Wheeler algorithm in QMOM %
3000	1.08	1.98	20%
1000	1.09	1.78	16%

Based on the number of quadrature points, the QMOM needs information about moments with orders higher than three. For wet-steam flows, high-order moments such as μ_4 and μ_5 here take extremely small values. Thus, it is better (or sometimes necessary) to perform moment calculations, particularly in the moment-inversion algorithm, with double-precision. In all Publications, the calculations for all models are done using the double-precision format.

As mentioned for Exp. 252 under Figure 4.12 (bottom), an issue can occur in the QMOM for nearly monodispersed distributions because the moment-inversion problem becomes ill-conditioned for very narrow distribution. This issue typically takes place near the nucleation front in flows with a uniform expansion rate, as in this flow type superstation rises very smoothly to begin the nucleation (see bottom of Figure 4.1). In such cases during the initial stages of the nucleation process, the droplet size distribution has nearly a zero standard deviation and a mean almost equal to the local critical droplet size. This problem can be avoided by nucleating droplets of a size distribution with an appropriate standard deviation and a mean equal to the local critical radius.

5 Moment corruption and nonrealisability problem

This chapter (in sections 5.1 and 5.2) encompasses the theory parts of Publications III and IV on moment corruption and the nonrealisability problem. It also (in sections 5.3 and 5.4) examines the solution techniques to the nonrealisability problem for the QMOM presented in Publication III.

5.1 Properties of moment space and realisability condition

The members of a moment set are not independent individuals; instead, they are directly interrelated to one another and can be only defined in a set. In fact, the moments in a set form a so-called moment space which possesses certain properties. Apart from the positivity of all moments, as shown by Feller (1971), a necessary condition for the realisability of a moment set is the convexity of the moment space which is determined by

$$d_{2j} = \mu_{j-2}\mu_j - \mu_{j-1}^2 \geq 0. \quad (5.1)$$

However, the convexity condition is sufficient only for moment sets with up to four members, as $d_{22} = \mu_0\mu_2 - \mu_1^2 \geq 0$ and $d_{23} = \mu_1\mu_3 - \mu_2^2 \geq 0$. It is noteworthy that $d_{22} \geq 0$ checks the non-negativity of the distribution variance. The necessary and sufficient condition for realisability is laid down by Hankel–Hadamard determinants, encapsulating also the convexity condition of the moment space (Shohat & Tamarkin, 1943). For a given moment set to be realisable, all Hankel–Hadamard determinants must be positive as shown below

$$\Delta_{m,l} = \begin{vmatrix} \mu_m & \mu_{m+1} & \cdots & \mu_{m+l} \\ \mu_{m+1} & \mu_{m+2} & \cdots & \mu_{m+l+1} \\ \vdots & \vdots & \ddots & \vdots \\ \mu_{m+l} & \mu_{m+l+1} & \cdots & \mu_{m+2l} \end{vmatrix} \geq 0 \quad (5.2)$$

in which $m = 0, 1$ and $l \geq 0$. The realisability condition, as shown above, becomes progressively complex and difficult to ascertain by increasing the number of moments in a set. As an example for the moment set with six members, $q = [\mu_0 \dots \mu_5]$, the realisability condition requires:

1. $\mu_{0-5} \geq 0$.
2. $\Delta_{0,1} = d_{22} \geq 0$ & $\Delta_{1,1} = d_{23} \geq 0$.
3. $\Delta_{0,2} = \begin{vmatrix} \mu_0 & \mu_1 & \mu_2 \\ \mu_1 & \mu_2 & \mu_3 \\ \mu_2 & \mu_3 & \mu_4 \end{vmatrix} \geq 0$ & $\Delta_{1,2} = \begin{vmatrix} \mu_1 & \mu_2 & \mu_3 \\ \mu_2 & \mu_3 & \mu_4 \\ \mu_3 & \mu_4 & \mu_5 \end{vmatrix} \geq 0$.

For a given realisable moment set containing a finite number of members, in theory, an infinite number of different NDFs can be found. The only criterion for any found NDF is that it must be non-negative over the positive section of the r coordinate in the PPS, i.e.

for $r > 0$. However, for a nonrealisable moment set it is impossible to find any NDF that is entirely non-negative for $r > 0$. Strictly speaking, the elements of a nonrealisable set cannot be called moments because for a nonrealisable set no f can be realised that $r \in \mathbb{R}_{>0}: f(r) \geq 0$.

5.2 Moment corruption

As explained by Wright (2007), any process which results in the mixing of moments without taking account of the moment interrelations in a set may produce nonrealisable moment sets. High-order spatial and temporal schemes, flux limiters, artificial diffusion terms and in general any numerical process which treats moments separately regardless of their interrelations may corrupt the moment interrelations and produce nonrealisable sets.

Among numerous numerical processes which are prone to cause nonrealisability in the context of the finite volume method, the main attention is devoted to high-order advection schemes due to their central importance. It should be noted that the term related to droplet growth has no effect on moment corruption, because if a moment set in a computational cell is realisable at time t , the growth of droplets just drifts (or disperses) the NDF over the r coordinate in the PPS. Hence, after the growth process, the new moments at time $t + \Delta t$ still remain realisable. Furthermore, nucleation itself does not create nonrealisability because it only generates realisable moments of a monodispersed droplet population with a size equal to the local critical radius. Therefore, if the initial moment set in the cell is realisable, the addition of new moments to them due to nucleation will not corrupt the final moments. However, the nucleation of monodispersed droplets at the beginning of the nucleation zone, i.e. the nucleation front, and the sharp gradients introduced by nucleation to moments seriously give rise to the nonrealisability problem indirectly. The indirect influence of nucleation on nonrealisability is further discussed for the test cases in this chapter. Thus, by omitting the nucleation and droplet growth terms in the population balance equation of liquid droplets, i.e. Equation 3.14, it can be discerned how only the first-order advection scheme is able to guarantee the non-negativity of f (Desjardins, et al., 2008). Applying a single-stage explicit time integration scheme, the discretised form of Equation 3.14, reads

$$f_I^{t+\Delta t} = f_I^t + \zeta(F_{I-1/2}^t - F_{I+1/2}^t) \quad (5.3)$$

where $\zeta = \Delta t / (A_I \Delta X_I)$ and F is the flux of f . Recalling Equation 3.11, for the flux of NDF one can write

$$F_{I+1/2} = \frac{1}{2}(U_L^+ f_L + U_R^- f_R), \quad (5.4)$$

to expand Equation 5.3 as follows:

$$\begin{aligned}
f_I^{t+\Delta t} = & f_I^t + \frac{\zeta}{2} (A_{I-1/2} U_{I-1/2}^{L+} f_{L,I-1/2})^t - \\
& \frac{\zeta}{2} (A_{I+1/2} U_{I+1/2}^{R-} f_{R,I+1/2})^t + \frac{\zeta}{2} (A_{I-1/2} U_{I-1/2}^{R-} f_{R,I-1/2})^t - \\
& \frac{\zeta}{2} (A_{I+1/2} U_{I+1/2}^{L+} f_{L,I+1/2})^t.
\end{aligned} \quad (5.5)$$

The main goal here is to seek the condition under which nonrealisability is avoided, i.e. the condition that guarantees $f_I^{t+\Delta t}$ is non-negative if f_I^t was non-negative. In this respect, it is remarked that apart from f_I^t , the second and third terms on the RHS of Equation 5.5 are also non-negative based on Equations 3.9 and 3.10. However, the sign of $f_I^{t+\Delta t}$ cannot be determined yet because the last two terms on RHS of Equation 5.5 are non-positive.

However, as described by Desjardins et al. (2008), only for the first-order advection scheme a criterion can be found that ensures the non-negativity of $f_I^{t+\Delta t}$. Using the first-order scheme leads to the approximation below for the left and right states of f

$$f_{R,I-1/2} = f_{L,I+1/2} = f_I. \quad (5.6)$$

Incorporating the relations above into Equation 5.5, this equation is rewritten as

$$\begin{aligned}
f_I^{t+\Delta t} = & f_I^t \left(1 + \frac{\zeta}{2} (A_{I-1/2} U_{R,I+1/2}^-)^t - \frac{\zeta}{2} (A_{I+1/2} U_{L,I+1/2}^+)^t \right) \\
& + \text{non-negative terms.}
\end{aligned} \quad (5.7)$$

Therefore, the non-negativity of f is ensured if

$$\begin{aligned}
1 + \frac{\zeta}{2} (A_{I-1/2} U_{R,I+1/2}^-)^t - \frac{\zeta}{2} (A_{I+1/2} U_{L,I+1/2}^+)^t & \geq 0 \xrightarrow{\zeta = \frac{\Delta t}{A_I \Delta X_I}} \\
\Delta t \leq \frac{2A_I \Delta X_I}{(A_{I+1/2} U_{L,I+1/2}^+)^t - (A_{I-1/2} U_{R,I+1/2}^-)^t} & \quad (5.8)
\end{aligned}$$

By satisfying the criterion above for the time step in each integration step and all cells, the NDF can be kept non-negative, or equivalently, the realisability of moments can be preserved.

On the other hand, owing to the complex mixing of variables from different cells in high-order advection schemes such as MUSCL or QUICK, it is impossible to ensure the non-negativity of the NDF in the course of time integration. By the same token, using an ordinary high-order time integration scheme, such as Runge-Kutta, increases the number of terms with a negative sign in Equation 5.5, and therefore, realisability cannot be guaranteed during time advancement. Vikas et al. (2011) suggested utilising the second-order strong stability-preserving Runge-Kutta scheme, which allows to enhance the temporal integration accuracy and also maintains realisability.

As an example, the second-order MUSCL is employed to further elucidate how a high-order scheme can produce a negative NDF or equivalently nonrealisable moments. Let us consider applying the second-order MUSCL in a simplified one-dimensional example as shown Figure 5.1. All the moment set at the cell centres are realisable. For simplicity, only the three first moments are considered in this example. Knowing the flow direction, by using the second-order MUSCL ($k = 0$) in Equation 3.12, μ_j at the west face of the cell I is interpolated as

$$\mu_{j_{I-1/2}} = \mu_{j_{I-1}} + \frac{1}{4}\mu_{j_I} - \frac{1}{4}\mu_{j_{I-2}}. \quad (5.9)$$

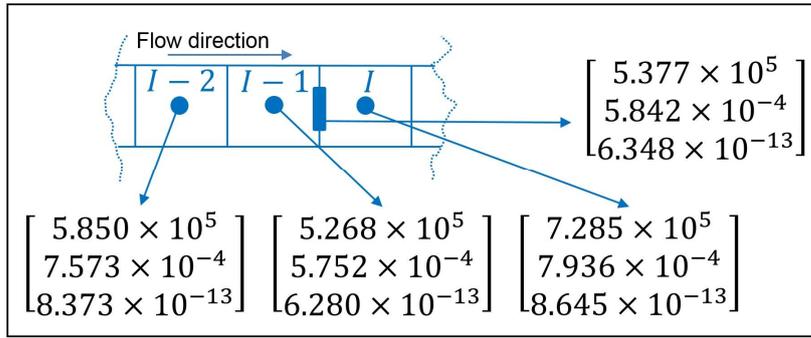


Figure 5.1: Interpolation of moments at the face $I - 1/2$ by the second-order MUSCL.

The interpolated moments at the face $I - 1/2$ are shown in Figure 5.1. At first glance, nothing seems to be wrong with the interpolated moments, as all of them are positive and apparently reasonable. However, by calculating $d_{22} = \mu_0\mu_2 - \mu_1^2 = -3.12 \times 10^{-12} < 0$, it is discerned that these three moments correspond to a negative variance and no NDF can be realised for them. Now let us reconsider this example in terms of NDFs instead of moment sets. Since in addition to the zeroth moments two other moments are also known, the moment sets can be represented by an equivalent log-normal distribution function in the cells, as shown in Figure 5.2. The calculation of log-normal distribution functions from moments will be discussed in section 5.3.2. In the same fashion as Equation 5.9, f at the west face of cell I is given as

$$f_{I-1/2} = f_{I-1} + \frac{1}{4}f_I - \frac{1}{4}f_{I-2}. \quad (5.10)$$

It can be seen in Figure 5.2 that the interpolated NDF is not entirely positive and becomes negative in a region of the r coordinate around the neighbourhood of the peak of distribution in the cell $I - 2$. In fact, the example shows when there are sharp gradients in size distributions (or moment sets) in adjacent cells, using a high-order interpolation scheme results in negative NDFs.

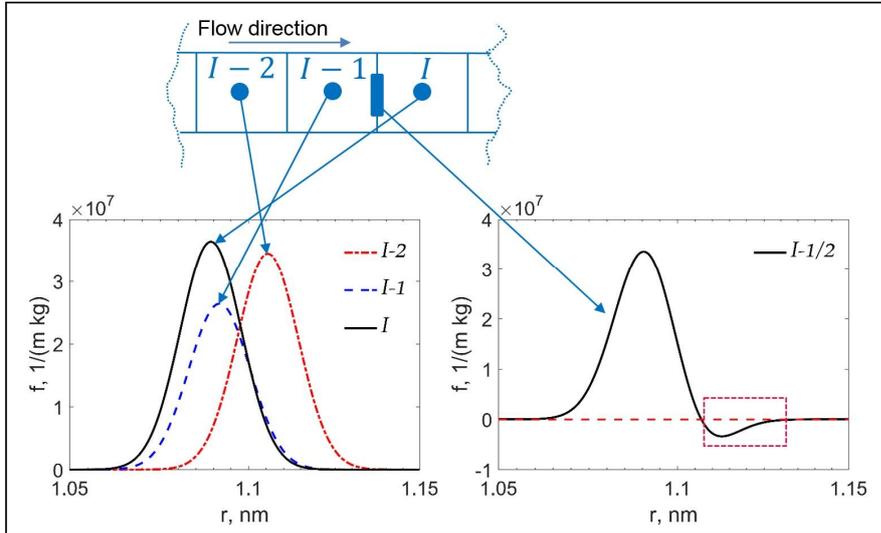


Figure 5.2: Interpolation of NDF at the face $I - 1/2$ by the second-order MUSCL.

It is noteworthy that nonrealisability occurs also in solving Euler equations for extreme low-density and low-pressure cases such as astrophysical jets with enormous Mach numbers, spotted by the Hubble Space Telescope, and blast waves (Li, et al., 2006; Zhang & Shu, 2010). As with the moment space, also in Euler equations the set consisting of density, momentum, total internal energy and pressure must be convex to be realisable. The breach of convexity in the above-mentioned cases leads to negative densities and pressures in numerical solutions to Euler equations.

5.3 Solution techniques for nonrealisability problem

In the literature, the nonrealisability problem is mainly addressed from the QMOM standpoint. This is because the application of the QMOM is precluded by nonrealisability while the CMOM, at least seemingly, is not troubled by this problem.

As explained earlier, the realisability of moment sets can be ensured only if the first-order advection scheme is applied. However, the first-order scheme is notorious for excessive numerical diffusion and should be avoided especially for flows in steam turbines with complex features and strong gradients. Hence, the main aim of a solution to nonrealisability is to allow the application of high-order advection schemes along with the QMOM without any concerns over moment corruption. In this section, two main types of solutions to the nonrealisability problem in the framework of the QMOM are introduced and compared in Nozzle B as a test case.

5.3.1 First solution type; realisable high-order schemes

The first type of solutions considers designing special high-order advection schemes to preserve the moment space in numerical calculations. For instance, Kah et al. (2012) devised a realisable second-order scheme both in time and space by transforming the moment space into a less complex one, i.e. the canonical moment space, to conveniently preserve the positivity of Hankel–Hadamard determinants. Another specially designed scheme was devised by Vikas et al. (2011). They suggested that, instead of moments, the corresponding weights and radii can be interpolated at the cell faces. Then, the moments at the cell faces are calculated from the interpolated weights and radii. Vikas et al. showed that if the first-order scheme is applied to interpolating the radii, it is possible to utilise any high-order scheme for the interpolation of weights while keeping the NDF positive. According to the first-order approximation, one can write $r_{i,L,I} = r_{i,L,I+1/2} = r_{i,R,I-1/2}$. Then, the non-negativity of $f_I^{t+\Delta t}$ is ensured if the sum of non-positive terms and f_I^t in Equation 5.7 also remains non-negative, so

$$\sum_i^n \left[w_{i,I} + \frac{\zeta}{2} (U_{R,I-\frac{1}{2}}^- w_{i,R,I-\frac{1}{2}} - U_{L,I+\frac{1}{2}}^+ w_{i,L,I+\frac{1}{2}}) \right] \delta(r - r_i)_I \geq 0 \quad (5.11)$$

$$\xrightarrow{\zeta = \frac{\Delta t}{A_I \Delta X_I}} \Delta t \leq \frac{2w_{i,I} A_I \Delta X_I}{(U_{R,I-1/2}^- w_{i,R,I-1/2} - U_{L,I+1/2}^+ w_{i,L,I+1/2})}$$

The condition above must be satisfied at each time step and for all cells to guarantee the realisability of moment sets. It should be emphasised that the schemes devised using this approach are not exactly equivalent to the conventional high-order schemes because although weights can be interpolated by arbitrary high spatial accuracy, the accuracy for radii interpolation is limited to the first order. Hence, this scheme is termed as the quasi-high-order scheme.

5.3.2 Second solution type; moment corrections

The second solution type concerns moment correction techniques which directly act on nonrealisable moment sets irrespective of the advection scheme. As a result, the moment corrections are advantageous if the advection scheme cannot be changed. However, the flexibility over the advection scheme offered by moment corrections comes at the expense of modifying the moment sets which may significantly change the underlying size distribution. Two moment corrections developed by McGraw (2006) and Wright (2007) are briefly explained here, and their performance is compared against the quasi-high-order scheme in the next chapter.

The correction technique given by McGraw is based on recovering the convexity condition which is a necessary but not sufficient condition for realisability. In this technique, first $d_{2j} \geq 0$ are checked for all moment sets in the domain. Thereafter, if any set does not satisfy $d_{2j} \geq 0$ it is corrected to recover the convexity. If more than one

moment needs to be modified, the corrected moment set may considerably deviate from the original set, as shown by Marchisio and Fox (2013).

The technique proposed by Wright substitutes a new realisable set for an old nonrealisable one. This technique calculates the new moment set from a log-normal distribution or the arithmetic average of two log-normal distributions. For the latter, as described by Marchisio and Fox (2013) μ_1 and μ_3 are typically selected to calculate the parameters of the first log-normal distribution. For the second log-normal distribution, μ_2 and μ_3 are used to compute the distribution parameters. Thus, the μ_0 and μ_3 of the new moment set will have values equal to the old μ_0 and μ_3 . The new moments from the first log-normal distribution are given as

$$\mu_j = \mu_0 \exp\left(jz + \frac{j^2 v}{2}\right) \quad (5.12)$$

where z and v are related to the mean and variance of the log-normal distribution and calculated as

$$z = \frac{3}{1 \times 3 - 1^2} \ln\left(\frac{\mu_1}{\mu_0}\right) + \frac{1}{1 \times 3 - 3^2} \ln\left(\frac{\mu_3}{\mu_0}\right) \quad (5.13)$$

$$v = \frac{1}{1-1/3} \left[\frac{2}{3^2} \ln\left(\frac{\mu_3}{\mu_0}\right) - \frac{2}{1 \times 3} \ln\left(\frac{\mu_1}{\mu_0}\right) \right]. \quad (5.14)$$

For the second log-normal distribution, z and v are calculated by simply replacing 1 and 3 with 2 and 3, respectively.

5.4 Comparison of solutions to nonrealisability

To compare the moment corrections and the realisable quasi-high-order scheme, Nozzle B of Moore's experiments is considered as the test case. The details on the boundary conditions and geometry of Nozzle B are presented in the appendix.

5.4.1 Realisable quasi-high-order scheme

To form the quasi-high-order scheme, the second-order MUSCL is applied, i.e. $k = 0$ in Equations 3.12 and 3.13, for the interpolation of all variables except for radii. To preserve the realisability, radii are interpolated with the first-order upwind approximation.

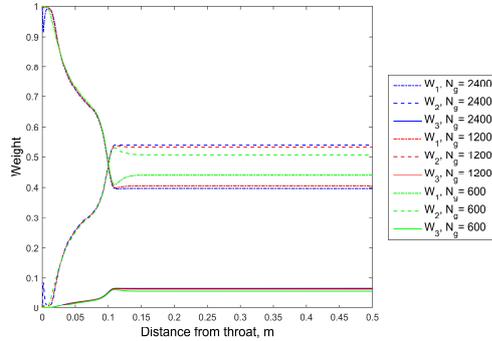


Figure 5.3: Comparison of weights along the nozzle centreline employing different grid sizes; N_g denotes the grid size.

Figures 5.3 and 5.4 compare the weight and radius distributions, respectively, using grids with 600, 1200 and 2400 cells. It can be seen that for the grids with 1200 and 2400 cells the distributions of weights and radii are very similar. The calculated weights are sensitive to the grid size after $X = 0.1$, i.e. downstream of the nucleation zone. In contrast, the radius distributions exhibit a stronger dependency on the grid size in the nucleation zone $0 < x < 0.1$. These different domains of sensitivity to the grid size exist because in the zone of nucleation, the size distribution in each cell is practically a delta function. Thus, the disparities in weight predictions are essentially very small. However, using coarse grids, the initial radii in the nucleation zone cannot be precisely stored in calculations. Then, this inaccuracy in the prediction of initial droplet sizes influences the growth rates of the droplets downstream of the nucleation zone, which appears in form of disparities in the prediction of weights.

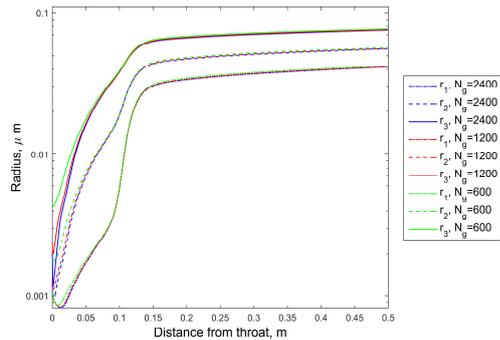


Figure 5.4: Comparison of radii along the nozzle centreline employing different grid sizes; N_g denotes the grid size.

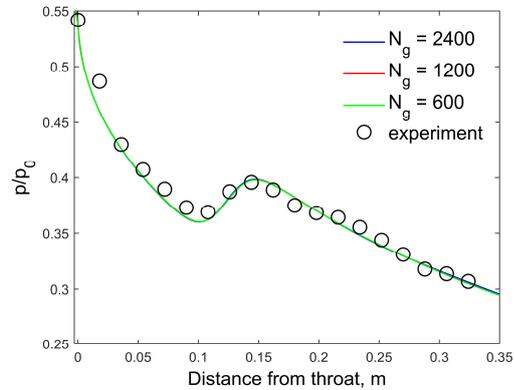


Figure 5.5: Comparison of pressures along the nozzle centreline employing different grid sizes; N_g denotes the grid size.

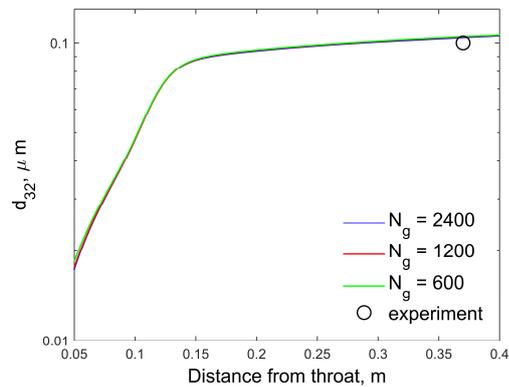


Figure 5.6: Comparison of d_{32} along the nozzle centreline employing different grid sizes; N_g denotes the grid size.

On the other hand, the pressure and the Sauter mean diameter d_{32} are insensitive to the grid resolutions (see Figures 5.5 and 5.6). In general, the quasi-second-order scheme is successful in preserving the realisability. In addition, the predictions of size distribution parameters, i.e. radii and weights, are sensitive to grid size, which is a common feature of DMFMs applied in an Eulerian reference frame.

5.4.2 Moment corrections

McGraw's moment correction fails to deal with the nonrealisability problem in Nozzle B. For both the second- and third-order MUSCL, this correction technique is completely unsuccessful in detecting most of the nonrealisable moment sets. This is because the detection and correction of corrupted moments in McGraw's method are performed only

according to the convexity condition, which for a three-point quadrature is a necessary but insufficient condition for realisability. The radii and weights given by this correction technique take unreadable or even negative values (missing parts of the curves) as shown in Figure 5.7. The unphysical weights and radii, resulting from McGraw's correction, eventually make the solution diverge.

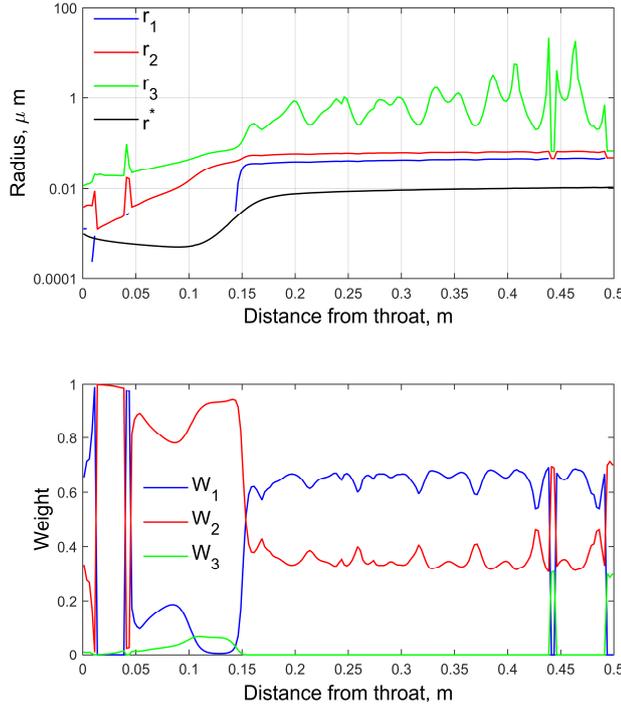


Figure 5.7: Radii and critical radius distributions of (top), and distributions of weights (bottom) from McGraw's moment correction.

On the one hand, the correction technique proposed by Wright is successful in providing acceptable weights and radii. Nevertheless, as this technique replaces all moment sets with those calculated from the average of two log-normal distributions, the final radii and weights are different from the original ones. Figure 5.8 compares the radii from the realisable quasi-second-order scheme and Wright's correction in the nucleation zone. It can be seen that the radii after correction have lost their relations to the local critical size. On the other hand, for the realisable quasi-second-order scheme, the origins and connections to the local critical size for all radii are clear. The weight distributions given by Wright's correction also differ considerably from those of the realisable advection scheme as shown in Figure 5.9. However, pressures and d_{32} are almost identical by both Wright's correction and the realisable scheme (see Figure 5.10).

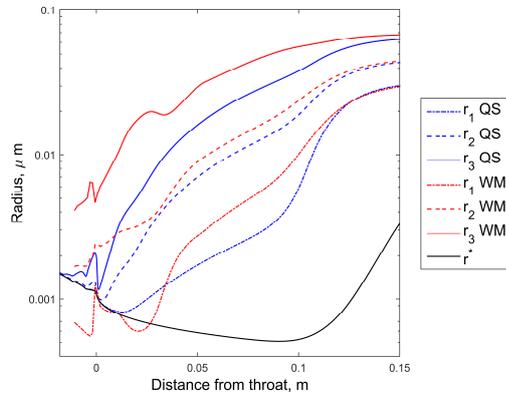


Figure 5.8: Comparison of distributions of radii in the nucleation zone, from the realisable quasi-second-order scheme, indicated by QS, and Wright’s moment correction, indicated by WM.

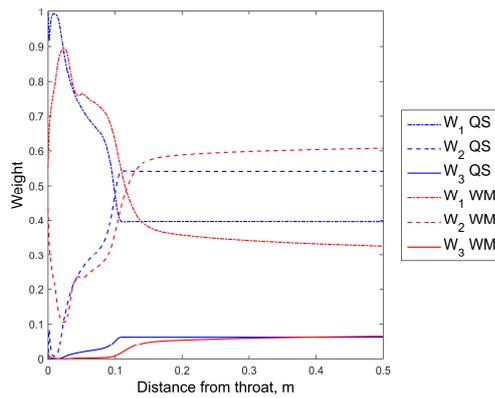


Figure 5.9: Comparison of distributions of weights, from the realisable quasi-second-order scheme, indicated by QS, and Wright’s moment correction, indicated by WM.

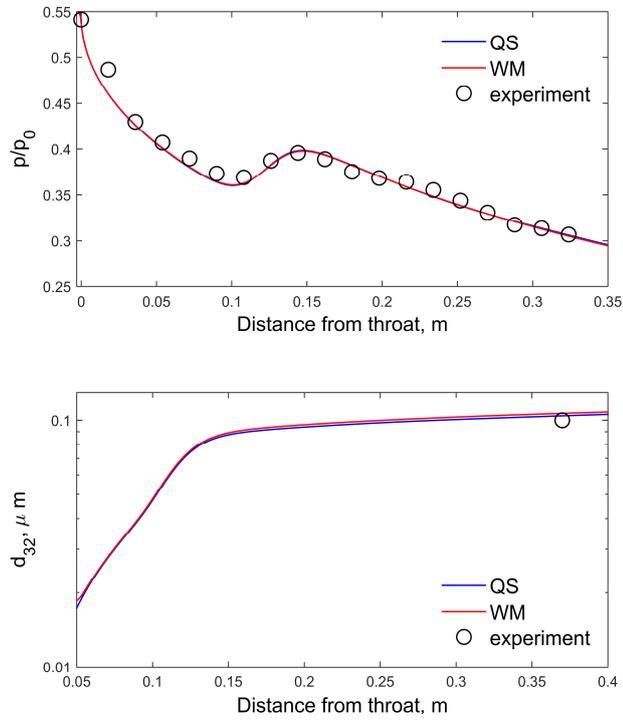


Figure 5.10: Comparison of pressure (top) and d_{32} (bottom) distributions along the nozzle centreline, from the realisable quasi-second-order scheme, indicated by QS, and Wright's moment correction, indicated by WM.

6 Nonrealisability problem with CMOM

This chapter comprises the results and discussions presented in Publication IV examining the effects of the nonrealisability problem on the CMOM results.

Contrary to the QMOM, at first look, it seems that the CMOM is not burdened by the nonrealisability problem. Thus, any high-order advection scheme can be coupled with the CMOM without concern. The reason is that the CMOM provides closure to the moment-transport equations without any recourse to the NDF by using the moments themselves. Therefore, existence of a NDF never arises as a question in the CMOM. Since obtaining a solution using the CMOM is not blocked by the nonrealisability problem, to the knowledge of the current author, this problem with CMOM has not been investigated so far. Therefore, all of the solutions to the nonrealisability problem available in the literature have been proposed in the framework of the QMOM. However, this does not mean that the corruption of moments cannot happen in the CMOM. This chapter shows that as with the QMOM, the application of high-order schemes in the CMOM also leads to a nonrealisable moment set.

Unfortunately, the significance of the nonrealisability problem and its influence on the MOM cannot be determined a priori and can differ case to case. Therefore, three types of test cases with distinct characteristics are considered to examine the effects of moment corruption on the CMOM prediction. The first type deals with steady subcritical condensation nozzles, as in Nozzle B and Exp. 203. The condensation process in these two well-known nozzles is very simple, as it is triggered by only a single nucleation event. The second type concerns steady condensation in a so-called ‘double nozzle’ which consists of two nozzles connected by a duct with a constant cross-sectional area. The flow in double nozzle can be viewed as an idealization of flow in a single stage of a steam turbine in which a secondary nucleation is also present. In fact, the three parts of the double nozzle are analogous to the stator, rotor and the gap between them. The third type considers a mode of unsteady supercritical condensation in Nozzle B to examine how temporal and spatial gradients affect the corruption of moments.

For the steady cases, a benchmark calculation is obtained by solving the moment-transport equations in a Lagrangian reference frame while the other transport equations are solved in an Eulerian frame of reference. The results of this benchmark calculation are denoted by E-L, which should not be confused by the discrete-spectrum Eulerian-Lagrangian model using the same abbreviation. On the other hand, when all the transport equations are solved using an Eulerian reference frame, the corresponding results are denoted by E-E. The aim is to check if the E-E results differ considerably if the third-order MUSCL is employed compared to the benchmark calculations. For the unsteady flow case, the last test case with supercritical condensation, the Lagrangian tracking approach cannot be used due to the nature of this model. Therefore, the evaluation is based on the E-E results using the first-order scheme.

6.1 Subcritical condensation with a single nucleation process

For Exp. 203, the inlet stagnation pressure and superheating degree were set to 0.358 bar and 21.95 K, respectively, while for Nozzle B, these parameters were 0.25 bar and 20 K. The normalised geometries of two nozzles with respect to their throat heights and the supersaturation distributions in these nozzles are compared in Figure 6.1. As in chapter 4, here

also the effective area is used for the nozzle of Moses and Stein. Moreover, for Nozzle B the shape of converging section is retrieved based on the isentropic expansion of steam in this section and using the distribution of pressure given by Moore, et al. (1973). See the appendix for more information on these nozzle geometries and boundary conditions.

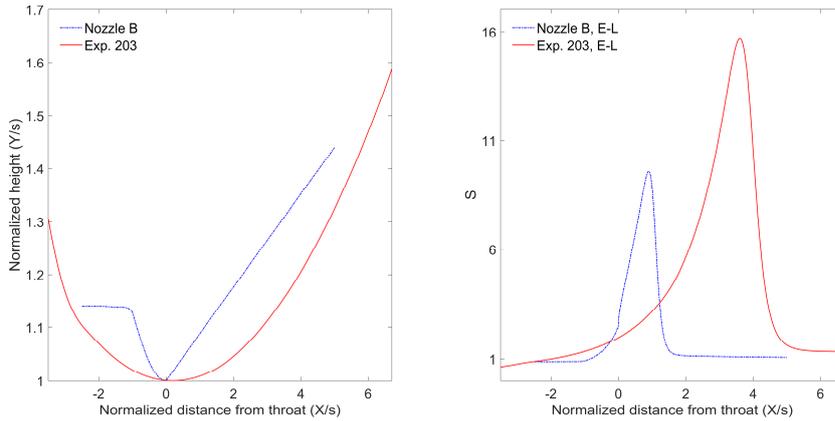


Figure 6.1: Comparisons of nozzle geometries normalised with respect to the throat height (left) and supersaturations (right), throat heights are 0.1 m and 0.01 m for Nozzle B and the Moses and Stein nozzle, respectively.

The convexity conditions $d_{22} \geq 0$ and $d_{23} \geq 0$ for Nozzle B (left) and Exp. 203 (right) are checked in Figure 6.2. In both nozzles, the convexity of the moment space is violated in the nucleation fronts; note the missing parts of d_{22} and d_{23} curves where the nucleation process starts. The explanation for the loss of convexity is that in the vicinity of the nucleation front, the underlying NDFs have not had enough time yet to develop by droplet growth. Moreover, the nucleation of droplets of a critical size results in delta-like NDFs in the cells with monodispersed droplets corresponding to the local critical radius. Applying a high-order advection scheme leads to subtracting (or mixing) these delta functions from different cells and consequently leads to a size distribution with negative values for radii around the critical size of the subtracted NDF.

The comparisons of distributions of pressure and mean droplet radii (r_{20} and r_{32}) are shown in Figures 6.3 and 6.4, respectively. Despite the loss of convexity for the E-E result applying the third-order MUSCL, these figures show no clear difference between the results, which can be attributed to the nonrealisability problem.

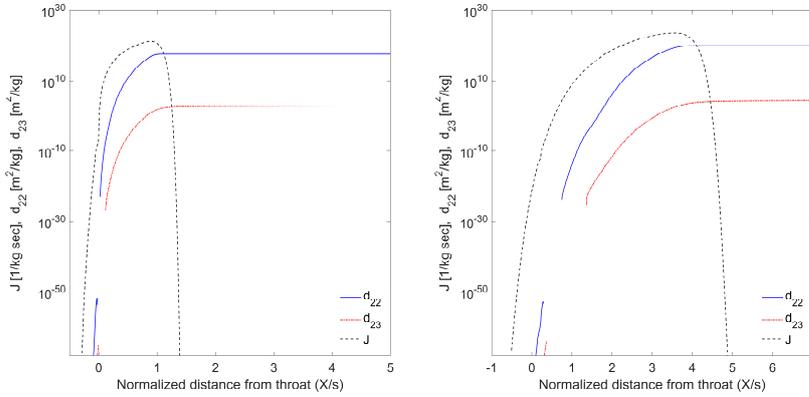


Figure 6.2: Nucleation rates and checks of the convexity condition for the CMOM with the third-order schemes in Nozzle B (left) and Exp. 203 (right).

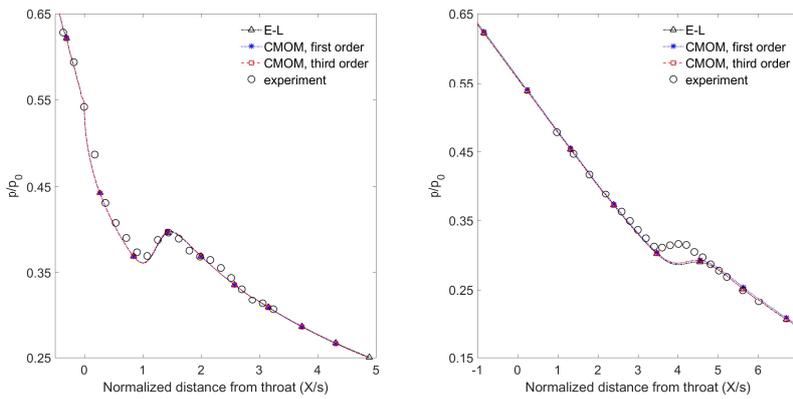


Figure 6.3: Comparisons of pressure distributions for Nozzle B (left) and Exp. 203 (right).

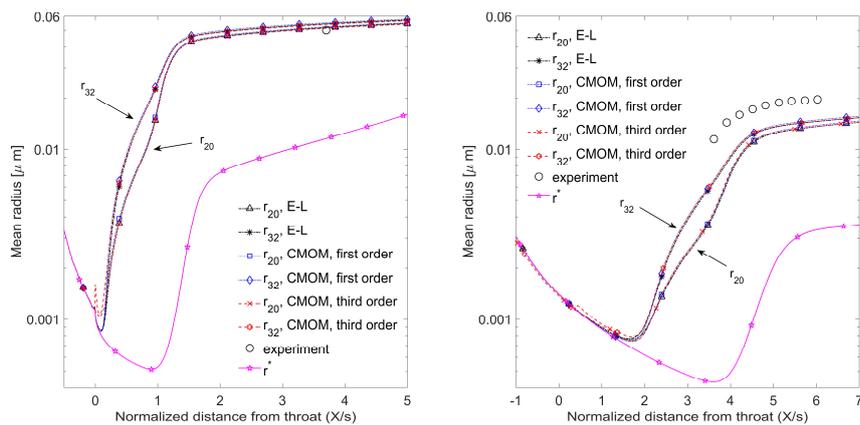


Figure 6.4: Comparisons of mean radii for Nozzle B (left) and Exp. 203 (right).

6.2 Subcritical condensation with two nucleation processes

For typical steady shock-free expansions, such as nozzle experiments by Moore et al. (1973) and the nozzle of Moses and Stein (1978), the moment gradients are generated only due to a single nucleation process. In these cases, droplet size distributions are generally very narrow and even a monodispersed representation of droplets suffices to deliver reasonably accurate predictions. However, condensation in wet-steam turbines consists of a sequence of several nucleation events. Thus, the inaccuracy in the prediction of the size of droplets in each nucleation processes can accumulate and distort the overall results.

To evaluate the possible effects of the nonrealisability problem for a more complex nucleation process, the current test case considers condensation with a primary and also a secondary nucleation event. As depicted in Figure 6.5, the considered domain, namely the double nozzle, consists of two nozzles linked by a constant-area duct. The inlet conditions are the same as those of Nozzle B. The overall hypothetical expansion rates in the nucleation zones of the first and second nozzles are about 600 sec^{-1} and 2000 sec^{-1} , respectively. The supersaturation distribution in Figure 6.5 shows that condensation begins with the primary nucleation occurring in the first nozzle converging part and continues in the duct where the release of latent heat in the absence of expansion considerably reduces the supersaturation. However, the insufficient interfacial surface area and high expansion rate of the second nozzle allows supersaturation to re-rise and triggers the secondary nucleation process. In return, the secondary nucleation sufficiently increases the interfacial surface area to quench itself.

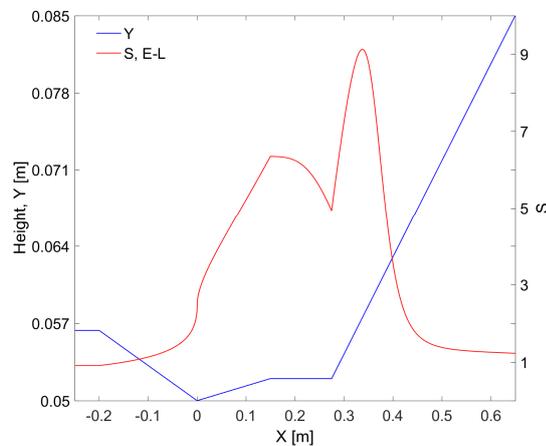


Figure 6.5: Geometry and supersaturation distribution for the double nozzle.

As with Nozzle B and Exp. 203, Figure 6.6 shows that also for the double nozzle, convexity is lost near the first nucleation front. In addition, as demonstrated in Figure 6.7, all distributions of mean radii and pressure are nearly identical irrespective of the method of the order of advection schemes. By the same token, the normalised moments are also well within the range especially those obtained using third-order MUSCL. As shown in Figure 6.8, the similarity of moments are reflected also in comparison to the standard deviation σ and skewness γ , computed as

$$\sigma = \left(\frac{\mu_2}{\mu_0} - \left(\frac{\mu_1}{\mu_0} \right)^2 \right)^{1/2} \tag{6.1}$$

$$\gamma = \frac{\frac{\mu_3}{\mu_0} - 3 \frac{\mu_1}{\mu_0} \sigma^2 - \left(\frac{\mu_1}{\mu_0} \right)^3}{\sigma^3} \tag{6.2}$$

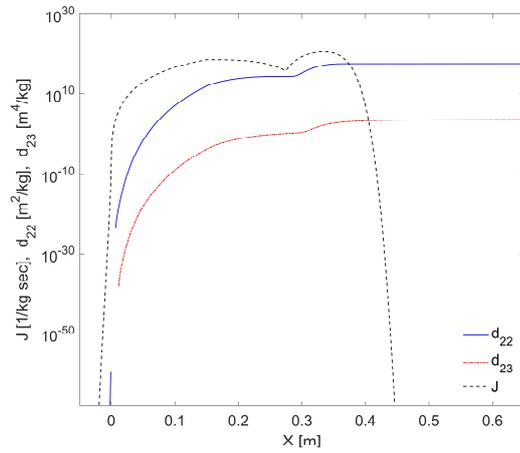


Figure 6.6: Nucleation rate and check of convexity condition for the CMOM with the third-order schemes in the double nozzle.

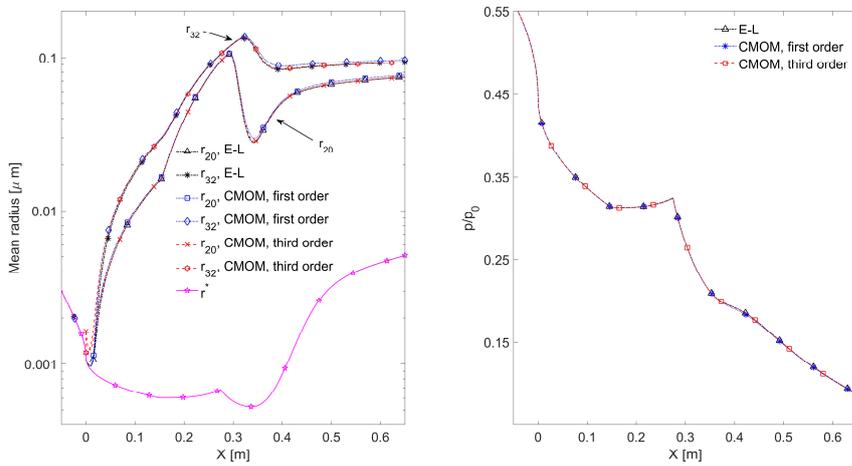


Figure 6.7: Comparisons of mean radii (left) and pressure distributions (right) for the double nozzle.

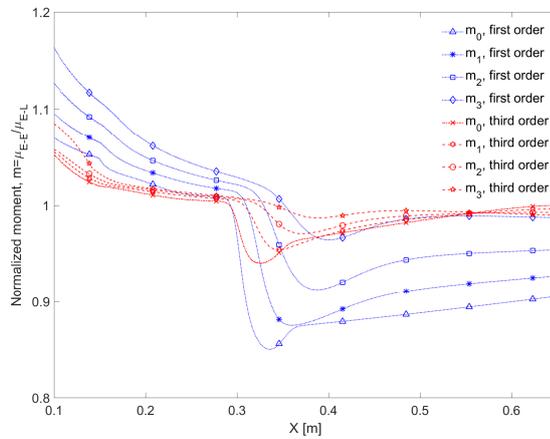


Figure 6.8: Relative moments, with respect to those obtained by the E-L method, for the double nozzle.

6.3 Unsteady supercritical condensation

This case concerns an oscillatory condensation mode interacting with an embedded aerodynamic shock in Nozzle B. To reach this flow mode, the inlet stagnation pressure is kept the same as for Nozzle B, i.e. 0.25 bar. However, the superheating degree at the inlet is decreased to 2.4 K. The aim is to see how the strong temporal and spatial gradients of moments in this case can affect the moment corruption. The periodic behaviour of pressure, in the form of the sum of the absolute pressure change between time steps in the entire domain, is demonstrated in Figure 6.9.

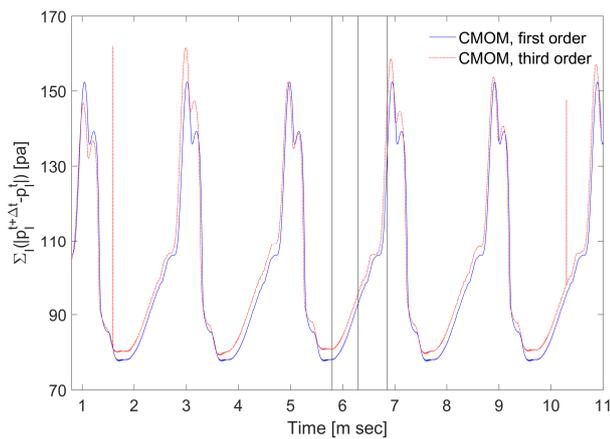


Figure 6.9: Periodic behaviour of pressure induced by supercritical condensation. For “CMOM, third order” only the moment-transport equations are solved using the third-order MUSCL, the vertical lines mark the times shown in Figures 6.10 and 6.11.

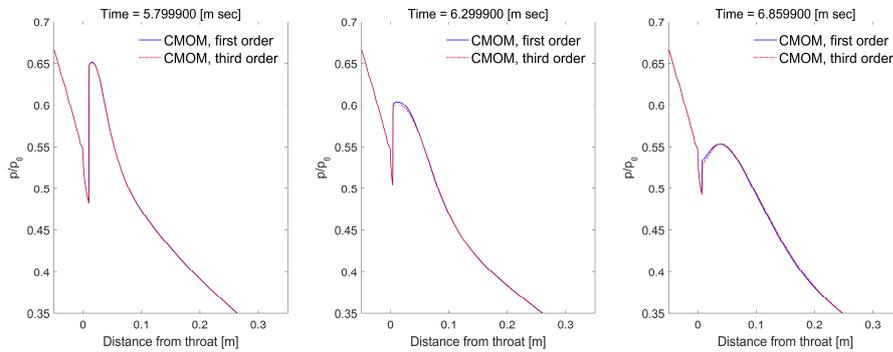


Figure 6.10: Comparison of pressure in different times for the flow with supercritical condensation. For “CMOM, third order” only the moment-transport equations are solved using the third-order MUSCL.

For this case to focus only on the effects of applying the high-order advection scheme to the moment-transport equations, the third-order MUSCL is only used for the moment advectons. That is to say all calculations were performed by solving the Euler equations using the first-order accuracy in space, while for the results denoted by ‘CMOM, third order’, the moment-transport equations are discretised applying the third-order MUSCL. The distributions of pressure and mean radii at three time steps are compared in Figures 6.10 and 6.11 showing no clear disparity, which can be attributed to nonrealisability.

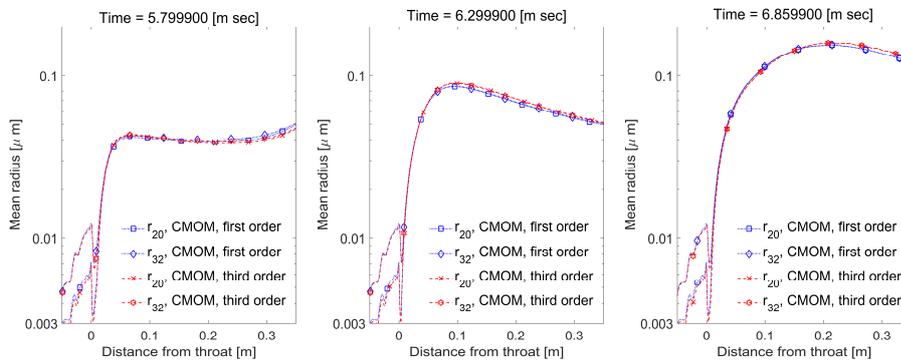


Figure 6.11: Comparison of mean droplet radii in different times for the flow with supercritical condensation. For “CMOM, third order”, only the moment-transport equations are solved using the third-order MUSCL.

Contrary to all previous cases, Figure 6.12 shows that the loss of convexity is not confined to the vicinity of the nucleation front. Nevertheless, the non-convex or nonrealisable regions are generated downstream of the aerodynamic shock where moments have significant values. The effects of nonrealisability are clearly visible in comparison to the standard deviation and skewness, as shown in Figures 6.13 and 6.14, respectively. Using the third-order MUSCL has led to nonrealisable sets in many cells for which no NDF can be sought. Furthermore, due to severe distortions of moment space, even in the cells with realisable moment sets, the standard deviation and skewness, as the typical measures of a distributions, possess unreasonable values.

However, in general, as the size distribution is very narrow, nonrealisability does not affect the overall predictions for pressure and mean droplet size.

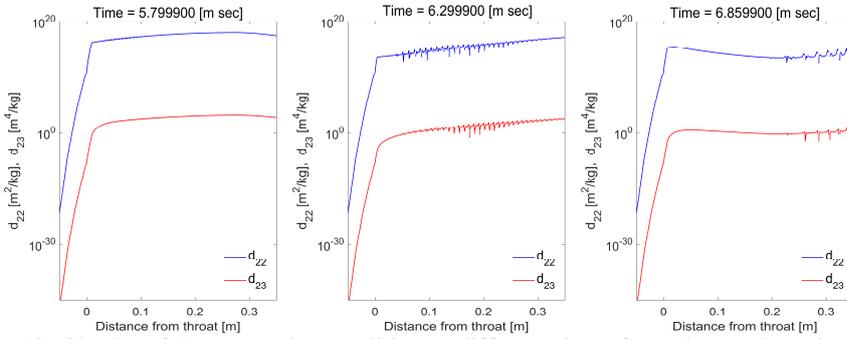


Figure 6.12: Checks of the convexity condition at different times from the results using the third-order schemes for the flow with supercritical condensation. Only the moment-transport equations are solved using the third-order MUSCL.

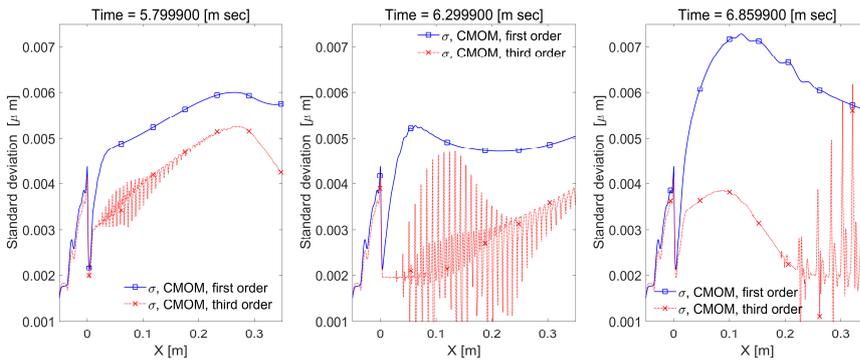


Figure 6.13: Comparison of standard deviation at different times for the flow with supercritical condensation; the curves of CMOM with the third-order schemes only show the values in cells with realisable moment sets. For “CMOM, third order” only the moment-transport equations are solved using the third-order MUSCL.

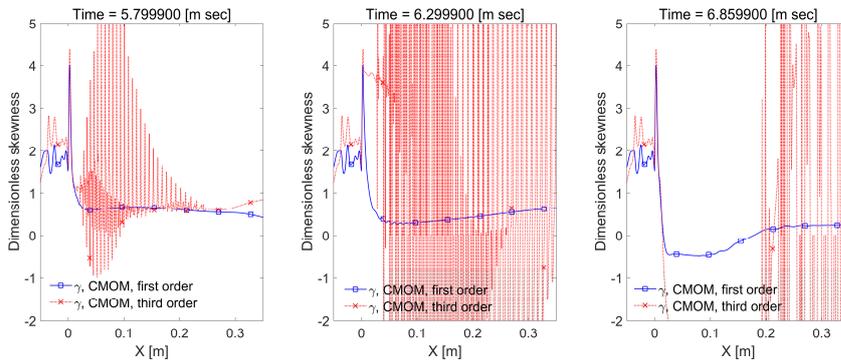


Figure 6.14: Comparison of skewness at different times for the flow with supercritical condensation; the curves of CMOM with the third-order schemes only show the values in cells with realisable moment sets. For “CMOM, third order” only the moment-transport equations are solved using the third-order MUSCL.

7 Conclusions and recommendations

This chapter briefly present the conclusions of Publications I, II, III and IV, which correspond to chapters 2, 4, 5 and 6, respectively.

7.1 Origin of droplet size underprediction in modelling of low pressure nucleating flows of steam

From the standpoint of modelling LP wet-steam flows, the excessive dependence of CNT on supersaturation was reappraised. It was demonstrated that this excessive dependence on supersaturation becomes more severe in the temperature range of interest in LP steam turbines. The complex mechanism of nucleation-growth is explained to decouple the inadequacies of CNT and the droplet growth equation from one another. In general, the main findings of Publication I are:

- The physical connection between the incorrect supersaturation dependence of CNT and mean droplet size underprediction in modelling LP nucleating flows of steam was described.
- Applying a semi-empirical nucleation model, it was shown that decreasing the dependence of CNT on supersaturation can improve the mean droplet size prediction without violating the agreement with the measured pressure.
- It is demonstrated that reducing and rectifying the dependence of the nucleation rate on supersaturation can lead to increased nucleation rates in comparatively low supersaturations, quench the nucleation process quicker, decrease the droplet number density, and thus, provide a better prediction for the mean droplet size.

7.2 Comparison of moment-based methods for representing droplet size distributions in supersonic nucleating flows of steam

Two LP supersonic nozzle experiments were chosen for comparing the CMOM, QMOM, Mono and E-L model. Considering the simple flow behaviour in these test cases, it is argued that the pressure and mean droplet size the predictions by the Mono are considerably different compared to the other models. In contrast, the three polydisperse models predict similar patterns for the pressure and mean diameter distributions. However, it was shown that the predictions of the moments and estimation of size distribution by the QMOM are much closer to those by the E-L particularly in the nucleation zone.

Moreover, it was observed that Gyarmathy's droplet growth equation and its revised version by Young are almost independent of the droplet size in the post-nucleation region of nozzles where supersaturation is marginal. Therefore, the QMOM reduces to the MOM where supersaturation is not significant and nucleation is quenched. For the same reason, in the first test case in which nucleation is limited to a small section of the nozzle and the post-nucleation droplet growth extends over a much larger section, the MOM and QMOM provide very similar

predictions for the underlying size distributions. In contrast, in the second case in which nucleation is more pronounced and covers a large part of the domain, the MOM and QMOM predict quite different size distributions even in the post-nucleation region. Consequently, in multistage steam turbines in which there is a sequence of several nucleation processes, predictions by the MOM can be far from certain especially because the MOM is not capable, in contrast to the QMOM, of taking account of polydispersity in modelling the droplet growth.

7.3 Nonrealisability problem with quadrature method of moments in wet-steam flows and solution techniques

It was shown that QMOM is burdened by the nonrealisability problem when it is together with high-order spatial and temporal schemes. Two types of solutions to this problem with the QMOM were examined and compared, namely realisable high-order advection schemes and moment correction methods. It was shown that the moment corrections either cannot detect and correct the nonrealisable moment sets or distort the proportionality of the corrected moment sets to the original ones. In contrast, a realisable high-order advection scheme can reliably preserve the moment space and avoid the nonrealisability problem.

7.4 Nonrealisability problem with conventional method of moments in wet-steam flows

The effect of the nonrealisability problem on the CMOM was examined. It was shown that although the CMOM is not interrupted by moment corruption, nonrealisable moment sets can still be generated by using a high-order advection scheme. Three types of test cases were used to see whether the CMOM results differ when moments become nonrealisable. The first type pertained to the subcritical condensation in supersonic nozzles. The second type considered condensation consisting of a primary and secondary nucleation process in a so-called 'double nozzle'. Finally, the third case concerned unsteady supercritical condensation with an embedded aerodynamic shock.

The two first cases showed no detectable differences in results, which can be related to moment corruption. This is chiefly due to the fact that the regions with nonrealisable moment sets were limited to a small region near the nucleation fronts where moments possess extremely low values. On the other hand, for the third case the moment corruption occurred far downstream of the nozzle throat where the moments had high values. As the moment sets were distorted quite significantly, the standard deviation and skewness also took unreasonable values in the majority of the domain. Nevertheless, because the droplet size distributions for this case were narrow, no considerable effects could be observed on the pressure and mean droplet sizes which can be associated with the nonrealisability problem.

It should be noted that although the studied test cases were selected considering the practical conditions in steam turbines, they were not able to mimic all of the complicated flow features of unsteady flows in multistage full-scale turbines. Thus, knowing that the theories of nucleation and droplet growth are subject to severe uncertainties, it is suggested the CMOM should be applied together with realisable advection schemes to avoid additional uncertainties over the modelling results.

References

- Bakhtar, F., Henson, R. & Mashmouhy, H., 2006. On the performance of a cascade of turbine rotor tip section blading in wet steam. Part 5: theoretical treatment. *Proceedings of the Institution of Mechanical Engineers, Part C: Journal of Mechanical Engineering Science*, 220(4), pp. 457-472.
- Bakhtar, F. & Piran, M., 1979. Thermodynamic properties of supercooled steam. *International Journal of Heat and Fluid Flow*, 1(2), pp. 53-62.
- Bakhtar, F., Young, J. B., White, A. & Simpson, D. A., 2005. Classical nucleation theory and its application to condensing steam flow calculations. *J. Mechanical Engineering Science*, 219(12), pp. 1315-1333.
- Bauman, K., 1921. Some recent developments in large steam turbine practice. *J. Inst. Elec. Engrs*, Volume 59, p. 565.
- Becker, R. & Döring, W., 1935. Kinetische behandlung der keimbildung in übersättigten dämpfen. *Annalen der Physik*, 416(8), pp. 719-752.
- Brus, D., Zdimal, V. & Smolik, J., 2008. Homogeneous nucleation rate measurements in supersaturated water vapor. *J. Chem. Phys.*, Volume 174501, p. 129.
- Brus, D., Zdimal, V. & Uchtmann, H., 2009. Homogeneous nucleation rate measurements in supersaturated water vapor II. *J. Chem. Phys.*, Volume 131, p. 074507.
- Chandler, K., White, A. J. & Young, J. B., 2014. Non-equilibrium wet-steam calculations of unsteady low-pressure turbine flows. *Proceedings of the Institution of Mechanical Engineers, Part A: Journal of Power and Energy*, Volume 228, pp. 143-152.
- Chen, B., Siepmann, J. I., Oh, K. J. & Klein, M. L., 2001. Aggregation-volume-bias Monte Carlo simulations of vapor-liquid nucleation barriers for Lennard-Jonesium. *J. Chem. Phys.*, Volume 115, pp. 10903-10913.
- Courtney, W. G., 1961. Remarks on homogeneous nucleation. *J. Chemical Physics*, 35(6), pp. 2249-2250.
- Desjardins, O., Fox, R. O. & Villedieu, P., 2008. A quadrature-based moment method for dilute fluid-particle flows. *Journal of Computational Physics*, 227(4), pp. 2514-2539.
- Dillmann, A. & Meier, G., 1991. A refined droplet approach to the problem of homogeneous nucleation from the vapor phase. *J. Chem. Phys.*, Volume 94, pp. 3872-3884.
- Dykas, S. & Wróblewski, W., 2011. Single-and two-fluid models for steam condensing flow modeling. *International Journal of Multiphase Flow*, 37(9), pp. 1245-1253.

- Dykas, S. & Wróblewski, W., 2012. Numerical modelling of steam condensing flow in low and high-pressure nozzles. *International Journal of Heat and Mass Transfer*, Volume 55, pp. 6191-6199.
- Fakhari, K., 2006. Development of a two-phase Eulerian/Lagrangian algorithm for condensing steam flows. *44th AIAA Aerospace Science Meeting*, Volume 10, pp. 7156-7167.
- Farkas, L., 1927. Keimbildungsgeschwindigkeit in übersättigten Dämpfen. *Z. phys. Chem*, Volume 125, pp. 236-242.
- Feller, W., 1971. *An introduction to probability theory and its applications. Vol. II*. New York: John Wiley & Sons.
- Frenkel, J., 1955. *Kinetic theory of liquids*. New York: Dover.
- Fuks, N. A. & Sutugin, A. G., 1970. *Highly dispersed aerosols*. s.l.:Ann Arbor Science Publishers, Ann Arbor, MI.
- Fuller, G. M., Mathews, G. J. & Alcock, C. R., 1988. Quark-hadron phase transition in the early Universe: Isothermal baryon-number fluctuations and primordial nucleosynthesis. *Physical Review D*, 37(6), p. 1380.
- Gail, H. P. & Sedlmayr, E., 1988. Dust formation in stellar winds. IV-Heteromolecular carbon grain formation and growth. *Astronomy & Astrophysics*, Volume 206, pp. 153-168.
- Gerber, A. G., 2002. Two-phase Eulerian/Lagrangian model for nucleating steam flow. *Journal of Fluids Engineering*, 124(2), pp. 465-475.
- Gerber, A. G., 2008. Inhomogeneous multifluid model for prediction of nonequilibrium phase transition and droplet dynamics. *Journal of Fluids Engineering*, 130(3), p. 031402.
- Gerber, A. G. & Kermani, M. J., 2004. A pressure based Eulerian–Eulerian multi-phase model for non-equilibrium condensation in transonic steam flow. *International Journal of Heat and Mass Transfer*, 47(10), pp. 2217-2231.
- Gerber, A. G. & Mousavi, A., 2006. Application of quadrature method of moments to the polydispersed droplet spectrum in transonic steam flows with primary and secondary nucleation. *Applied Mathematical Modelling*, 31(8), pp. 1518-1533.
- Gerber, A. G. & Mousavi, A., 2007. Representing polydispersed droplet behavior in nucleating steam flow. *Journal of Fluids Engineering*, 129(11), pp. 1404-1414.

- Gibbs, J. W., 1878. On the equilibrium of heterogeneous substances. *American Journal of Science*, Volume 96, pp. 441-458.
- Girshick, S. L., 2014. The dependence of homogeneous nucleation rate on supersaturation. *J. Chem. Phys.*, Volume 141, p. 024307.
- Gordon, R. G., 1968. Error bounds in equilibrium statistical mechanics. *Journal of Mathematical Physics*, Volume 9, pp. 655-663.
- Gyarmathy, G., 1962. *Grundlagen einer theorie der nassdampfturbine*, Diss. Techn. Wiss. Nr. 3221, Ref.: W. Traupel, Korref.: J. Ackeret. Zürich, ETH Zürich.
- Gyarmathy, G., 1976. Condensation in flowing steam. In: M. J. Moore & C. H. Sieverding, eds. *Two-Phase Steam Flow in Turbines and Separators*. Washington: Hemisphere Publishing Corporation, pp. 127-190.
- Halama, J. & Fort, J., 2012. *Numerical simulation of two-phase flow in a low pressure steam turbine stage*. Svatka, Czech Republic, Engineering Mechanics .
- Hall, R. M. & Kramer, S. A., 1979. *A review of at rest droplet growth equations for condensing nitrogen in transonic cryogenic wind tunnels.*, Hampton, Virginia: NationalAeronautics and Space Administration.
- Hansen, K., 2014. Comment on "The dependence of homogeneous nucleation rate on supersaturation" [J. Chem. Phys. 141, 024307 (2014)]. *J. Chem. Phys.*, Volume 141, p. 157101.
- Helmholtz, R. V., 1886. Untersuchungen über Dämpfe und Nebel, besonders über solche von Lösungen. *Annalen der Physik*, 263(4), pp. 508-543.
- Hill, P. G., 1966. Condensation of water vapour during supersonic expansion in nozzles. *J. Fluid Mech*, 25(3), pp. 593-620.
- Hill, P. G., Miyagawa, K. & Denton, J. D., 2000. Fast and accurate inclusion of steam properties in two-and three-dimensional steam turbine flow calculations. *Proceedings of the Institution of Mechanical Engineers, Part C: Journal of Mechanical Engineer Science*, 214(7), pp. 903-919.
- Holten, V., Labetski, D. G. & Van Dongen, M. E. H., 2005. Homogeneous nucleation of water between 200 and 240 K: New wave tube data and estimation of the Tolman length. *J. Chem. Phys.*, Volume 123, p. 104505.
- Hulburt, H. M. & Katz, S., 1964. Some problems in particle technology: A statistical mechanical formulation. *Chemical Engineering Science*, 19(8), pp. 555-574.

- IAPWS, 2007. *Release on the IAPWS Industrial Formulation 1997 for the Thermodynamic*, s.l.: s.n.
- Kah, D., Laurent, F., Massot, M. & Jay, S., 2012. A high order moment method simulating evaporation and advection of a polydisperse liquid spray. *Journal of Computational Physics*, 231(2), pp. 394-422.
- Kantrowitz, A., 1951. Nucleation in very rapid vapor expansions. *J. Chemical Physics*, 19(9), p. 1097.
- Kashchiev, D., 1982. On the relation between nucleation work, nucleus size, and nucleation rate. *J. Chem. Phys.*, Volume 76, pp. 5098-5102.
- Keenan, J. H., Keyes, F. G., Hill, P. G. & Moore, J. G., 1978. *Steam Tables: Thermodynamics Properties of Water Including Vapor, Liquid and Solid Phases*. New York: John Wiley & Sons.
- Kermani, M. J. & Gerber, A. G., 2003. A general formula for the evaluation of thermodynamic and aerodynamic losses in nucleating steam flow. *International Journal of Heat and Mass Transfer*, 46(17), pp. 3265-3278.
- Kim, Y. J. et al., 2004. Isothermal nucleation rates in supersonic nozzles and the properties of small water clusters. *The Journal of Physical Chemistry A*, Volume 108, pp. 4365-4377.
- Kirillov, I. I. & Yablonik, R. M., 1968. *Fundamentals of the theory of turbines operating on wet steam*. Leningrad, Russia: Mashinostroyeniye.
- Koren, B., 1993. A robust upwind discretization method for advection, diffusion and source terms. *Notes on Numerical Fluid Mechanics*, Volume 45, pp. 117-138.
- Kulmala, M. et al., 2013. Direct observations of atmospheric aerosol nucleation. *Science*, 339(6122), pp. 943-946.
- Laaksonen, A. & Oxtoby, D. W., 1995. Gas-liquid nucleation of nonideal binary mixtures. I. A density functional study. *The Journal of chemical physics*, 102(14), pp. 5803-5810.
- Laaksonen, A., Talanquer, V. & Oxtoby, D. W., 1995. Nucleation: Measurements, theory, and atmospheric applications. *Annu. Rev. Phys. Chem.*, Volume 46, pp. 489-524.
- Li, H. et al., 2006. Modeling the large-scale structures of astrophysical jets in the magnetically dominated limit. *The Astrophysical Journal*, pp. 92-100.
- Liou, M. S. & Steffen, C. J., 1993. A new flux splitting scheme. *Journal of Computational Physics*, 107(1), pp. 23-39.

- Lothe, J. & Pound, G. M., 1962. Reconsiderations of nucleation theory. *J. Chem. Phys.*, Volume 36, pp. 2080-2085.
- Luijten, C. C. M., Bosschaart, K. J. & Van Dongen, M. E. H., 1997. High pressure nucleation in water/nitrogen systems. *J. Chem. Phys.*, Volume 106, pp. 8116-8123.
- Manka, A. A. et al., 2010. Homogeneous water nucleation in a laminar flow diffusion chamber. *J. Chem. Phys.*, Volume 132, p. 244505.
- Marchisio, D. L. & Fox, R. O., 2013. *Computational models for polydisperse particulate and multiphase systems*. New York: Cambridge University Press.
- Marchisio, D. L. et al., 2003. Quadrature method of moments for population-balance equations. *AIChE Journal*, 49(5), pp. 1266-1276.
- Mason, B. J., 1960. Nucleation of water aerosols. Discussions of the Faraday Society. *Discussions of the Faraday Society*, Volume 30, pp. 20-38.
- Mccallum, M. & Hunt, R., 1999. The flow of wet steam in a one-dimensional nozzle.. *International journal for numerical methods in engineering*, 44(12), pp. 1807-1821.
- McGraw, R., 1997. Description of aerosol dynamics by the quadrature method of moments. *Aerosol Science and Technology*, 27(2), pp. 255-265.
- McGraw, R., 2006. <https://www.bnl.gov/envsci/>. [Online] Available at: http://www.ecd.bnl.gov/pubs/momentcorrection_mcgraw2006.pdf [Accessed 23 11 2015].
- Mikheev, V. B. et al., 2002. Laboratory measurement of water nucleation using a laminar flow tube reactor. *J. Chem. Phys.*, Volume 116, pp. 10772-10786.
- Miller, R. C., Anderson, R. J., Kassner Jr, J. L. & Hagen, D. E., 1983. Homogeneous nucleation rate measurements for water over a wide range of temperature and nucleation rate. *The Journal of Chemical Physics*, Volume 78, pp. 3204-3211.
- Moore, M. J. & Sculpher, P., 1969. Conditions producing concentrated erosion in large steam turbines. *Proceedings of the Institution of Mechanical Engineers*, 184(7), pp. 45-56.
- Moore, M. J., Walters, P. T., Crane, R. I. & Davidson, B. J., 1973. *Predicting the fog-drop size in wet-steam turbines*. Warwick, s.n.
- Moses, C. A. & Stein, G. D., 1978. On the growth of steam droplets formed in a Laval nozzle using both static pressure and light scattering measurements. *Journal of Fluids Engineering*, Volume 100, pp. 311-322.

- Mullick, K. et al., 2015. Isothermal nucleation rates of n-propanol, n-butanol, and n-pentanol in supersonic nozzles: critical cluster sizes and the role of coagulation. *J. Phys. Chem. B*, Volume 119, pp. 9009-9019.
- Oxtoby, D. W., 1992. Homogeneous nucleation: Theory and experiment. *Journal of Physics: Condensed Matter*, Volume 7627, p. 4.
- Pathak, H., Mullick, K., Tanimura, S. & Wyslouzil, B. E., 2013. Nonisothermal droplet growth in the free molecular regime. *Aerosol Science and Technology*, Volume 47, pp. 1310-1324.
- Porter, D. A., Easterling, K. E. & Sherif, M. Y., 2009. *Phase Transformations in Metals and Alloys*. Boca Raton, Florida: CRC Press.
- Press, W. H., Teukolsky, S. A., Vetterling, W. T. & Flannery, B. P., 1992. *Numerical Recipes in Fortran 77: The Art of Scientific Computing*. 2nd ed. Cambridge: Cambridge University Press.
- Randolph, A. D. & Larson, M. A., 1988. *Theory of Particulate Processes: Analysis and Techniques of Continuous Crystallization*. San Diego, California: Academic Press Inc.
- Reiss, H., Kegel, W. K. & Katz, J. L., 1997. Resolution of the problems of replacement free energy, $1/S$, and internal consistency in nucleation theory by consideration of the length scale for mixing entropy. *Phys. Rev. Lett.*, Volume 78, p. 4506.
- Roe, P. L., 1986. Characteristic-based schemes for the Euler equations. *Annual Review of Fluid Mechanics*, 18(1), pp. 337-365.
- Schmelzer, J. W. P., Boltachev, G. S. & Baidakov, V. G., 2006. Classical and generalized Gibbs' approaches and the work of critical cluster formation in nucleation theory. *J. Chem. Phys.*, Volume 124, p. 194503.
- Schnerr, G. H., Adam, S., Lanzenberger, K. & Schulz, R., 1995. Multiphase flows: Condensation and cavitation. In: *Computational Fluid Dynamics REVIEW*. Chichester, England: John Wiley & Sons, pp. 614-640.
- Shohat, J. A. & Tamarkin, J. D., 1943. *The problem of moments*. New York: American Mathematical Soc.
- Simpson, D. A. & White, A. J., 2005. Viscous and unsteady flow calculations of condensing steam in nozzles. *International journal of heat and fluid flow*, 26(1), pp. 71-79.
- Sinha, S., Wyslouzil, B. E. & Wilemski, G., 2009. Modeling of H₂O/D₂O condensation in supersonic nozzles. *Aerosol Science and Technology*, Volume 43, pp. 9-24.

- Stodola, A., 1922. *Dampf-und Gasturbinen: mit einem Anhang über die Aussichten der Wärmekraftmaschinen*. 5th ed. Berlin: Springer.
- Temelso, B., Archer, K. A. & Shields, G. C., 2011. Benchmark structures and binding energies of small water clusters with anharmonicity corrections. *The Journal of Physical Chemistry A*, 115(43), pp. 12034-12046.
- Ten Wolde, P. R., Oxtoby, D. W. & Frenkel, D., 1998. Coil-globule transition in gas-liquid nucleation of polar fluids. *Phys. Rev. Lett.*, Volume 81, p. 3695.
- Thomson, W., 1872. On the Equilibrium of Vapour at a Curved Surface of Liquid. *Proceedings of the Royal Society of Edinburgh*, Volume 7, pp. 63-68.
- Walters, P. T., 1987. Wetness and efficiency measurements in LP turbines with an optical probe as an aid to improving performance. *Journal of engineering for gas turbines and power*, 109(1), pp. 85-91.
- Walters, P. T., 1988. *Improving the accuracy of wetness measurements in generating turbines by using a new procedure for analysing optical transmission data*, London: British Nuclear Energy Society.
- Van Leer, B., 1979. Towards the Ultimate Conservative Difference Scheme V. A second Order Sequel to Godunov's method. *J. Computational Physics*, Volume 32 , pp. 101-136.
- Van Leer, B., 1997. *Flux Vector Splitting for the Euler Equations*. s.l., 8th Int. Conf. on Numerical Methods in Fluid Dynamics, Springer Verlag, pp. 80-89.
- Vekilov, P. G., 2010. Nucleation. *Crystal Growth & Design*, Volume 10, pp. 5007-5019.
- Wheeler, J. C., 1974. Modified moments and Gaussian quadratures. *Rocky Mountain Journal of Mathematics*, Volume 4, pp. 287-296.
- White, A. J., 2003. A comparison of modelling methods for polydispersed wet-steam flow. *International Journal for Numerical Methods in Engineering*, 57(6), pp. 819-834.
- White, A. J. & Hounslow, M. J., 2000. Modelling droplet size distributions in polydispersed wet-steam flows. *International Journal of Heat and Mass Transfer*, 43(11), pp. 1873-1884.
- White, A. J. & Young, J. B., 1993. Time-marching method for the prediction of two-dimensional, unsteady flows of condensing steam. *Journal of Propulsion and Power*, 9(4), pp. 579-587.

- White, A. J. & Young, J. B., 2008. *Transient calculations of nucleation and droplet growth for wet-steam expansion*. Berlin, ICPWS XV.
- White, A., Young, J. & Walters, P., 1996. Experimental validation of condensing flow theory for a stationary cascade of steam turbine blades. *Philosophical Transactions of the Royal Society of London A: Mathematical, Physical and Engineering Sciences*, 354(1704), pp. 59-88.
- Vikas, V., Wang, Z. J., Passalacqua, A. & Fox, R. O., 2011. Realizable high-order finite-volume schemes for quadrature-based moment methods. *Journal of Computational Physics*, 230(13), pp. 5328-5352.
- Volmer, M., 1939. *Kinetik der Phasenbildung*. Dresden: Steinkopff.
- Wright, D. L., 2007. Numerical advection of moments of the particle size distribution in Eulerian models. *Journal of Aerosol Science*, 38(3), pp. 352-369.
- Vukalovich, M., 1958. *Thermodynamic Properties of Water and Steam, sixth ed.*. Mashgis, Moscow: s.n.
- Wölk, J. & Strey, R., 2001. Homogeneous nucleation of H₂O and D₂O in comparison: The isotope effect. *J. Chem. Phys.*, Volume 105, pp. 11683-11701.
- Wölk, J., Strey, R. & Heath, C. H. W. B. E., 2002. Empirical function for homogeneous water nucleation rates. *J. Chem. Phys.*, Volume 117, pp. 4954-4960.
- Yan, Y. Y., Lio, H. C. & Lin, T. F., 1999. Condensation heat transfer and pressure drop of refrigerant R-134a in a plate heat exchanger. *International Journal of Heat and Mass Transfer*, 42(6), pp. 993-1006.
- Yasuoka, K. & Matsumoto, M., 1998. Molecular dynamics of homogeneous nucleation in the vapor phase. I. Lennard-Jones fluid. *The Journal of chemical physics*, 109(19), pp. 8451-8462.
- Young, J. B., 1982. Spontaneous condensation of steam in supersonic nozzles. *J. PhysicoChemical Hydrodynamics (PCH)*, Volume 3, pp. 57-82.
- Young, J. B., 1988. An equation of state for steam for turbomachinery and other flow calculations. *J. Engineering for Gas Turbines and Power*, 110(1), pp. 1-7.
- Young, J. B., 1992. Two-dimensional, nonequilibrium, wet-steam calculations for nozzles and turbine cascades. *J. Turbomachinery*, 114(3), pp. 569-579.
- Zeldovich, J., 1942. On the theory of new phase formation. *Zh Eksp Theor Fiz*, Volume 12, pp. 525-538.

- Zhang, X. & Shu, C. W., 2010. On positivity-preserving high order discontinuous Galerkin schemes for compressible Euler equations on rectangular meshes. *Journal of Computational Physics*, pp. 8918-8934.

Appendix: details of nozzle test cases

This appendix covers all the details about the geometry, inlet conditions and experimental data of the three nozzles studied in this thesis. These nozzles are Nozzles A and B of Moore et al. (1973) and the nozzle of Moses and Stein (1978). It is noted that Moses and Stein performed several experiments, employing an identical nozzle, by changing the steam conditions at the nozzle inlet. In contrast, Moore et al. (1973) used five different nozzles (named as A, B, C, D and E) in their work.

From Moses and Stein work, only the experiments denoted as Exp. 203 and Exp. 252, whose conditions are similar to LP steam turbines are considered for study. For these two experiments, experimental data on both droplet size and pressure distributions are available. The stagnation temperature, superheating degree and pressure at the inlet of Nozzles A and B, and Exp. 203 and Exp. 252 are given in Table A.1.

Table A.1: stagnation conditions at the nozzle inlet.

	Nozzle A	Nozzle B	Exp. 203	Exp. 252
Temperature, K	355.11	358.11	368.3	374.3
Superheating degree, K	17	20	21.95	25.26
Pressure, bar	0.25	0.25	0.358	0.4005

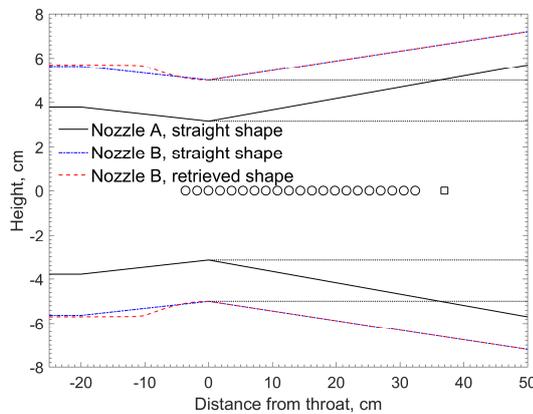


Figure A.1: geometries used for Nozzles A and B, open circles and square indicate locations of pressure and droplet size measurements, respectively.

The shapes of Nozzles A and B are depicted in Figure A.1 and the nozzle of Moses and Stein is shown in Figure A.2. It is noted that the shapes of the converging part of none of the nozzles studied by Moore et al. (1973) were given in their work. However, the shapes

of the diverging part were provided in the form of a straight line indicating that the geometry curvature was discontinuous at the throat of Nozzles A and B.

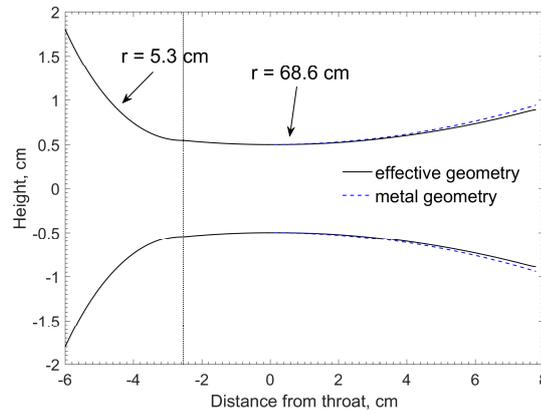


Figure A.2: geometry of Moses and Stein nozzle, the dotted line indicates the intersection of the two circular arcs.

Thus, the converging part of Nozzle B, in chapter 2 (associated with Publication I), and the converging part of Nozzle A, in chapter 4 (associated with Publication II) are approximated by the straight lines, which is indicated by “straight shape” in Figure A.1, as suggested by Kermani & Gerber (2003). To sidestep this uncertainty, in chapters 5 and 6 (associated with Publications III and IV, respectively) the geometry of Nozzle B converging part is retrieved based on the isentropic expansion of steam in this section, using the calculated distribution of pressure by Moore, et al. (1973), which is indicated by “retrieved shape” in Figure A.1.

In contrast to Nozzles A and B, Moses and Stein nozzle curvature in both transonic and supersonic sections was a continuous part of a circular arc (with the radius of 68.6 cm). This circular arc smoothly intersects with the subsonic entrance being an arc with the radius of 5.3 cm, as depicted in Figure A.2. All the nozzles in studies by Moore et al. and also Moses and Stein were built between parallel walls with constant distances of 15.2 cm and 1 cm, respectively. The large dimensions (width and height) of nozzles in the experiment by Moore et al. (1973), as stated by in their work, allows using the metal (raw) geometry in the one-dimensional numerical calculations. On the other hand, as suggested by Moses and Stein, the effective area is used in calculations of Exp. 203 and Exp. 252, owing to the considerable thickness of boundary layer compared to the nozzle height and depth. The profile of the effective area for Moses and Stein nozzle is denoted by “effective profile” in Figure A.2. The main information about the geometries of all nozzles are summarised in Table A.2.

The experimental data of pressure distribution and droplet size are obtained from the study of Young (1982), as these data were not reported in the original work by Moses and Stein. According to the Young's work, it can be deduced that pressure and droplet size measurements were performed by smoothly sliding the probes downstream of the throat from 2 to 6 cm, for pressure, and from 3.5 to 6 cm for droplet size.

Table A.2: main information about the nozzle geometries.

	Nozzle A	Nozzle B	Moses and Stein nozzle
Throat height, cm	6.3	10	1
Width, cm	15.2	15.2	1
Inclination (of the converging part) at throat, °	6.504	8.194	-
Curvature radius (in transonic and supersonic sections), cm	-	-	68.6

To display the effects of nozzles geometries on the flow behaviour, Figure A.3 and A.4 shows the normalized pressure, with respect to the inlet stagnation pressure, (left) and Mach number (right) distributions of isentropic (dry) expansions in experiments by Moore et al. and Moses and Stein, respectively.

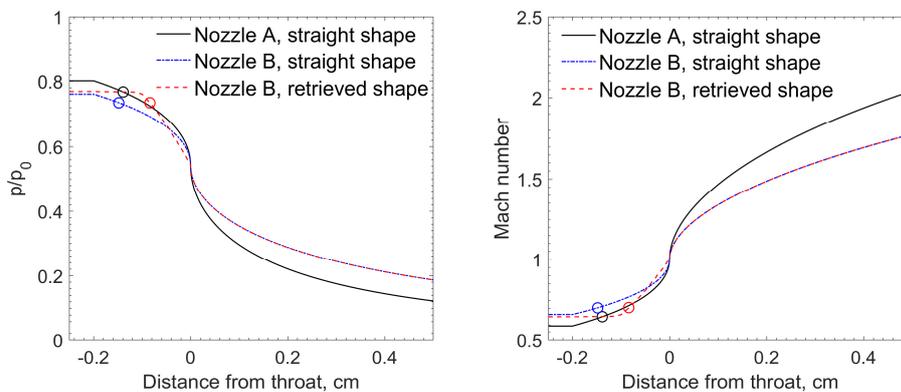


Figure A.3: normalized pressure, with respect to the inlet stagnation pressure, (left) and Mach number (right) distributions in Nozzles A and B, open circles indicate where the steam stat path crosses the saturation line.

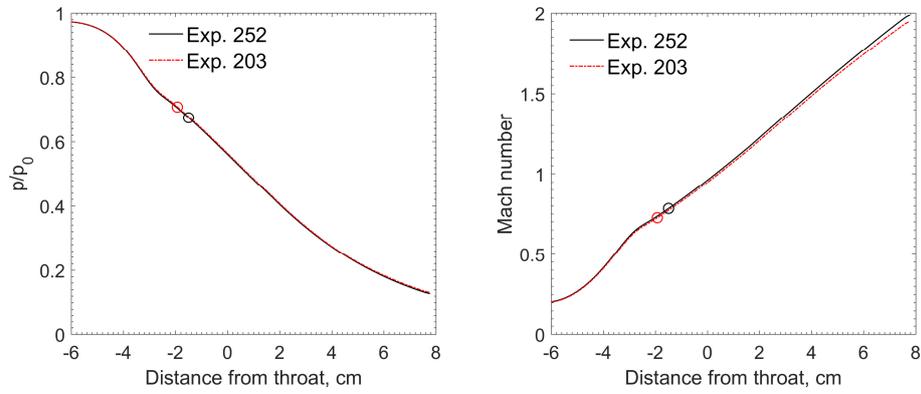


Figure A.4: normalized pressure, with respect to the inlet stagnation pressure, (left) and Mach number (right) distributions in Exp. 203 and Exp. 252, open circles indicate where the steam stat path crosses the saturation line.

Publication I

I. Afzalifar, A., Turunen-Saaresti, T., and Grönman, A.
Origin of droplet size underprediction in modeling of low pressure nucleating flows of steam

Reprinted with permission from
International Journal of Multiphase Flow
Vol. 86, pp. 86-98, 2016
© 2016, Elsevier

Publication II

II. Afzalifar, A., Turunen-Saaresti, T., and Grönman, A.

**Comparison of moment-based methods for representing droplet size distributions in
supersonic nucleating flows of steam**

*Proceedings of the 16th International Symposium on Transport Phenomena and Dynamics of
Rotating Machinery ISROMAC*

Honolulu, Hawaii, April 10-15

This Publication has been selected to be published in the special issue, entitled "Flows in
Rotating Machineries: some Recent Advances", of Journal of Fluids Engineering

Publication III

III. Afzalifar, A., Turunen-Saaresti, T., and Grönman, A.
**Nonrealizability problem with quadrature method of moments in wet-steam flows and
solution techniques**

Reprinted with permission from
Journal of Engineering for Gas Turbines and Power
Vol. 139, pp. 012602, 2017
© 2017, ASME

Publication IV

IV. Afzalifar, A., Turunen-Saaresti, T., and Grönman, A.

Nonrealisability problem with the conventional method of moments in wet-steam flows

Wet Steam Conference

Prague, September 12-14

This Publication has been selected to be published in the special issue, entitled "Wet Steam 2016", of Proceedings of the Institution of Mechanical Engineers, Part A: Journal of Power and Energy.

ACTA UNIVERSITATIS LAPPEENRANTAENSIS

724. MONTECINOS, WERNER EDUARDO JARA. Axial flux permanent magnet machines – development of optimal design strategies. 2016. Diss.
725. MULTAHARJU, SIRPA. Managing sustainability-related risks in supply chains. 2016. Diss.
726. HANNONEN, JANNE. Application of an embedded control system for aging detection of power converter components. 2016. Diss.
727. PARKKILA, JANNE. Connecting video games as a solution for the growing video game markets. 2016. Diss.
728. RINKINEN, SATU. Clusters, innovation systems and ecosystems: Studies on innovation policy's concept evolution and approaches for regional renewal. 2016. Diss.
729. VANADZINA, EVGENIA. Capacity market in Russia: addressing the energy trilemma. 2016. Diss.
730. KUOKKANEN, ANNA. Understanding complex system change for a sustainable food system. 2016. Diss.
731. SAVOLAINEN, JYRKI. Analyzing the profitability of metal mining investments with system dynamic modeling and real option analysis. 2016. Diss.
732. LAMPINEN, MATTI. Development of hydrometallurgical reactor leaching for recovery of zinc and gold. 2016. Diss.
733. SUHOLA, TIMO. Asiakaslähtöisyys ja monialainen yhteistyö oppilashuollossa: oppilashuolto prosessi systeemisenä palvelukokonaisuutena. 2017. Diss.
734. SPODNIAK, PETR. Long-term transmission rights in the Nordic electricity markets: An empirical appraisal of transmission risk management and hedging. 2017. Diss.
735. MONTONEN, JUHO. Integrated hub gear motor for heavy-duty off-road working machines – Interdisciplinary design. 2017. Diss.
736. ALMANASRAH, MOHAMMAD. Hot water extraction and membrane filtration processes in fractionation and recovery of value-added compounds from wood and plant residues. 2017. Diss.
737. TOIVANEN, JENNI. Systematic complaint data analysis in a supply chain network context to recognise the quality targets of welding production. 2017. Diss.
738. PATEL, GITESHKUMAR. Computational fluid dynamics analysis of steam condensation in nuclear power plant applications. 2017. Diss.
739. MATTHEWS, SAMI. Novel process development in post-forming of an extruded wood plastic composite sheet. 2017. Diss.
740. KÄHKÖNEN, TOMMI. Understanding and managing enterprise systems integration. 2017. Diss.
741. YLI-HUUMO, JESSE. The role of technical dept in software development. 2017. Diss.
742. LAYUS, PAVEL. Usability of the submerged arc welding (SAW) process for thick high strength steel plates for Arctic shipbuilding applications. 2017. Diss.

743. KHAN, RAKHSHANDA. The contribution of socially driven businesses and innovations to social sustainability. 2017. Diss.
744. BIBOV, ALEKSANDER. Low-memory filtering for large-scale data assimilation. 2017. Diss.
745. ROTICH, NICOLUS KIBET. Development and application of coupled discrete and continuum models in solid particles classification. 2017. Diss.
746. GAST, JOHANNA. The cooperation-innovation nexus: Investigating the role of cooperation for innovation in SMEs. 2017. Diss.
747. KAPOOR, RAHUL. Competition and disputes in the patent life cycle. 2017. Diss.
748. ALI-MARTTILA, MAAREN. Towards successful maintenance service networks – capturing different value creation strategies. 2017. Diss.
749. KASHANI, HAMED TASALLOTI. On dissimilar welding: a new approach for enhanced decision-making. 2017. Diss.
750. MVOLA BELINGA, ERIC MARTIAL. Effects of adaptive GMAW processes: performance and dissimilar weld quality. 2017. Diss.
751. KARTTUNEN, JUSSI. Current harmonic compensation in dual three-phase permanent magnet synchronous machines. 2017. Diss.
752. SHI, SHANSHUANG. Development of the EAST articulated maintenance arm and an algorithm study of deflection prediction and error compensation. 2017. Diss.
753. CHEN, JIE. Institutions, social entrepreneurship, and internationalization. 2017. Diss.
754. HUOTARI, PONTUS. Strategic interaction in platform-based markets: An agent-based simulation approach. 2017. Diss.
755. QU, BIN. Water chemistry and greenhouse gases emissions in the rivers of the "Third Pole" / Water Tower of Asia". 2017. Diss.
756. KARHU, PÄIVI. Cognitive ambidexterity: Examination of the cognitive dimension in decision-making dualities. 2017. Diss.
757. AGAFONOVA, OXANA. A numerical study of forest influences on the atmospheric boundary layer and wind turbines. 2017. Diss.
758. AZAM, RAHAMATHUNNISA MUHAMMAD. The study of chromium nitride coating by asymmetric bipolar pulsed DC reactive magnetron sputtering. 2017. Diss.
759. AHI, MOHAMADALI. Foreign market entry mode decision-making: Insights from real options reasoning. 2017. Diss.
760. AL HAMDY, ABDULLAH. Synthesis and comparison of the photocatalytic activities of antimony, iodide and rare earth metals on SnO₂ for the photodegradation of phenol and its intermediates under UV, solar and visible light irradiations. 2017. Diss.
761. KAUTTO, JESSE. Evaluation of two pulping-based biorefinery concepts. 2017. Diss.

